HEAT EXCHANGE IN TENSILE FRACTURES –

AN EXPERIMENTAL AND NUMERICAL APPROACH

Marco Balmer

MSc Thesis
Applied Earth Sciences

TUDelft

HEAT EXCHANGE IN TENSILE FRACTURES –
AN EXPERIMENTAL AND NUMERICAL APPROACH

By

Marco Balmer

To obtain the degree of Master of Science at the Delft University of Technology

To be defended publicly on Friday September 28, 2018 at 02:00 PM.

Thesis Committee:

Prof. Dr. D.F. Bruhn	TU Delft – Department of Geoscience and Engineering
Dr. A. Barnhoorn	TU Delft – Department of Geoscience and Engineering
Dr. Ir. F.C. Vossepoel	TU Delft – Department of Geoscience and Engineering
Dr. R.R. Bakker	TU Delft – Department of Geoscience and Engineering

TUDelft

Delft
University of
Technology

Contents

Abstract

Geothermal energy is a relatively sustainable energy source of which the essence is to extract heat from hot subsurface rocks. Circulating fluids serve as the transport agent of heat. The contact area between the fluids and the rocks is where the relevant heat transfer occurs, i.e., where the water is heated up. In some geothermal reservoirs, this circulation occurs naturally through porous matrix (mainly sediments) or through heavily fractured formations. Enhanced geothermal systems (EGS) are potentially favorable reservoirs where subsurface permeability is increased by means of artificial stimulation techniques. These stimulation techniques often involve hydraulic fracturing where a limited existing fracture network is expanded or "enhanced" by injecting fluids under high pressure conditions. While the geometry of the generated fractures influences permeability, the effect on heat exchange has received less attention. This thesis discusses the effects of fracture geometry on the heat transfer between solid and fluid. Along with laboratory experiments, numerical simulations were conducted. All investigations were performed on igneous granite rocks. Tensile fractures were generated to allow a fluid flow along the otherwise impermeable rock samples. Several parameters were varied throughout the experiments and simulations including volumetric flow rate, fracture aperture, rock temperature and fracture geometry and surface area in order to investigate their impact on heat transfer processes. Flow rate variations in the experiments have shown that higher flow rates cause the fluid to absorb less heat per unit volume and cause the rock to cool down more extensively, therefore thermal depletion of the reservoir is likely to occur within a shorter time frame. The dependency of exchanged heat on fracture aperture variations (in the range of 0.05 to 0.5 mm) did not yield a clear trend within the experiments, but does so in numerical simulations. Aperture variations in the numerical simulations did not cause notable differences in transferred heat as long as the volumetric flow rate is kept constant. However, as the fluid velocity is kept constant the amount of fluid flushed along the fracture per unit time is affected by varying apertures. This causes a difference in heat transfer as well. Increased fracture surface areas alone (more extensive topology/roughness) have shown a minimal impact on the heat production while a more extensive fracture network (additional branches) has shown notable enhancement in the amount of heat produced. Cooling behavior of the rock has shown correlations with Newton's law of cooling and suggests a limitation of heat production by the heat conduction occurring within the rock.

Experimental findings cannot directly be compared with natural reservoir conditions. The reason for this is a thermal equilibrium that is achieved at each flow experiment, i.e., the heat withdrawn equals the heat resupplied by a heater. In natural reservoirs this is often not the case where a cold front propagates towards the production well and determines the lifetime of how long heat can efficiently be produced from a certain rock mass. This results in an unsteady heat conduction where the heat withdrawn does not equal the heat resupplied.

Keywords

Geothermal energy, Heat Transfer, Fractures, Laboratory experiments, Numerical simulations, Flow rates, Heat conduction, Heat convection, Heat advection, Fracture aperture, Fracture surface area, Fracture geometry, Enhanced geothermal system, Stimulation, Hydraulic fracturing

List of Abbreviations and Terminology

EGS	Enhanced Geothermal System
ΔT	Temperature difference between inlet and outlet at steady-state flow condition
ΔT_{in}	Temperature difference between no-flow and steady-state flow condition at the inlet
ΔT_{out}	Temperature difference between no-flow and steady-state flow condition at the outlet
ΔT_{sample}	Temperature difference between no-flow and steady-state flow condition at the sample
CT	Computed Tomography
PT	Pressure Temperature
COMSOL	COMSOL Multiphysics® (Numerical finite element package software)
Exp	Experiment

Steady-state flow conditions	=	steady-state heat transfer	=	thermal equilibrium
Unsteady heat transfer	=	non-equilibrium		
Tensile fracture	=	mode I fracture		
Heat transfer	=	heat exchange		
Sub-experiment	=	each time range when a continuous constant fluid flow is imposed during an experiment in the triaxial apparatus		

List of Figures, Tables & Equations

1. Introduction

The essence of geothermal energy is heat generated and stored in the Earth that is produced as thermal energy. Geothermal energy in the Earth's crust originates from the formation of the planet and radioactive decay of materials (Dye, 2012). The temperature difference between the subsurface and the Earth's surface poses an enormous energy potential. It was estimated that the total thermal energy above mean surface temperature to a depth of 10 km is 1.3×10^{27} J. This amount of energy is equivalent to burning 3.0×10^{17} barrels of oil and would theoretically suffice to supply all of mankind's energy needs for six million years (Wright, 1989). This energy potential can be used by the means of heated fluids produced from the subsurface generating electrical power or providing direct-use heating for houses and industry (Lund et al., 2008).

Geothermal energy has attracted increasingly more attention in the last few decades. Some favorable characteristics of geothermal energy include reliability, renewability, low-carbon solutions, reduced environmental impacts and abundant availability around the world (Glassley, 2014). Fossil fuels still account for the largest and most efficient energy source nowadays but comes at a high environmental cost and is only renewable over time periods in the range of millions of years (Covert et al., 2016). This is why alternative energy solutions such as geothermal energy are necessary nowadays.

Different types of geothermal energy sources exist or can be engineered respectively. Liquid-dominated geothermal reservoirs are commonly found near young volcanoes surrounding the Pacific Ocean, occur in rift zones and mantle hot spots. The temperatures of such reservoirs are usually above 200 °C and a fluid circulation is usually naturally present without artificial pumping required (Moore et al., 2013). Another type is the direct-use thermal energy reservoir. These are commonly found in permeable sedimentary layers with lower temperatures and the energy extracted is used for direct heating rather than electrical power generation (Lund et al., 2005). Lastly, partly engineered systems called Enhanced Geothermal Systems (EGS) are used for deep geothermal energy production. Initially impermeable basement rocks are made permeable for fluid circulation by the means of stimulation techniques (e.g. hydraulic stimulation). EGS reservoirs are regionally less dependent on specific geological settings and are considered nearly ubiquitous (Moore et al., 2013). Due to these characteristics, certain reservoirs initially thought not to be suitable for geothermal production can be developed with this concept of EGS. All further discussion and work conducted within the framework of this project focus on Enhanced Geothermal Systems.

The temperature gradient in the Earth's crust varies highly by the location and geological setting with an average thermal gradient of 25-30 °C/km (Fridleifsson et al., 2008). However, there are areas with much higher thermal gradients such as parts of southern Australia, the regions of Alsace (eastern France) and Rhineland-Palatinate (western Germany) and active volcanic areas situated in subduction or rift zones (Olasolo et al., 2015). A classification was made with three different resource quality levels of potential reservoirs (low-grade, medium-grade, high-grade) with an estimated geothermal gradient of 30 °C/km, 50 °C/km and 70 °C/km respectively. The higher the resource quality level is, the more suitable the location is for the development of an EGS (Beckers et al., 2014). As a general rule the permeability decreases as pressure increases. Pressure (P) increases with depth (z) proportional to the density of the subsurface material (ρ) (Khoshnaw et al., 2015). Therefore, the greater the depth is the lower the permeability becomes (Stober, 2011). Combined with a rock type (typically granite) with a very low porosity, EGS reservoirs are initially only partly saturated with fluids and almost impermeable (Brown et al., 2012). This is why a common procedure of engineering a geothermal reservoir is to make use of certain treatments to enhance productivity in EGS. Common treatments include thermal, chemical and hydromechanical/hydraulic stimulation (Huenges, 2016). This project lays its focus on the treatment of generating fractures in addition to expanding the existing fractures by the means of hydraulic stimulation ("hydro-frac"). This technique is well known and commonly used in the oil and gas industry. These additionally generated and/or expanded fractures therefore allow a confined fluid-circulation loop. Cold water is injected into the reservoir under high hydraulic pressures such that new fractures are forming and existing fractures are expanded. These fractures serve as fluid pathways across the reservoir to the production well. The hot water is pumped to the surface through a production well where the thermal energy is extracted. The now cooled water is reinjected through an injection well into the hot fractured basement rock again (Brown et al., 2012). A conceptual sketch of a closed-loop EGS is depicted in *Figure 1.1*. One injection well is placed in the middle with 2 production wells on each side in a fractured reservoir in approximately 4 km depth in this example.

Introduction
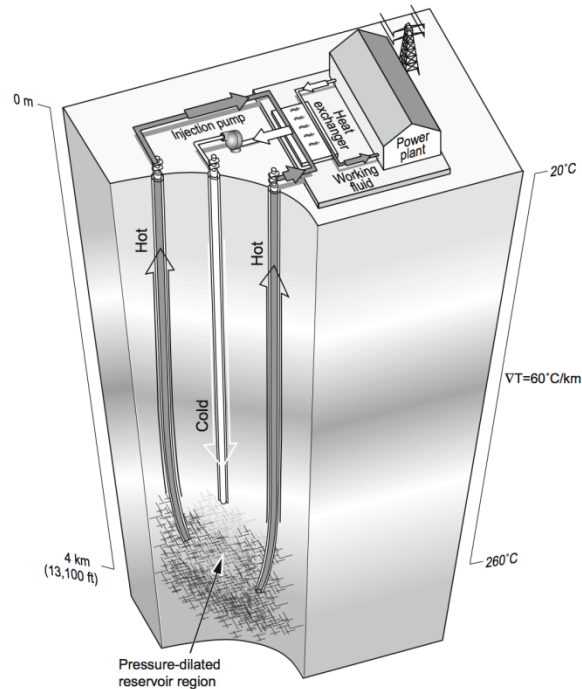
Fig 1.1: Conceptualization of an EGS (Brown et al., 2012)

The permeability of fractures is an important parameter which determines at what velocity subsurface flow occurs or whether flow can occur at all. Unlike reservoirs with pre-existing permeability in porous layers, EGS reservoirs rely completely on generated and expanded fractures as the major fluid pathway. Therefore, it is crucial to control the permeability at reservoir scale by applying suitable pore fluid pressure (injection pressure) which alters the difference between confining rock pressure and pore fluid pressure. As this pressure difference decreases (E.g. by increasing the pore fluid pressure) the fluid pathways (fractures in this case) are increasingly expanding in volume and aperture (Walsh, 1981). A sufficient fracture width/aperture then allows fractures to act as efficient fluid pathways. In EGS, it is attempted to reach a large fraction of the reservoir with circulating fluids. A broad fracture network throughout the reservoir is desirable because it increases the total surface area with which fluids come in contact with the thermal reservoir rocks. This fracture surface area is where heat exchange between solid and fluid occurs. Predominant heat transfer processes in EGS are thermal conduction within the solid rock and convection/advection in the fluid circulating the rock. The link between these two processes must be provided by a large contact area, e.g., fracture surfaces. The velocity of the fluid flowing along the rock surface then determines how long a certain volume of fluid comes into contact with a certain reservoir rock surface area and therefore how much heat-energy can be taken up by the fluid volume before exiting the reservoir. Therefore, at low flow rates the fluid velocity is smaller too and thus there is "more time" for heat exchange. The heat energy taken up by a certain volume of produced fluid is then relatively high while the produced fluid volume per unit time is relatively small. On the other side, at high flow

rates there is "less time" for heat exchange. Thus, the heat energy taken up by a certain volume of produced fluid is relatively small while the produced fluid volume per unit time is relatively high.

A part of this thesis project is to show whether varying fracture surface areas cause differences in heat exchanged. Another part is to show that fluid absorbs different amount of heat with altering velocities and therefore varying fluid-rock contact times. As depicted in *Figure 1.2,* fluid velocities along fractures also vary individually since natural fractures are never perfectly planar but rather possess individual unpredictable geometries (Luo et al., 2017).
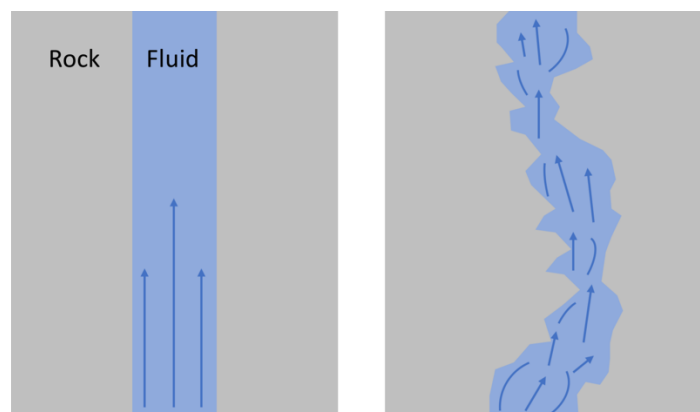
Fig 1.2: Concept of fluid saturated pathways in the rock (fractures) and their flow behavior. On the left, a perfectly straight fracture imposes a straight laminar flow. On the right, a more natural fracture with a chaotic geometry imposes a more chaotic flow with varying velocities and flow regimes.

This master thesis project focuses on the heat exchange processes between rock and fluid at depth occurring in EGS. Geothermal power plants of this kind are still rare at this point despite their enormous potential (Goldstein et al., 2011). To stress this enormous potential, for example, it has been estimated in 2013 that the total heat available in the crust of the earth is around 540×10^7 EJ (EJ = Exajoules = 10^{18} J) (WEC, 2013). In case just 1% of this amount is used to meet global energy needs (around 500 EJ per year) the world would be provided with all energy required for 2800 years at a constant consumption rate (Olasolo et al., 2015). Successfully operating electricity-generating small-scale EGS plants are, for example, located in Soultz-sous-Forêts, France (1.5 MWe) and in Landau (3 MWe) and Insheim (4.5 MWe) in Germany (Goldstein et al., 2011). A former EGS project that was abandoned lay in a remote part of South Australia with temperatures of up to 250 °C in a depth of around 4 km (Bendall et al., 2013). Several sites in the USA are also investigated for EGS resources, where existing hydrothermal reservoirs are expanded by stimulating their edges. Extensive further research is still required to optimize energy production and also make such plants financially viable in less favorable areas by the means of improving production technology, heat exchange and stimulation techniques and energy conversion processes at the surface. For example, research and experiments have been carried out on hydraulic and heat transfer properties of artificially fractured granite (Luo et al., 2017). Similar to this thesis project, Luo et al. also used non-permeable granite in their studies where the entire fluid flow is

Introduction

occurring along the generated fracture (2017). It was shown that the hydraulic conductivity is proportional to the fracture aperture. However, their studies on heat transfer within the fracture was limited to varying the rock temperature. It was shown that thermal energy production could significantly be improved at high rock temperatures. Additionally, this master thesis aims to study the effect of different fracture topologies on heat exchange at constant reservoir temperatures. Varying fluid flow rates along fractures and varying fracture apertures and therefore permeability is expected to result in different thermal efficiencies. Other studies include a modelling-based work of flow and/or heat transfer in fractured rocks without an experimental component such as the work of Kolditz (1995) or Kissling et al. (2015). Most of these studies are carried out at the reservoir scale such as the numerical study of flow and heat transfer of Hao et al. (2012) rather than at the sample scale. Most examinations within this thesis occur in an experimental and numerical setting at the sample scale and are attempted to be upscaled to reservoir scale. In the framework of this project, sample scale is in the range of centimeters (heat exchange along a fracture with a length of approximately 5 cm) and reservoir scale is in the range of kilometers.

There is an enormous body of publications about EGS research. This is also stressed in the work of Olasolo et al. (2015) referring to many other publications in this area in the reference list. However, at experimental scale there is still a lot to investigate. The main motivation and goal of this thesis topic is to understand heat transfer in fractures and apply the yielded knowledge at reservoir scale. Based on existing knowledge and literature the thermal efficiency is hypothetically dependent on the fracture surface area that the fluid injected into the subsurface comes in contact with. Another hypothesis is the significant dependency of thermal efficiency on fluid velocities. It is therefore important to carefully choose pore fluid pressures and injection flow rates in a subsurface system which is correlated with the occurrence of artificially generated fractures and therefore a varying rock contact surface area. These hypotheses are to be tested within the framework of this thesis.

The main research objective of this thesis is therefore to show the impact of varying fracture geometries/topologies and areas on the heat exchange between rock and fluid. In order to answer the main research question, following sub-research questions are formulated below. Each research question is investigated by means of laboratory experiments as well as numerical models with the software COMSOL Multiphysics. Numerical models mainly serve to back-test and simulate experiments throughout a larger range of parameters.

- **How and to what degree do varying flow rates/fluid velocities change the amount of heat exchanged between fluid and solid along naturally formed fractures (in situ tensile (mode 1) fractures)?**

  The imposed volumetric flow rate along the artificially generated fracture is the only parameter varied to answer this research question. Essentially, experiments are run in which a fluid is forced along a fracture at different velocities under pressure. The temperature changes are measured to answer this question.

- **How do different fracture geometries affect the amount of heat exchanged between fluid and solid along the fracture?**

  Each generated fracture has an individual geometry and surface area that is difficult to predict precisely. The surface of fractures is where heat exchange between fluid and solid occurs. Individual geometries can hamper fluid flow and alter fluid velocities along the rock surface. Fluid velocities are not constant along the fracture plane because of the laminar flow profile and irregular geometries. A correlation is established between individual surface areas and their corresponding heat exchange behavior.

- **Does varying the fracture width/aperture have an impact on heat exchange at constant flow rates and constant fluid velocities?**

  As the fracture aperture is increased, the permeability is increased and lower local fluid velocities along the fracture at constant flow rates occur. If the injection fluid velocity is kept constant, the volumetric flow rate is changing with varying fracture aperture. The amount of fluid being in contact with the fracture surface and the time a certain volume of fluid is exposed to the hot rock depend on the flow rate and velocity.

2. Methodology

Fracture properties and fluid flow behavior is investigated on granite rock specimen. A triaxial deformation apparatus is utilized to fracture rock samples and generate a pathway for fluid flow under relevant pressure and temperature (PT) conditions. A total of eight experiments were conducted with the triaxial deformation apparatus, of which six involved fracturing of the rock sample (Experiments 1 – 6). The remaining two experiments were conducted with samples that contained a pre-drilled fluid pathway (Experiments 8 – 9). The results of Experiment 7 were not used in this thesis due to unstable temperature conditions during the experiment, but can be found in the appendix. Furthermore, fracture geometry investigations are conducted with a micro-CT scanner that yields 3D x-ray images of the rock samples. Flow and temperature conditions observed during the experiments with the triaxial setup are simulated with a numerical finite element package (COMSOL Multiphysics®).

2.1 Description and properties of the samples

The examined rock originates from a granite quarry in Odenwald, Germany (RÖHRIG Granit GmbH, GPS coordinates, 49.633071, 8.700709) and sufficiently reflects rock compositions as found in upper crustal conditions (most commonly below the sedimentary cover). This rock is coarse-grained with fully crystallized and visible minerals up to 5 mm in size. Comparable intact granitic rocks were found to have a porosity of about 1% and a permeability of $< 10^{-18}$ m^2 in literature (Selvadurai et al., 2005). The permeability of non-fractured specimens is therefore negligible.

In addition to determining the rock density by simply measuring its weight and volume as shown in *Table 2.1,* the density is also measured with a so-called density determination kit.

With this method, the density of a solid is determined with the aid of a liquid (distilled water) of which the density is known. The solid (in this case the rock sample) is weighted in air (A) and then emerged in the auxiliary liquid (B). The density of the solid can then be calculated from the two weightings as follows:

$$\rho = \frac{A}{A-B}(\rho_0 - \rho_L) + \rho_L \qquad \text{(Eq. 1)}$$

where ρ is the density of the sample, A the weight of the sample in air, B the weight of the sample in the auxiliary liquid, ρ_0 the density of the auxiliary liquid and ρ_L the density of air (0.0012 g/cm^3). Considering the temperature dependent density of distilled water (997.54 kg/m^3 at 23 °C) according to Kell (1975), A being 41.54 g and B being 26.46 g, the density of the rock sample was determined to **2745.6 kg/m^3**.

The thermal conductivity of the rock sample was determined using a C-Therm Thermal Conductivity Analyzer® located in the laboratory of the Aerospace Faculty at TU Delft. This analyzer consists of a metal spiral on a flat surface where the sample (also a flat surface) is placed on. Wetting (with distilled water) of the contact surface ensures no void air space between the measuring surface and the sample. The metal spiral is then heated by a few degrees Celsius. Heat conduction transfers energy from the metal spiral along the sample material to the adjacent temperature sensors. In this way the thermal effusivity as well as the conductivity are directly measured. Usually ten measurements are conducted on one sample, then taking the average result from all measurements. It was found that the thermal effusivity of the granite sample is **2444.26 W*s$^{1/2}$/m^2/K** and the thermal conductivity is **2.918 W/m/K**.

From these two parameters, the heat capacity can be derived according to the following equation:

$$C_p = \frac{e^2}{k*\rho} \qquad\qquad\qquad \textit{(Eq. 2)}$$

where C$_p$ is the heat capacity of the sample, e the thermal effusivity, k the thermal conductivity and ρ the density. Plugging all previously determined parameters into the equation yields a heat capacity value of **745.71 J/kg/K**.

All above-listed properties are determined at room temperatures (23 °C) and are considered fairly constant over the temperature range in which later experiments are conducted.

These experimentally determined rock properties are used for the numerical simulations which are elaborated in *Chapter 2.9*. The same property-determining experiments and calculations are conducted for other relevant materials used in this project (rubber jacket, steel wedges). A complete table in *Chapter 2.9.3* lists all material properties used in the numerical simulations.

2.2 Preparation of the samples

Pieces of cylindrically shaped rock specimen were cored out of a larger single block of granite, to limit variability. The diameter of the cores is approximately 30 mm. These cores were then cut to an individual sample length of approximately 50 mm with a diamond blade saw. If needed, the top and bottom surfaces were polished off to provide a smooth surface to ensure an equal distribution of load on the sample during experiments. The preparation of all samples to be fractured (Experiments 1 – 6) is hereby finished. A special exception poses the sample used for Experiment 6. It was initially intended to be part of the benchmarking experiment series. It was cut apart with a diamond-blade saw along the middle in axial direction to provide a perfectly straight and smooth artificial "fracture". However, due to misplacement in the triaxial testing apparatus it was further fractured as explained in *Chapter 2.4*. Therefore, Experiment 6 was adopted into the category of fractured sample experiments. The abnormally extensive fracture network of this sample was

considered for geometry and surface area analysis. Due to the time constraint of the thesis and limited availability of laboratory facilities, a correctly conducted saw-cut sample benchmarking experiment could unfortunately not be repeated.

The rock sample that was used for the benchmarking Experiments 8 and 9 was further prepared. A straight and smooth hole was drilled along the middle in axial direction with a diameter of 4 mm. This is why it is called the "drilled-hole sample" that was used for both benchmarking experiments. Within the framework of the benchmarking experiments, simple and predictable fluid pathway geometries shall be compared with naturally formed fractures with complex geometries. The goal of benchmarking experiments in this project is to yield experimental results where the conditions are perfectly known. The flow regime is perfectly laminar and occurs along a smooth and symmetrical flow pathway of which the width and volume can accurately be measured. Benchmarking experiments are based on fewer assumptions and results can be considered more accurate. *Figure 2.1* depicts the fully prepared sample for the benchmarking experiments. The metal cylinders placed on top and bottom of the sample are part of the experimental assembly explained in *Chapter 2.3*. Instead of steel wedges used in Experiments 1 – 6, flat steel cylinders are used in Experiment 8 and 09 to ensure no fracturing of the rock sample occurs inside the testing apparatus.

Fig 2.1: Rock sample with a drilled hole in the middle and steel cylinders placed on top and bottom of the specimen during Experiments 8 and 9. Prepared rock samples for the fracture Experiments 1 – 5 are identical except the drilled hole.

Pre-experimental measurements on all rock samples are carried out. Length, diameter and weight (except Experiment 1 – 4) are quantified. From these values, the sample volume and density are calculated. *Table 2.1* lists all parameters.

Experiment	1	2	3	4	5	6	8 / 9
Length (mm)	46.40	49.85	49.30	48.40	47.65	46.90	49.32
Diameter (mm)	29.70	29.30	29.30	29.30	29.25	29.30	29.34
Weight (g)	-	-	-	-	87.85	86.90	88.86
Volume (mm³)	32146	33612	33241	32634	32019	31623	32662
Density (kg/m³)	-	-	-	-	2744	2748	2721

Table 2.1: Measurements and derived volume and density of all prepared pre-experimental rock samples.

2.3 Experimental Setup

In the present work, the testing system consists of a triaxial deformation apparatus located at the Delft University of Technology. This cylindrically shaped apparatus is equipped with an internal oven/furnace and is designed to achieve reservoir PT (Pressure and Temperature) conditions. The cell pressure can be set as high as 70 MPa and the optional furnace can be heated to temperatures as high as 200 °C. All experiments were carried out at a cell pressure of 10 MPa and equilibrium temperature conditions of 100 °C, except for one benchmarking experiment where only 60 °C was reached. One experiment was run at only 60 °C in order to see temperature dependent variations in heat production. While in uniaxial deformation tests only axial stress in one direction is applied, triaxial testing additionally allows radial pressure to be applied on the sample by filling the space around the sample with oil and pressurize it. A rubber jacket fitted around the rock sample ensures that the pore fluid inside the sample does not come into contact with the oil-pressure outside the sample. For all experiments in the triaxial deformation apparatus the cell/confining or radial pressure (P_{cell}), the axial load (σ_a), the differential pore pressure (P_{diff}), the radial deformation (ε_r) and the axial deformation (ε_a) are measured. Additionally, temperatures at 3 different points around the sample are recorded which include the outlet fluid temperature at the top of the sample (T_{out}), the inlet fluid temperature at the bottom (T_{in}) and the sample temperature outside of the rubber jacket (T_{sample}). Both thermocouples at the inlet and outlet are embedded within the pore fluid lines which makes this setup rather unique. It is also important to note that the metal wedges are placed between the rock sample and the inlet and outlet thermocouple respectively. The axial deformation (ε_a) is measured by means of two LVDTs (linear variable differential transformers) placed on two opposing sides of the sample. Radial deformation (ε_r) is measured by a chain-type extensometer placed around the sample.
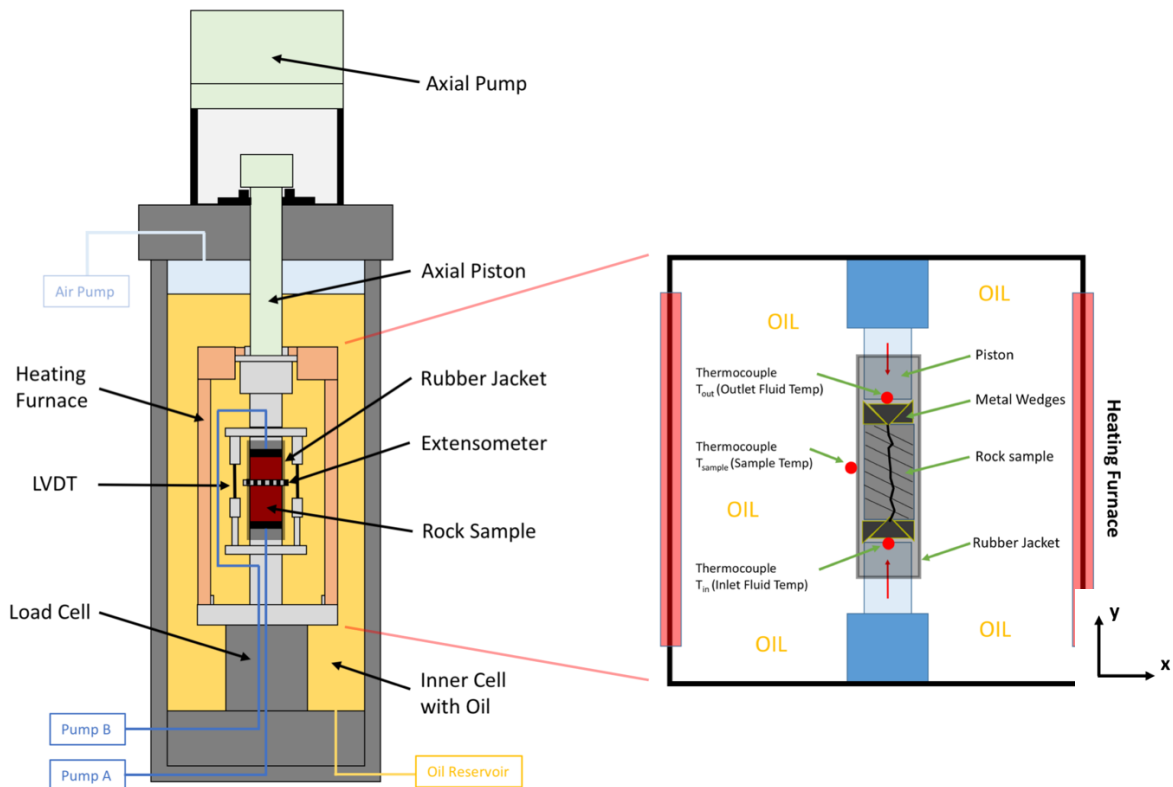
Fig 2.2: 2D cross-section of the entire apparatus on the left and the zoomed in sample assembly on the right. Due to practical reasons, the LVDT's and the extensometer is not depicted in the zoomed in section.

The rock sample sits between two steel pistons at the top and bottom. Between each piston and the sample, steel wedges which allow relative movement in respect to each other are placed. These steel wedges are aligned in such a way that a fracture lying along y-direction (see *Figure 2.2)* is generated upon applying high axial load. Essentially, a line load is applied by the steel wedges on the rock sample to force a mode 1 fracture. This load however is uncertain since frictional forces between the steel wedge holders and the rock are unknown. It is purely a way for force a mode 1 fracture. Instead of steel wedges, flat steel cylinders as shown in *Figure 2.1* are utilized in the benchmarking experiments. This ensures a stress distribution over the entire top and bottom surface of the rock sample, so that fracturing does not occur within the present experimental conditions. The lower steel piston sits on a load cell while the upper piston is connected to the controllable axial piston which applies axial load on the sample. The assembly including the rock sample, steel wedges/cylinders and part of the top and bottom pistons is jacketed. O-rings attached to the bottom and top of the assembly prevent oil leakage into the sample during the experiments. Once the jacketed sample and the instrumentation is setup, a cylindrical heating furnace resting inside the pressure cell is lowered over the sample assembly to cover it completely. The heating furnace with the sample assembly including the load cell and the bottom plate (see sketch in *Figure 2.2* for details) are then mechanically lifted upwards into the pressure cylinder. Before mounting the sample assembly into the pressure cell, one needs to make sure that all connections are properly attached and the measurement tools are set into the measurement range and

the heating furnace is properly fitting. A connection then needs to be established between the axial loading piston and the top of the sample assembly by lowering the axial piston by means of a hydraulic hand pump. This is done manually to avoid a load overshoot in automatic pump control which could break the sample prematurely. The air inside the pressure cell then needs to be replaced by oil. Heat resistant oil from a reservoir is pumped into the pressure cell from the bottom up while the air is pushed out through an outlet at the top. In order to remove the oil after every experiment, the oil is pushed out of the pressure cell back into the reservoir by applying air pressure from the top. Radial pressure is then gradually applied on the rock sample by compressing the oil in the pressure cell by means of a pressure intensifier. At the same time, axial pressure is manually increased with the hand pump to ensure a hydrostatic loading of the sample. Once the desired confining pressure of 10 MPa and an approximate corresponding axial load of 8 kN is reached, the sample is ready to be fractured. By checking the value of the extensometer during the test we assume the rock is still in-tact. It is aimed to start at hydrostatic no-flow conditions but this cannot be accurately determined.

2.4 Tensile Fracturing
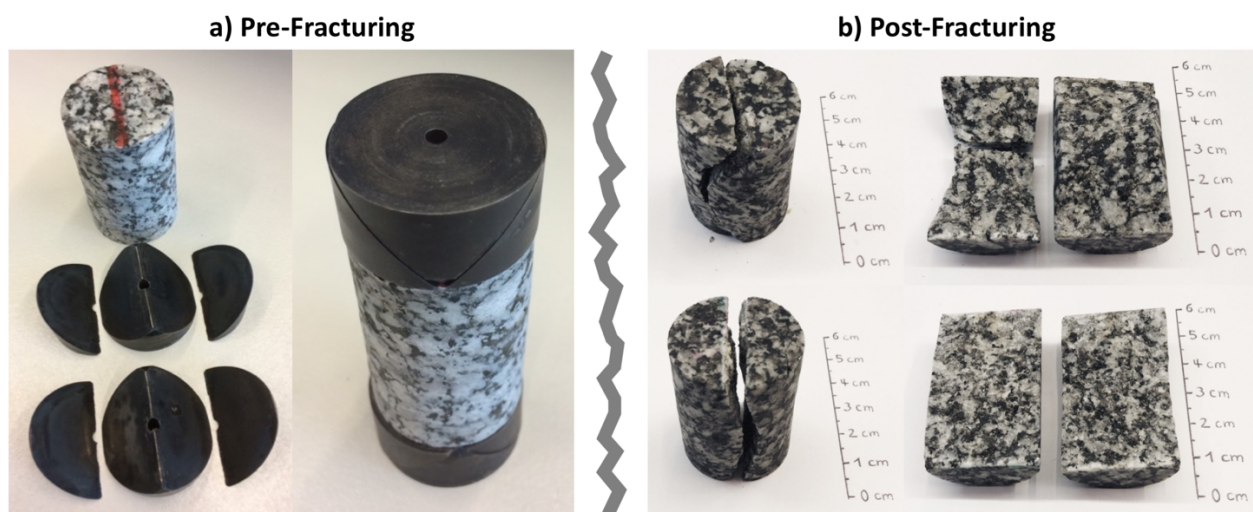
Fig 2.3: In-tact rock sample marked for accurate placement of the wedges (left photo of panel *a)*) and steel wedges on top and bottom of the sample ready to be placed into the experimental apparatus (right photo of panel *a)*). Panel *b)* depicts the appearance of fractured rock samples (Top: Experiment 5; Bottom: Experiment 4). Every fracture is unique and resulting fracture patterns vary.

As already described in *Chapter 2.3* steel wedges (also called "mode I frackers") sit on top and bottom of the sample of Experiment 1 – 6 (see *Figure 2.3*). This chapter does not apply for the benchmarking experiments. Each of these fracker assemblies consist of a wedge and two counterparts which make up a cylinder of 15 mm length. In the middle of this cylinder a hole with a 3 mm diameter is located to allow fluids to pass from the sample to the pore fluid lines. Their function is to focus the entire axial stress applied on the sample along one line on a small area which initiates a crack on the rock. Since the wedge assemblies are on both sides of the

sample and the crests of the wedges are aligned parallel to each other, the stress field is such that a single close-to-planar shaped fracture is most likely to occur. This is comparable with a common test in rock mechanics; the Brazilian disk tensile strength test. There the rock is also broken with a line-load (Jaeger and Hoskins, 1966). In order to break the sample, axial pressure is increased on the sample using the hydraulic hand pump. The crests of the wedges carve into the sample and load is continuously increased until measurement tools indicate the sudden generation of a fracture and therefore brittle failure. This way a mode 1 type fracture is forced to open. Mode 1 leads to a continuous opening across the rock sample and thereby provides a fluid pathway (Paterson and Wong, 2005). Fracture modes II and III do not lead to an opening and are therefore not suitable for the experiments in this project (see *Figure 2.4*).
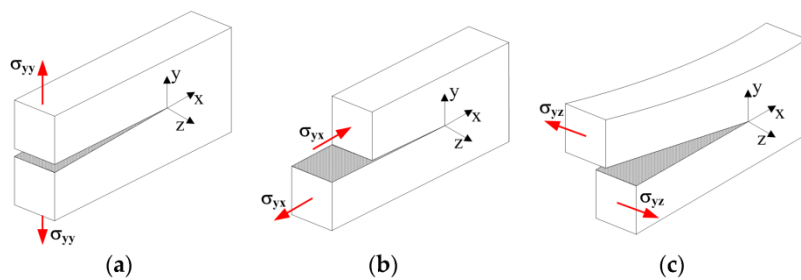
Fig 2.4: a) Fracture mode I (opening or tensile mode). b) Fracture mode II (sliding or in-plane shear mode). c) Fracture mode III (tearing or anti-plane shear mode). (Golewski, 2017)

Prior to the experiment, a thin film of grease is applied on the steel wedges and their counterparts on the contact area to assure smooth sliding between the wedge and its counterparts. Cracking of the sample is indicated by a sudden and significant increase of the radial displacement which is measured by the extensometer chain. Another indicator of successful fracturing is air being able to flow along the entire pore fluid system since there is now a connection between inlet and outlet of the sample. Prior to fracturing a vacuum pump is connected to one end of the pore fluid line. As soon as suction of air is achieved on the other side of the pore fluid line, there is a continuous connection, i.e., an open fracture. The relationship between the measured extensometer value of the sample before the experiment and after fracturing is assumed to show an approximate fracture aperture. It is a change of circumference due to an opening caused by the wedges. Changes of the circumference between post-fracturing and further testing are assumed to be fracture aperture variations. It is important to note that controlled fracture aperture variations are conducted only in Experiment 2 and 6. For all other experiments, the fracture aperture is considered fairly constant throughout the entire experiment. The "parallel plate" theory is considered, assuming a single straight fracture from one wedge to the other without irregular surface topography. This assumption is required to conduct calculations based on the experimental data such as fluid velocity and permeability.

2.5 Fluid flow across the sample and heating of the system

In order for fluids to be able to flow across the sample, an open fracture/fluid pathway must be present in the otherwise practically impermeable granitic rock. Demineralized water is used due to its thermal properties and viscosity easily to be determined and its non-precipitative behavior. After fracturing, the pore fluid lines and the fracture are flushed with water until full saturation is reached assuming no major volumes of air is left in the pore fluid system. Pumps to drive the fluid flow are two ISCO Syringe Pump 100 DM, with a flow rate accuracy of $\pm$ 0.3% (maximum 0.25 µl/min seal leakage; ISCO 100DM manual, 2009). Flowrates (Q) and fluid volumes (V) of both pumps A and B are measured and logged along other parameters mentioned in *Chapter 2.3*. A constant flow rate is set on one pump, e.g., pump A and a constant fluid pressure of 10 bar (back pressure) is maintained with the other pump, e.g., pump B. The fluid volume leaving one pump should then be equal to the volume arriving at the other pump. If this is not the case, a leak along the pore fluid line is likely. This procedure allows to set desired flow rates ranging from 2 ml/min to 12 ml/min over a period of time until the total pump volume of 100 ml is exhausted and needs to be refilled again. The flow occurs only in one direction and the water is disposed after each run. This procedure ensures that the fluid is kept clean and contains no mineral/rock particles. The pressure differential P_{diff} shall linearly increase with increasing flow rates. This behavior confirms a steady-state fluid flow without a leakage in the system.

For the experiments conducted within this project, the system including the sample assembly is heated up to a target temperature of 100 °C (or 60 °C in Experiment 9). After setting the heating furnace to the target temperature, it takes about 30-60 min for the system to be in thermal equilibrium ready to start flow experiments. In the present experimental apparatus, thermal equilibrium does not imply same temperatures at all measurement points but rather temperatures that do no change in time anymore at each measurement point. This state of equilibrium shall be achieved every time before imposing a fluid flow. A flow of water initially at room temperature is then imposed on the pore fluid lines at a constant flow rate over a duration of approximately 10 min. After this time frame the cooling usually reaches the confining pressure oil and thereby the whole triaxial cell. In response, more power is conducted to the furnace triggered by the thermal regulator that recorded lower temperatures. Therefore, the time scale of 10 min is long enough to reach a steady-state heat exchange between rock and fluid, but short enough to avoid the influence of the oven. The steady state condition is mentioned in the following *Chapter 2.6*. It states that the temperature change at each thermocouple is below a certain rate to be considered steady state. Flow experiments are repeated at several constant flow rates. Each constant flow rate imposed on the sample within the frame of the same experiment is called sub-experiment. At least 3 and up to 9 such sub-experiments were conducted within every experiment of this project. *Figure 2.5* depicts the temperature equilibrium approach at a constant flow rate. A large non-linear temperature gradient can be seen between the different thermocouple measurements before flow and

during flow condition. This temperature gradient in the experimental assembly even at a steady state temperature approach was initially not expected to occur. Even after checking the proper functioning of the entire apparatus, the undesired temperature gradient could not be overcome. In order to explain such temperature gradients, additional numerical simulations were run. The outcomes and possible reasoning of the experimental and numerical temperature gradients between thermocouple locations are shown and discussed in *Chapter 3 and 4*.
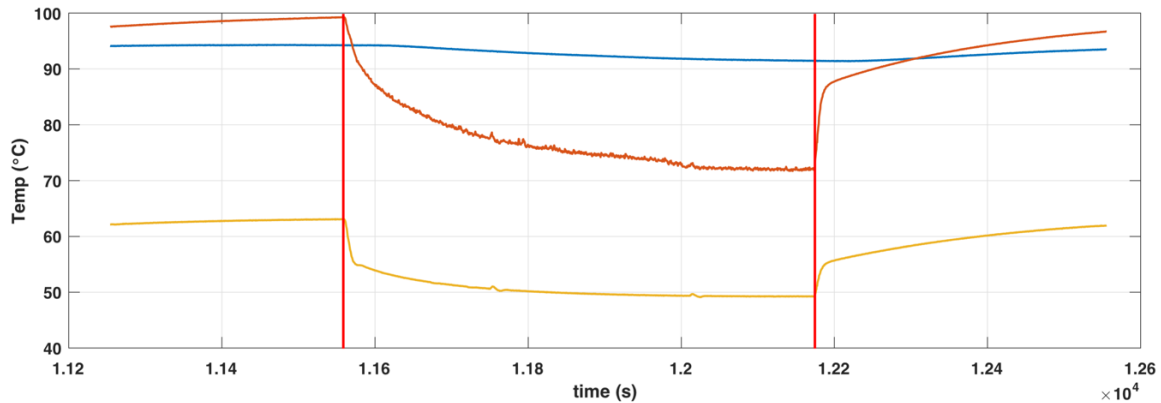
Fig 2.5: A flow rate of 8 ml/min is imposed at the point where the temperature curves start to drop until the point where the temperature is increasing again (approximate time frame between red markings is 10 min). T$_{sample}$ is blue; T$_{out}$ is red; T$_{in}$ is yellow. A steady temperature is reached at the end of the flow period (Experiment 6).

2.6 Data Analysis with MATLAB

Continuous data logging during the experiments returns a ".log" text file with values of relevant parameters described in *Chapter 2.3* and *2.5* at every time step of 0.5 seconds. Equations used for initial permeability and heat capacity calculations are described below.

2.6.1 Permeability Approaches

Permeability based on Darcy's law (Darcy, 1856) modified for the core sample assuming dP/dx can be approximated by ΔP/L:

$$K_D = \frac{Q*\mu}{A} * \frac{L}{\Delta P} \qquad\qquad (Eq.\ 3)$$

where K_D is the Darcy Permeability (m^2), Q the flow rate of the fluid (m^3/s), A the cross-sectional area of the sample (m^2), μ the dynamic viscosity of the fluid (Pa*s), L the thickness of the bed or sample length (m) and ΔP the pressure difference across the sample (Pa).

However, permeability calculations based on Darcy's law are not a sufficient approach for the experimental conditions of this project. Darcy's law is suitable for porous media, but the majority of flow is concentrated to the generated fracture of the examined samples which can be considered non-porous. Hence, the approximation can be made that

$$A * K_{sample} = A_{matrix} * K_{matrix} + A_f * K_f \qquad \text{(Eq. 4)}$$

where $K_{sample} = K_D$, A_{matrix} is the cross-sectional area of the matrix (m²), K_{matrix} is the permeability of the matrix (m²) and A_f and K_f are the cross-sectional area and the permeability of the fracture respectively (m²).

Equation 4 is further reduced to

$$A * K_{sample} = A_f * K_f \qquad \text{(Eq. 5)}$$

assuming matrix permeability K_{matrix} is negligible in granite with < 10^{-18} m² (Selvadurai et al., 2005). Using the cross-sectional area of the sample and the fracture, *Equation 5* can be rewritten to

$$(\pi R^2) * K_{sample} = (2a_h) * K_f \qquad \text{(Eq. 6)}$$

where R is the radius of the sample or half fracture length (m) and a_h is the hydraulic fracture aperture (m²).

Assuming laminar flow in a parallel plate model according to the "cubic law", **fracture permeability based on the hydraulic fracture aperture** can be expressed in the following way (e.g., Hofmann et al., 2016):

$$K_f = \frac{a_h{}^2}{12} \qquad \text{(Eq. 7)} \quad \text{with}$$

$$a_h = \sqrt[3]{6 * \pi * K_{sample} * R} \qquad \text{(Eq. 8)}$$

Another approach for fracture permeability on the other side is considering only the mechanical fracture aperture. **Fracture permeability based on the mechanical fracture aperture** and cubic law is (Witherspoon, 1980):

$$K_f = \frac{a_m{}^2}{12} \qquad \text{(Eq. 9)}$$

where a_m represents the mechanical fracture aperture (m) as shown in *Figure 2.6*.
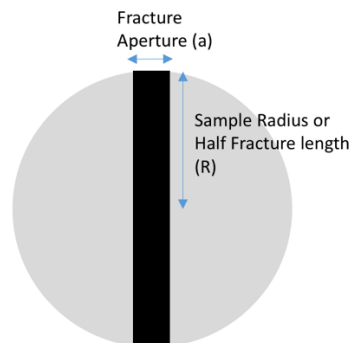
Fig. 2.6: Sample cross section with fracture

Methodology

It was shown that the permeability approach based on hydraulic fracture aperture is the most reliable measure to quantify permeability in the conducted experiments.

2.6.2 Potential Power Output

Another MATLAB script is computing the potential power output generated in Watt at a certain fluid flow rate. This approach is usually used in geothermal reservoirs where a well doublet is engineered, i.e., a pair of drilled wells that consist of one injection well and one production well. The temperature difference between the injected fluid and the produced fluid is then converted into an energy per unit time. It is expressed as:

$$P_{doublet} = C_p * Q * \Delta T \qquad \text{(Eq. 10)}$$

Where $P_{doublet}$ is the power output (W or J/s), C_p is the mass heat capacity of the fluid (J/g/K), Q is the mass flow rate (g/s) and ΔT is the temperature difference between inlet and outlet (K or °C) (e.g., Vik et al., 2018 or Willems et al., 2017). The mass heat capacity of liquid demineralized water is 4.184 J/g/K (NIST, 2018).

It is important to note that in the experiments within this project, the power production cannot be calculated with *Equation 10*. The reason is the non-uniformity of the sample temperatures during all experiments that pose a temperature gradient as mentioned in *Chapter 2.5*. The inlet/injection temperature shall also be kept constant for *Equation 10* to be quantitative which is not achieved during the experiments. In certain numerical simulations in which fairly constant temperature conditions are achieved however, *Equation 10* can be used.

2.6.3 Flow Regimes

Fluid flow regimes are important to estimate fluid flow behavior and, in this project, quantify heat exchange between the fluid and rock along the fracture. Turbulent flow would impose different heat exchange rates from laminar flow. Turbulent flow generally allows for more efficient heat exchange than laminar flow due to its multi-directional convective behavior. Laminar flow is a unidirectional convective flow, e.g., in axial direction while no mixing of the fluid occurs, e.g., in radial direction. Radial heat transfer in laminar flow therefore mostly occurs by conduction which generally is a slower heat transfer process than convection/advection. Turbulent flow on the other side is irregular and unpredictable. Heat transfer in radial direction therefore can also occur by convection, e.g., turbulent whirls (Patil et al., 2015). The Reynolds number is a dimensionless parameter to quantify the flow regime. An assumption made is that all fractures are fully filled rectangular ducts where the diameter or fracture length is much larger than the fracture aperture. The hydraulic diameter D_h (m) is then twice the mechanical fracture aperture a_m:

$$D_h = 2a_m \qquad \text{(Eq. 11)}$$

The **Reynolds number** can then be calculated with the following equation (Reynolds, 1883):

$$Re = \frac{\sigma_w * u * D_h}{\mu}$$ *(Eq. 12)*

Where σ_w is the fluid (water) density of 1000 kg/m³, u the fluid velocity (m/s) and μ the dynamic fluid viscosity (Pa*s).

In general, laminar flow occurs when Re < 2300 and turbulent flow occurs when Re > 4000. These transition values depend on the flow channel geometry and can vary (Schlichting and Gersten, 2017).

2.6.4 Exponential fitting curve and steady-state condition at fluid flow

The temperature at all three thermocouples decreases at a certain rate as soon as a fluid flow is imposed on the rock sample. This temperature decay occurs until the point when a stable thermal equilibrium is achieved. In order to express this decay curve in terms of a mathematical function, an **exponential fitting curve** is applied in MATLAB. In general, an exponential cooling/decay can be expressed by the following equation, where T is the temperature, t is the time and λ (lambda) is a positive rate called the exponential decay constant:

$$\frac{dT}{dt} = -\lambda T$$ *(Eq. 13)*

The solution of *Equation 13* is in this specific case:

$$T(t) = (T_0 - T_{end}) * e^{-\lambda t} + T_{end}$$ *(Eq. 14)*

where T_0 is the starting temperature at the point a certain flow rate is imposed and T_{end} is the stable thermal equilibrium. In MATLAB *Equation 14* is defined as:

$$f(x) = a * \exp(-bx) + c$$ *(Eq. 15)*

where the variables a, b and c are specifically computed for each set of values in order to get a best-fitting curve. Exponential fitting curves of selected sub-experiments are shown and evaluated in *Chapter 3.1.4*. Correlations between different sub-experiments are established in terms of their cooling behavior.

In order to evaluate whether a **steady-state condition** with constant temperatures is reached at each flow sub-experiment, temperature variations at each thermocouple of the last 60 seconds are analyzed. A steady-state condition in terms of temperature change occurs when the variation in temperature is less than 1% in correspondence to the mean value within the last 60 seconds of a sub-experiment. 1% variability from the mean is assumed to be a reasonable value to proof steady state. A steady-state check of each sub-experiment is conducted and presented in *Chapter 3.1.4*. In order for experimental results to be significant and comparable with each other, the achievement of steady-state or near-steady-state conditions are favorable. *Figure 2.7* visualizes the range where the temperature values are compared with each other to determine steady state.
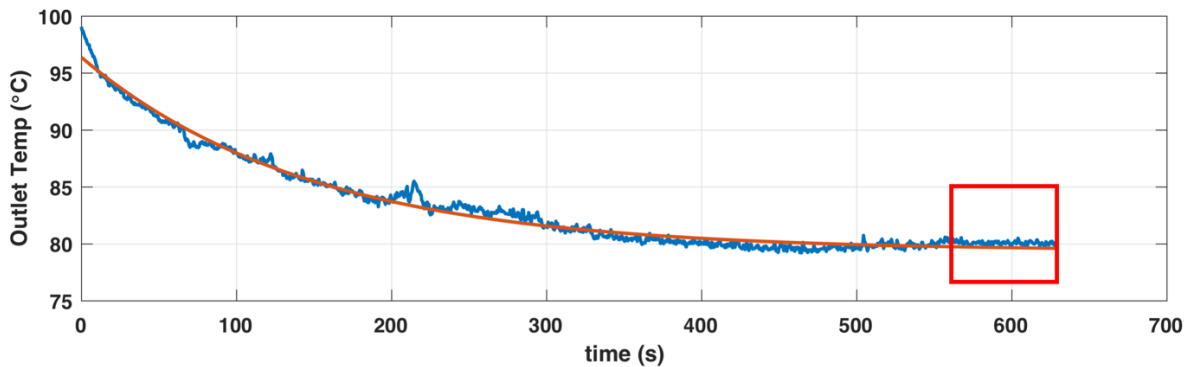
Fig 2.7: An example of a temperature decay curve (blue) and its exponential fit (red) at the fluid outlet at 6 ml/min in Experiment 5. Steady-state check is performed in the last 60 seconds of a flow experiment (red box)

2.7 X-Ray Micro CT Scanning

After experiments each rock sample undergoes a computer tomography with a NANOTOM high resolution CT (Computed Tomography) Scanner located in the Geoscience Laboratory at TU Delft. The scanner uses an x-ray-source of 180 kV and 15 W. The minimum focal spot size is < 0.9 μm and the maximum sample diameter able to be scanned is 60 mm and with detector shift up to 120 mm. The resolution depends on the sample size and can be as low as 1 μm for a sample size of 1 mm³. *Table 2.2* shows the settings of the CT scanner for the experiments of this project.

Experiment	Setting Specifications	Details
1	160 kV, 230 μA, Resolution 22.5 μm	
2	160 kV, 180 μA, Resolution 25 μm	• 500 ms between images
3	150 kV, 180 μA, Resolution 25 μm	• Take average of 5 images and skip 1
4	140 kV, 100 μA, Resolution 25 μm	image at each rotation of 0.5°
5	140 kV, 110 μA, Resolution 25 μm	• 1440 images in total
6	140 kV, 110 μA, Resolution 25 μm	
8 / 9	140 kV, 110 μA, Resolution 25 μm	

Table 2.2: Micro CT Scanner settings of each rock sample

After scanning the sample, the retrieved images have to be reconstructed. An image correction called "beam hardening correction" of 9 is applied to achieve a homogeneous greyscale throughout the dataset. An X-ray signal is getting weaker the deeper a material is penetrated. Since the rock sample is rotating by 0.5° between each individual scan, the signal in the middle of the core is weaker than at the edges. This is why a beam hardening correction needs to be applied to equalize the signal strength across the entire sample. The resolution is then reduced to half in order to get smaller files to work with (e.g. from 25 μm to 50 μm).

Examples of cross-sectional image slices of Experiments 1 – 4 can be seen in *Figure 2.8*.
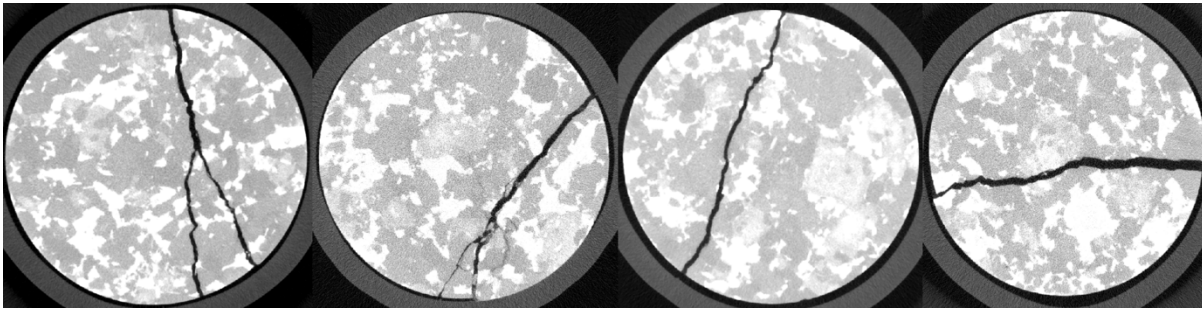
Fig. 2.8: Micro CT scans of fractured rock samples of Experiment 1, 2, 3, 4 (from left to right). Cross-sectional slices in approximately half of the length of the cylinder/middle of the sample

2.8 3D Fracture Analysis with AVIZO

The 3D image sequence generated by computed tomography tools is now analyzed with the software AVIZO®. In order to accurately detect the fracture volume within the sample, the irrelevant data space surrounding the cylindrically shaped rock sample has to be excluded. This is done by the tool "Volume Edit" in AVIZO. By cropping out further "dead data space" in all 3 axis directions with the AVIZO cropping tool, the data space is now reduced to the solid rock mass containing the fracture. The fracture now has to be isolated from the rest of the rock by using the AVIZO tool "Interactive Thresholding" to create a binary image. The intensity range of the tool "Interactive Thresholding" has to be set in such a way that it only covers the color contrast of the fracture volume. Intensity ranges applied for the different samples are indicated in *Table 2.3*.

Experiment	1	2	3	4	5	6	8 / 9
Intensity Range	2000 – 6100	2000 – 7216	2000 – 7810	2000 – 6514	2000 – 5450	2000 – 6508	2000- 4981

Table 2.3: Intensity ranges used in AVIZO

There was an individual intensity range chosen for each sample due to different fracture geometries. A relatively simple fracture without branching off such as is the case in Experiment 3, a high intensity range could be chosen without the risk of too much noise. However, a relatively complicated branched-off fracture that occurred in Experiment 5, a low intensity range had to be chosen to exclude noisy micro-fractures not relevant for fluid flow in this project.

Since the intensity range chosen to detect the fracture also includes noise and parts of the rock that do not belong to the fracture, this has to be removed by the AVIZO tool "Remove Small Spots". Setting this tool to remove all spots with 10000 or less pixels connected, the majority of the noise can be erased. These small spots could be existing micro-fractures in the rock that are not connected to the generated fracture and are

therefore not relevant to fluid flow. To remove remaining undesired spots, a manual drawing tool in "Volume Edit" is used to encircle areas to be erased. The generation of a surface then allows for better visualization and compatibility with other software. Fracture surface analysis within this project is however limited to the work done in AVIZO. The tool "Label Analysis" can be used on either the fracture volume or surface to compute parameters such as total volume or surface area. Each generated fracture from Experiments 1 – 6 and the drilled hole of Experiments 8 – 9 was analyzed in AVIZO and presented in the results section of this thesis.

2.9 Numerical Simulations with COMSOL Multiphysics

2.9.1 General Setup

The software COMSOL Multiphysics Version 5.3a was used to simulate heat transfer problems occurring in the conducted experiments. COMSOL is mainly used as a tool to understand what heat transfer behavior is happening inside and around the sample and yield comparable results to the experiments. Temperature gradients can be observed across the entire experimental setup at no-flow conditions as well as during the times when a steady-state fluid flow is imposed on the sample. Integrated numerical models in COMSOL compute temperature values at desired locations of the sample setup. An axisymmetric heat exchange behavior is assumed around the axial cylinder axis of the sample and the pressure cell. Therefore, a 2D model initially presents a sufficient temperature distribution model for this case. Initially, only the rock sample with a fluid pathway in the middle, the insulating rubber jacket and the metal disks on top and bottom were considered for the heat exchange model. A stationary heat transfer problem in solids at steady-state constant flow rate conditions was computed. As depicted in *Figure 2.2* thermocouples are placed in three locations around the sample. This presents a relatively scarce distribution of temperature measurement locations and therefore requires assumptions to be made for various input parameters in COMSOL. The following assumptions were made for modeling in COMSOL:

- The fracture is box shaped according to the parallel plate theory without variations in aperture during one simulation run.
- The behavior of heat transfer is axisymmetric and modelled in the 2D ZR-plane (axial-radial direction) perpendicular to the fracture plane.
- The temperature at the outermost layer of the rubber jacket is divided into 8 temperature sections in axial direction with increasing temperature from the bottom to the top. Constant temperatures at these locations are based on measurements of thermocouples during experiments.

- Constant temperatures are assigned to the bottom and top boundaries of the model based on measurements of thermocouples for the first simulation, while open boundaries are applied for all subsequent simulations.

- Thermal properties of the materials used in the model are based on the material data set of COMSOL Multiphysics (distilled water), on experimental findings of the density determination kit and thermal conductivity analyzer and calculations (rock samples, rubber jacket, steel wedges) as shown in *Chapter 2.1* and on literature values and fitting curves (pressurized oil) elaborated in *Chapter 2.9.4*. See *Table 2.4* in *Chapter 2.9.4* for a complete list.

- Model dimensions are based on approximate measurements of assembly parts used during the experiments. The entire sample model setup is 80 mm high which includes steel metal disks at the bottom and the top of the rock sample with 15 mm height each and a sample height of 50 mm. The width of the model is totaling 34.4 mm including the rock sample width of 30 mm and rubber jacket thickness of 2.2 mm on each side.

Figure 2.9 shows the model geometry used in COMSOL Multiphysics with different predominant physics in different areas of the model. The heat transfer module was used for the entire model where laws for heat transfer in solids are applied for the areas consisting steel, rubber or granite. For the fluid pathway along the middle of the sample, heat transfer in fluid physics and laminar flow are predominant. In order to couple heat transfer processes with laminar flow, the Multiphysics module Nonisothermal Flow needs to be added.
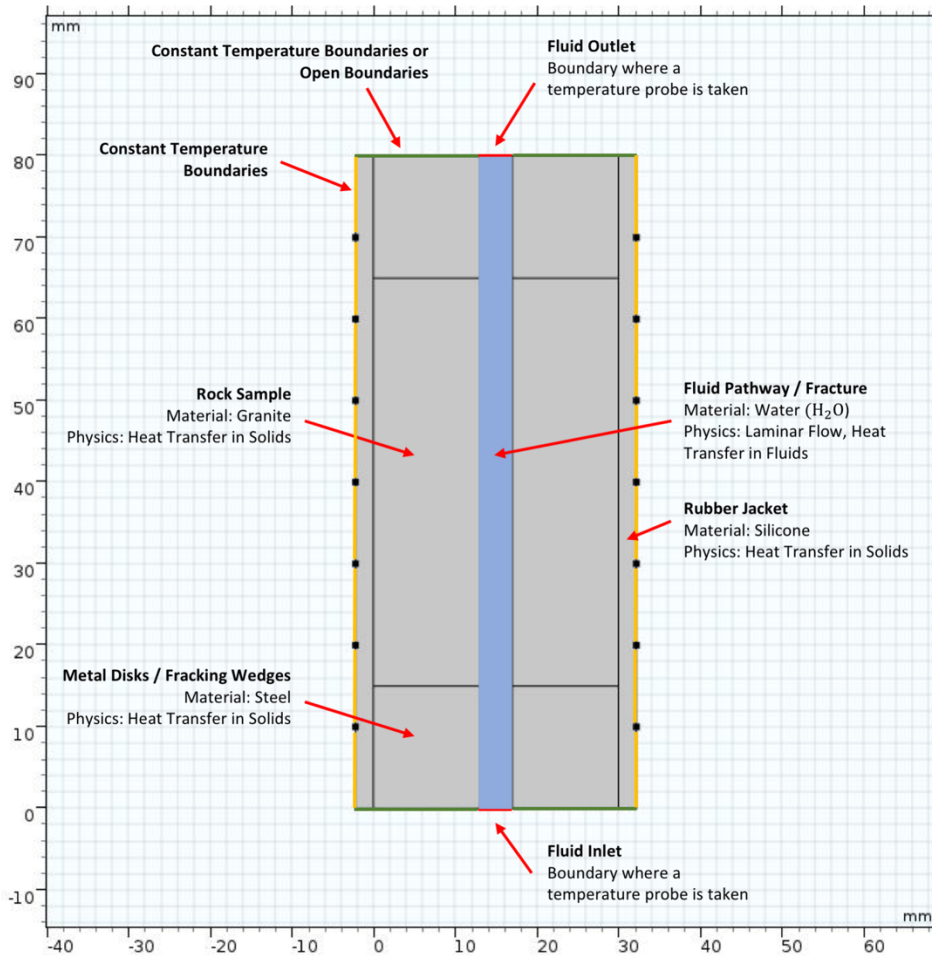
Fig 2.9: Sample geometry of the 2D model created with COMSOL Multiphysics describing the different parts in terms of materials and physical laws ruling. Dimensions are shown in mm along the z (axial) and r (radial) axis. The fluid pathway depicted in the middle represents the case of one of the benchmarking experiments, a hole of 4 mm drilled through the middle of the sample in axial direction. Artificially generated fractures present a much narrower fluid pathway.

Similar to the laboratory experiments carried out, a laminar fluid flow from the bottom to the top of the sample assembly is imposed on the COMSOL model. A constant average fluid velocity is defined at the inlet and a zero-pressure or 10 bar back-pressure condition is applied at the outlet. This allows for a rather constant fluid velocity along the entire flow pathway. Similar flow rates as used during the experiments are used for the model. Temperature conditions measured during the experiments are used to set temperature boundary conditions and inlet fluid temperature in the COMSOL model. The goal of the numerical work in COMSOL is not primarily to simulate the same temperature conditions as in the experiments. More so it is attempted to yield similar heat exchange responses comparable to the experiments by changing certain parameters of the model, mainly flow rates and the width of the fluid pathway/fracture as well as the geometry of the fluid pathway.

2.9.2 Model with Constant Temperature Boundaries (2D)

In a 2D model taking the cross-section along the middle of the sample, the differences between benchmarking and fracture experiments in terms of fluid pathway geometry cannot be considered. This is due to rectangular ducts and pipes (fracture versus cylindrical fluid pathway) looking the same from a cross-sectional perspective. However, in the first set of simulations benchmarking experiments were reproduced by applying the same fluid pathway width of 4 mm. The boundary conditions of the model are set at constant temperatures for this simulation. The lowest temperatures are applied at the bottom (68 °C) while the highest temperatures (95 °C) are applied at the top. These temperatures are similar to temperatures measured during Experiment 8 based on inlet and outlet temperatures. Since the sample temperature at the outside of the rubber jacket is fairly constant throughout the experiment, it is a good assumption to set constant temperature boundaries. Injection temperature is set to 52.1 °C based on measurements during Experiment 8. For simulation results to be more comparable, the temperature conditions were kept constant for all 2D simulations conducted in this thesis. It does not necessarily match with experimental temperatures. However, as mentioned before, the goal is not to receive the same temperatures as in the experiments, but more so to see similar trends as certain parameters are altered. Another simulation run was conducted at constant temperature boundaries with the fluid pathway width altered to 1 mm.

2.9.3 Model with Constant Temperature Boundaries and Open Boundaries (2D)

For this set of simulations, open boundary conditions were applied at the top and bottom of the model (see *Figure 2.9*). This allows for unrestricted heat flow along these boundaries. All other boundary conditions are unchanged. It is expected that more realistic conditions are simulated by applying these changes. Due to the geometry of the furnace, it is most likely that the majority of the heat flux towards the sample occurs at its side boundaries.

Within this set of simulations, **three different cases** were simulated.

a) Starting with varying flow rates at a constant aperture, it is investigated what impact flow rates have on heat exchange. This case is simulated at three different fracture apertures of 0.1 mm, 0.2 mm and 1 mm. Flow rates are varied from 2 ml/min up to 80 ml/min, but temperature distribution figures only show the range between 2 ml/min and 10 ml/min while temperature difference curves cover the range between 2 ml/min and 20 ml/min. The reason for showing only limited flow rate ranges is because the relevant changes occur within this range.

b) In the second case, the impact of varying fracture aperture at a constant flow rate and constant fluid velocity is investigated. Firstly, the flow rate is kept at 6 ml/min while varying the fracture aperture in the range of 0.1 mm to 2 mm. Secondly, the fluid velocity is kept at 0.033 m/s while varying the fracture aperture within the same range.

c) In the third case, fracture geometries are altered by adding additional side fractures of similar apertures. 1 and 2 side fractures are added while the simulation with 2 side fractures is also altered to a winding fracture network. The same variation of flow rates as in the first case is applied on each geometry.

2.9.4 Axisymmetric extended model

In addition to the simplified model of *Chapter 2.9.1*, a more extensive model including the oil surrounding the sample assembly and the heating furnace was integrated into COMSOL. Since the oil convection within the pressurized vessel is likely a major driving force for the heat transfer and also causes a vertical temperature gradient to establish along the sample assembly, it is important to look into these processes. An axisymmetric geometry is chosen in COMSOL assuming radially symmetric conditions. Since a radial symmetry is only achieved in experiments with a drilled hole serving as the fluid pathway, Experiment 8 is simulated in this section. Unlike the COMSOL model with the geometry explained in *Chapter 2.9.1*, the goal of this simulation is to investigate in the heat transfer processes as a whole and the transition between convective and conductive heat exchange instead of yielding absolute temperature values at the fluid inlet and outlet.

The pressurized oil filling the void space between furnace and pressure cylinder as well as between sample assembly and furnace is of the type MultiTherm PG-1$^{®}$, a non-toxic heat transfer fluid (Multitherm LLC., 2018). To establish temperature dependent density driven fluid convection of the oil, the density as a function of temperature needs to be implemented into COMSOL. Density values were taken from Multitherm LLC. and plotted against temperature. The resulting linear curve and the corresponding equation is depicted in *Figure 2.10*.
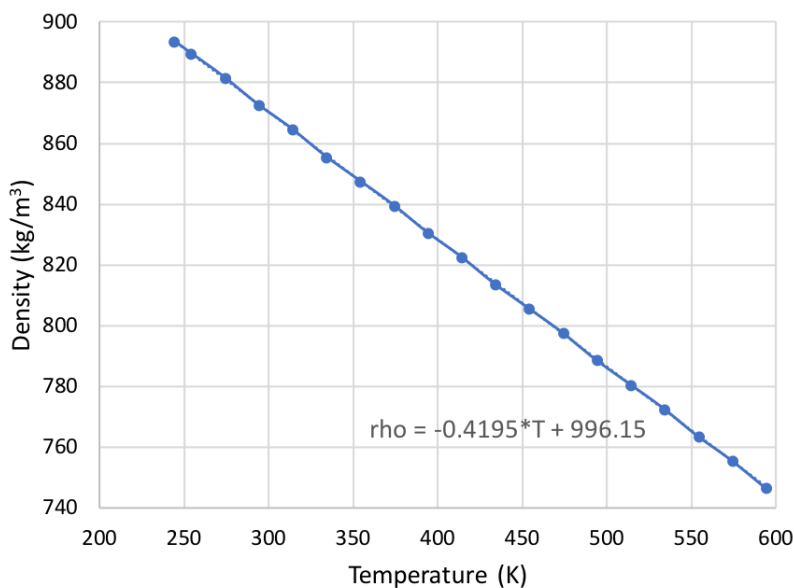
Fig 2.10: Density of MultiTherm PG-1® as a function of temperature and the corresponding linear equation.

Since the viscosity of MultiTherm PG-1® varies significantly with temperature, a correlation equation was also established. *Figure 2.11* shows the viscosity function. However, due to a non-linear behavior of the curve, it is difficult to find a perfect fit. The equation is fairly accurate for temperatures above 273.15 K (0 °C). This is sufficient since all temperatures in present experiments and simulations do not reach values lower than 20-25 °C.
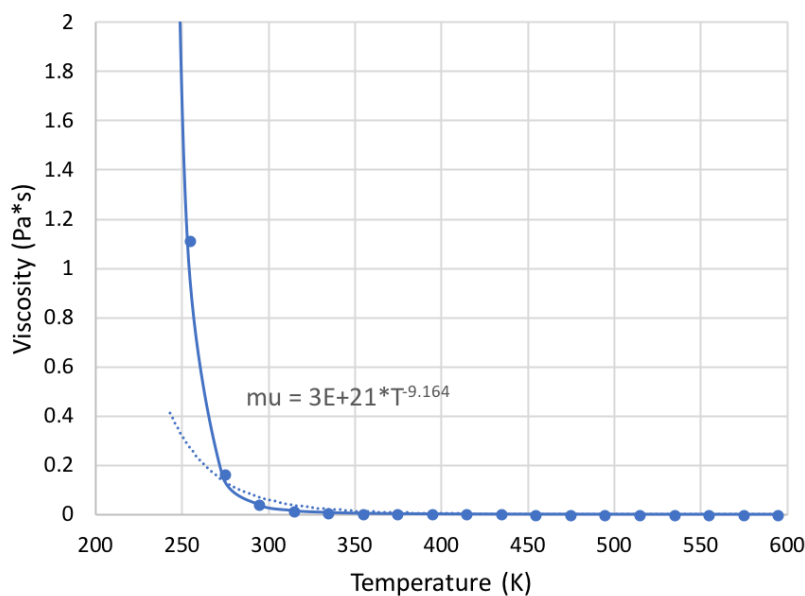
Fig 2.11: Viscosity of MultiTherm PG-1® as a function of temperature and the corresponding non-linear equation.

Other relevant parameters for the simulations are thermal conductivity and heat capacity of the oil. For simplification reasons and to reduce computation times, these parameters are set constant over the entire

Methodology

temperature range. These two heat transfer properties do not vary significantly with temperatures and an average value of **0.127 W/m/K** and **2100 J/kg/K** respectively are used.

The geometry of the COMSOL model is shown in *Figure 2.12* including the different heat transfer domains. The height of the cylindrical model is 28 cm with a diameter of 11 cm.
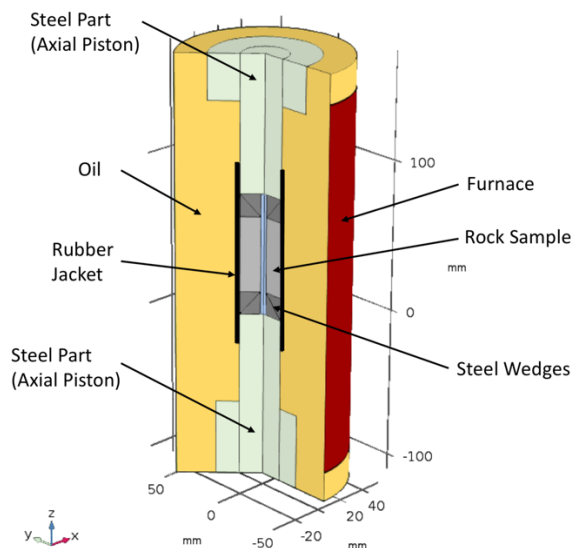
Fig 2.12: Geometry of the 2D axisymmetric COMSOL model with materials annotated.

A constant temperature of 100 °C is set at the furnace boundary while open boundaries are assigned at the top and the bottom of the model. A heat transfer physics module is used for the entire model while a laminar flow module is assigned for the oil and the fluid pathway domain. A gravity component is added in the laminar flow module to account for density variations of the oil with temperature. For properties of other materials steel (wedges and pistons), rubber (rubber jacket), granite (rock sample) and demineralized water (fluid pathway) the same values are used as in previous simulations. Other assumptions are identical to the setup explained in *Chapter 2.9.1*.

The axisymmetric model includes **three different cases** that were simulated in COMSOL including time-dependent no-flow conditions **(a)**, stationary steady-state flow conditions **(b)** and time-dependent flow conditions **(c)**.

a) In order to see the temperature distribution at different times, a time-dependent problem is now solved over a period of 180 seconds (initial heating) and 120 minutes (heating until thermal equilibrium). Additionally, the solution after 120 minutes at a thermal equilibrium with heat sinks at the top and bottom is also shown. No-flow conditions along the fluid pathway are applied.

b) Two sets of simulations with fluid pathway diameters of 4 mm and 1 mm respectively are computed at varying flow rates ranging from 2 ml/min to 10 ml/min. The solutions shown are at a thermal equilibrium (stationary solution). While the furnace is kept at a constant temperature, a laminar flow along the fluid pathway in the sample is set at a constant flow rate injecting water at 52.1 °C. Initial temperature conditions of the entire model are set to 25 °C.

c) Experimental-similar sub-experiments are numerically simulated as well. So far in the axisymmetric model, time dependence was only implemented at no-flow conditions to see the heating pattern of the apparatus. Temperature distributions at flow conditions were only analyzed at a stationary solution, i.e., where a thermal equilibrium is achieved. It is desirable to also investigate in the exponential cooling itself that occurs during every sub-experiment and is elaborated in *Chapter 2.6.4*. For this, the simulated apparatus was first heated up for 100 minutes setting the furnace boundary temperature to 100 °C. After 100 min, a constant volumetric flow rate is imposed on the sample (6 ml/min in this case). Temperatures along the length of the fracture as well as temperature distributions in the apparatus are documented until a steady-state flow condition and thermal equilibrium is achieved.

In order to summarize all material properties relevant for the COMSOL simulations, *Table 2.4* is provided.

	Thermal Conductivity (W/m/K)	Heat Capacity (J/kg/K)	Density (kg/m^3)	Viscosity (Pa.s)
Rock Sample	2.918 [1]	745.71 [2]	2745.6 [3]	-
Water (H$_2$O)	(0.606) [4]	(4182.6) [4]	(996.9) [4]	(8.872 E-4) [4]
Steel Wedges	25.84 [1]	457.67 [2]	7823.7 [3]	-
Rubber Jacket	0.619 [1]	1250.4 [2]	1250.3 [3]	-
MultiTherm Oil	0.127 [5]	2100 [5]	(871.1) [6]	(6.33 E-2) [6]

Table 2.4: Relevant material properties used in COMSOL simulations. Meaning of superscripts see below.

1) *Measured with a C-Therm Thermal Conductivity Analyzer$^{®}$ described in Chapter 2.1.*
2) *Derived with Equation 2 described in Chapter 2.1.*
3) *Measured with a density determination kit described in Chapter 2.1.*
4) *Temperature-dependent function in the material library of COMSOL. Shown values at 25 °C.*
5) *From literature (Multitherm LLC., 2018) described earlier in this chapter.*
6) *From literature (Multitherm LLC., 2018), temperature-dependent function approximated with fitting curve described earlier in this chapter. Shown values at 25 °C.*

3. Results

3.1 Triaxial testing

As mentioned in the *Methodology* section, a total of eight experiments on the triaxial apparatus were carried out. Temperature measurement results of all experiments are presented starting with Experiments 1 – 6 in *Chapter 3.1.1* as a function of flow rate and Experiments 2 and 6 in *Chapter 3.1.2* as a function of fracture aperture. Then, temperature data of the benchmarking Experiments 8 – 9 are presented in *Chapter 3.1.3* as a function of flow rate*. The following parameters relevant in answering the research questions are plotted. Most relevant are temperatures expressed in absolute values and differences (°C) as well as in relative percentile changes (%). Additionally, fluid velocity, pressure difference, permeability and Reynolds Number are plotted (only as a function of fracture aperture). Exponential fitting curves of the cooling and steady-state condition analysis of all sub-experiments are presented in *Chapter 3.1.4*.

All triaxial testing experiments conducted in this project show similar temperature patterns as depicted in *Figure 3.1.* Based on the temperature behavior observed at the three thermocouples, experiments are divided into different experimental stages. Stage A represents the heating of the apparatus to the point where thermal equilibrium is reached. Stage B represents the thermal equilibrium where temperatures are not changing significantly anymore. Stage C represents a sub-experiment where exponential cooling occurs due to an imposed fluid flow. Depending on the goal of each individual experiment, stage C is repeated several times. Between every stage C, the apparatus heats back up to reach thermal equilibrium which represents a combination of stage A and B. In stage D, the heating furnace is turned off and the apparatus cools back down to room temperature. Temperature values that make up most subsequent results of *Chapter 3.1.1 – 3.1.3* are taken at two points: A point at the end of stage B is selected to read temperature values at no-flow conditions in thermal equilibrium (green vertical line in *Figure 3.1*); then, a point at the end of stage C is selected to read temperature values at flow conditions with steady-state temperatures (blue vertical line in *Figure 3.1*). The reason why only one point instead of a range is selected to read values is the small data variation that occurs in equilibrium and steady-state conditions. This generally small variation from mean values is elaborated in the second part of *Chapter 3.1.4*.
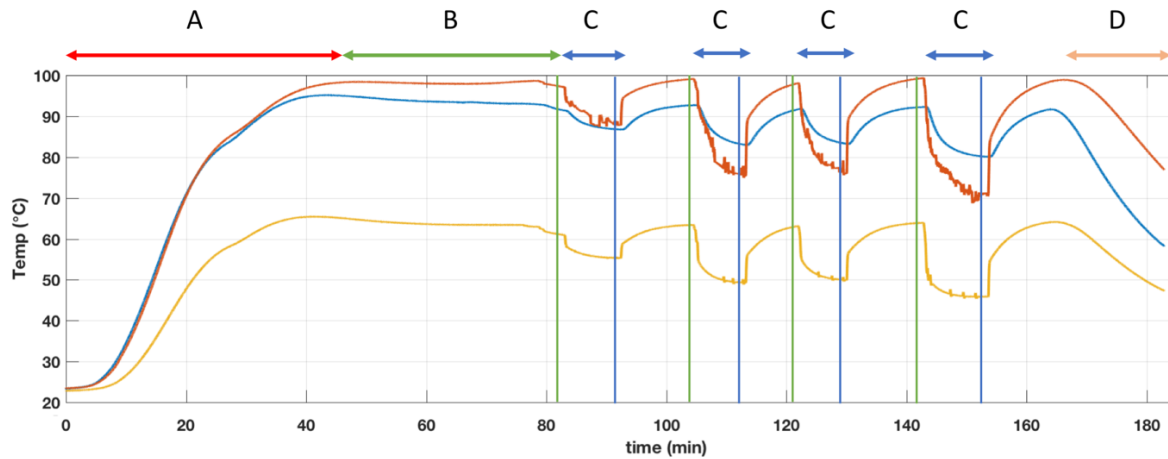
Fig 3.1: Temperature values at the inlet (yellow curve), outlet (red curve) and sample (blue curve) throughout the course of a typical experiment on the triaxial apparatus (Experiment 1). The x-axis shows a time range of approximately 180 min. Different stages of an experiment are annotated on top with the letters A-D. The green and blue vertical lines indicate the approximate time points where temperature values at no-flow and flow conditions are read respectively.

3.1.1 Experiments 1-6 – as a function of flow rate

Figure 3.2 gives an overview of the initial temperatures measured at the points as shown in *Figure 3.1.* Based on these absolute temperature values, most following figures of this chapter are generated to allow clearer insight for interpretation and comparison purposes. The values plotted in *Figure 3.2* are listed in *Table 8.1* in the appendix.

Apart from Experiment 2, where temperatures at no-flow as well as steady-state flow conditions are notably higher at all thermocouple locations, similar temperature conditions could be applied for each subsequent experiment. The goal was to repeat the same initial temperature conditions (no-flow temperatures) prior to each sub-experiment within the same experiment as well as across different experiments. This was successfully done since the initial temperature range is fairly small, again with the exception of Experiment 2.
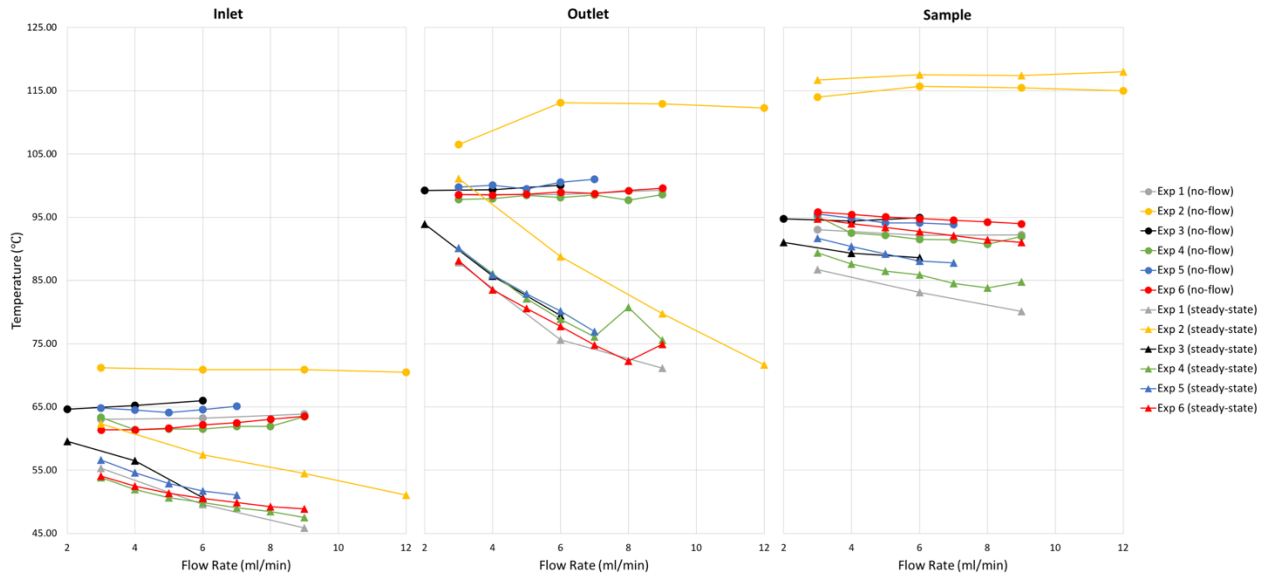
Fig 3.2: Absolute temperatures at the inlet, outlet and sample location measured during Experiments 1 to 6. Each of the 3 subplots consists of a set of graphs of temperatures at no-flow conditions and a set of graphs at steady-state flow conditions for each experiment. Plotted values are listed in Table 8.1 (Appendix).

An indicator of how much heat is absorbed by the fluid flowing through the sample is comparing the outlet temperature at no-flow conditions with the outlet temperature at steady-state flow conditions (green and blue vertical line respectively in *Figure 3.1*). A larger value of this temperature difference (ΔT_{out}) suggests less heat taken up by the fluid per volume unit. Due to variations in the heating behavior of the furnace, not all sub-experiments could be carried out at identical initial temperature conditions. The average outlet temperature at no-flow conditions over all sub-experiments is 101 °C. To compare ΔT_{out} values of each experiment, changes are expressed in percentage. In other words, to what percentage fraction does the temperature decrease from no-flow to steady-state flow condition. This is calculated with the following term:

$$\Delta T_{out}(\%) = -\left(100 - \left(T_{out_{flow}} * \frac{100}{T_{out_{no-flow}}}\right)\right) \qquad (Eq.\ 16)$$

In *Figure 3.3* results of ΔT_{out} and a fitting curve of all fracture experiments are shown. The drop of temperatures at the outlet (ΔT_{out}) is generally increasing with higher flow rates while differences between experiments are small.
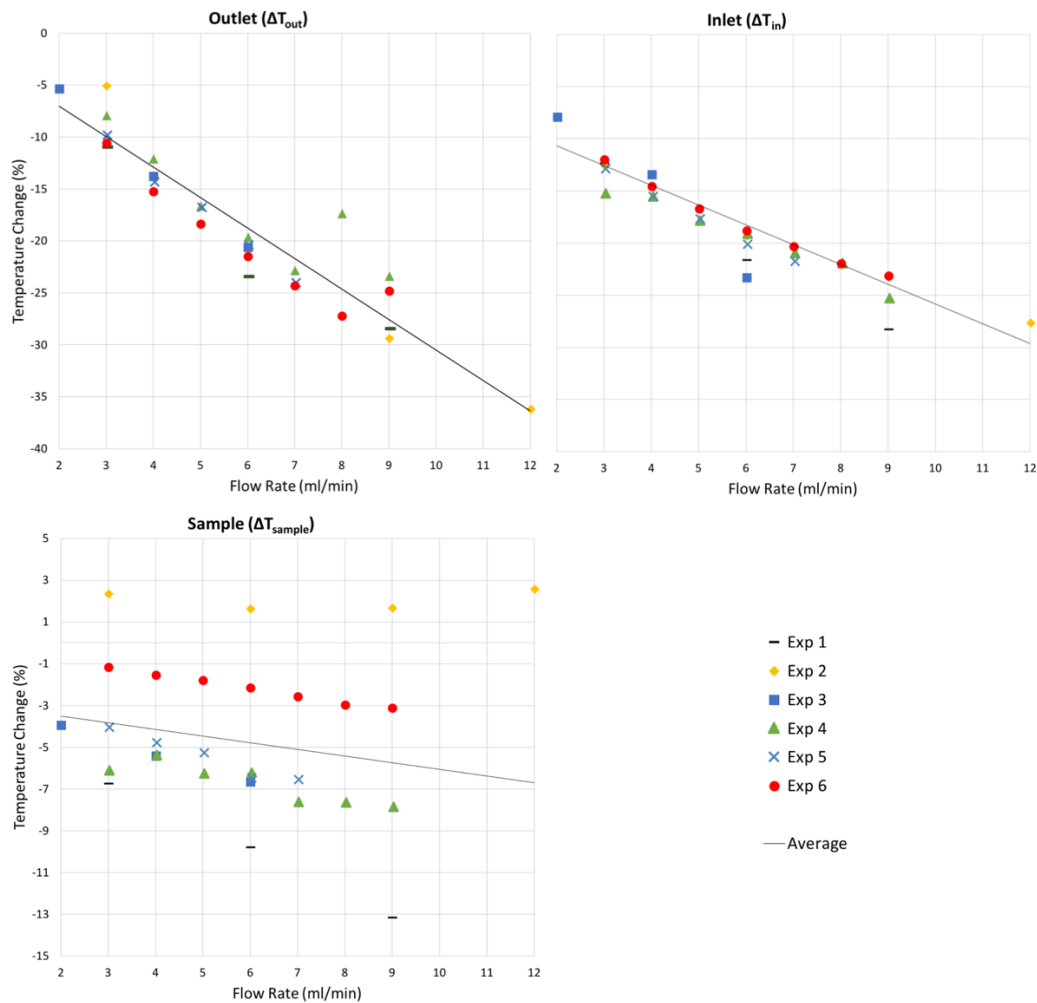
Fig 3.3: Relative comparison of temperature changes at different flow rates at the outlet, inlet and sample thermocouple. Note that not all samples were tested in the flow rate range between 2 to 12 ml/min. The black curves depict a linear trendline of the average for Experiment 1 to 6. Note that the range of temperature change (%) is different for ΔT_{sample}.

The same temperature difference in percentage can be quantified for the inlet as well as the sample temperature which is measured outside of the rubber jacket. Due to the temperature gradient along the rock sample in axial direction that is present at no-flow conditions as well as steady-state flow conditions, temperatures at the inlet are notably lower than at the outlet. Therefore, the temperature changes at the inlet (ΔT_{in}) are generally smaller than at the outlet. The average inlet temperature at no-flow conditions over all sub-experiments is 65 °C, that is 36 °C colder than at the outlet. ΔT_{in} of all fracture experiments is also depicted in *Figure 3.3* along with the sample temperature change ΔT_{sample}. Generally, the temperature measured at the outside of the rock sample encounters much smaller changes compared to the fluid temperatures at the inlet and outlet. This depends greatly on where the sample thermocouple tip is placed with respect to the fracture. This is discussed in greater detail in *Chapter 4.1.1.* The average sample temperature at no-flow conditions over all sub-experiments is 97 °C, which is only 4 °C colder than outlet temperatures at no-flow conditions.

Results

In order to understand the heat exchange behavior between the rock and the fluid in these experiments better, it is also useful to look at the absolute temperature difference between the outmost layer of the sample (T_{sample}) and the temperature at the outlet (T_{out}) at various flow rates. This can provide insight into an approximate temperature gradient across the sample in radial direction. In the majority of cases, the sample temperature is higher than the outlet fluid temperature at steady-state flow conditions. As depicted in *Figure 3.4*, variations in the temperature difference with altering flow rates as well as between different experiments can be observed. Experiment 2 shows the highest temperature gradients followed by Experiment 6. The rest of the fractured sample experiments have similar behavior in temperature differences.
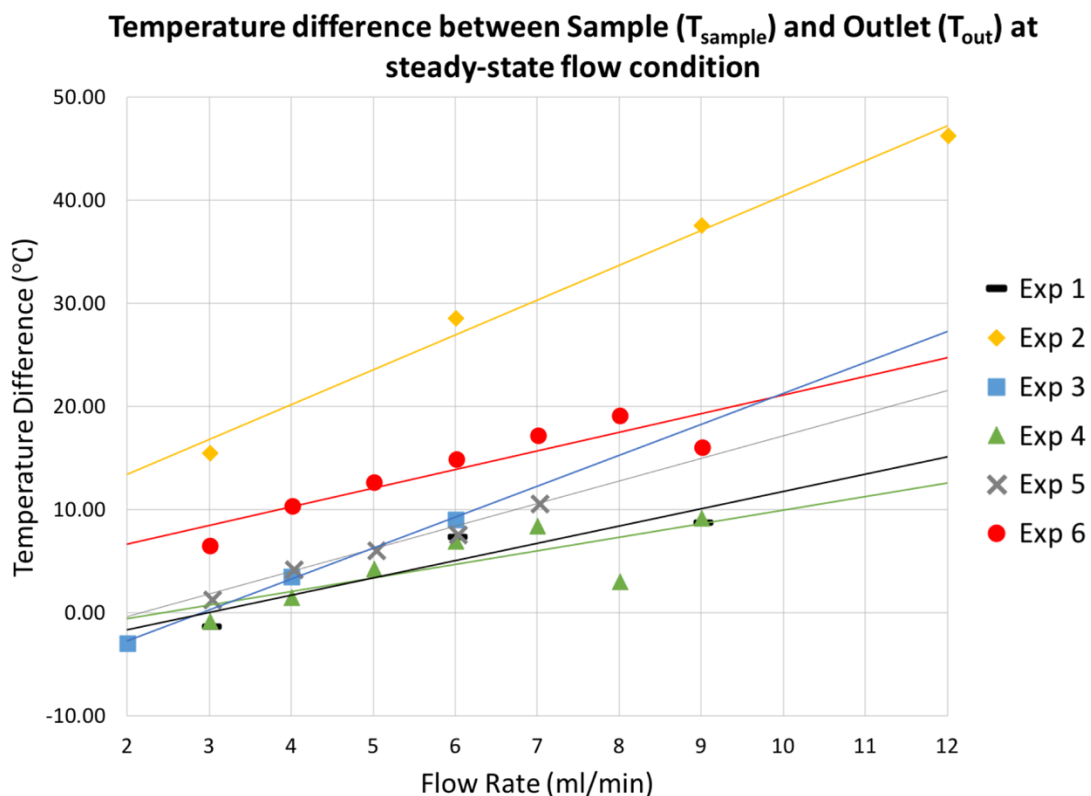
Fig 3.4: Temperature differences between sample and outlet ($T_{sample} - T_{out}$) measurement locations at steady-state flow condition. Fractured sample Experiments 1 – 6 are shown. Linear trendlines for each experiment are displayed.

Additionally, absolute temperature differences between no-flow and steady-state flow conditions of fractured sample Experiments 1 – 6 are presented. Temperature differences in °C at the inlet, outlet and sample measurement locations are depicted in *Figure 3.5.*

As expected, the linear trend lines averaging all six experiments of differences at each the inlet, outlet and sample show notable differences. High temperature drops are observed at the outlet increasing with higher flow rates, followed by the inlet while the sample experiences only slight changes in absolute temperatures.
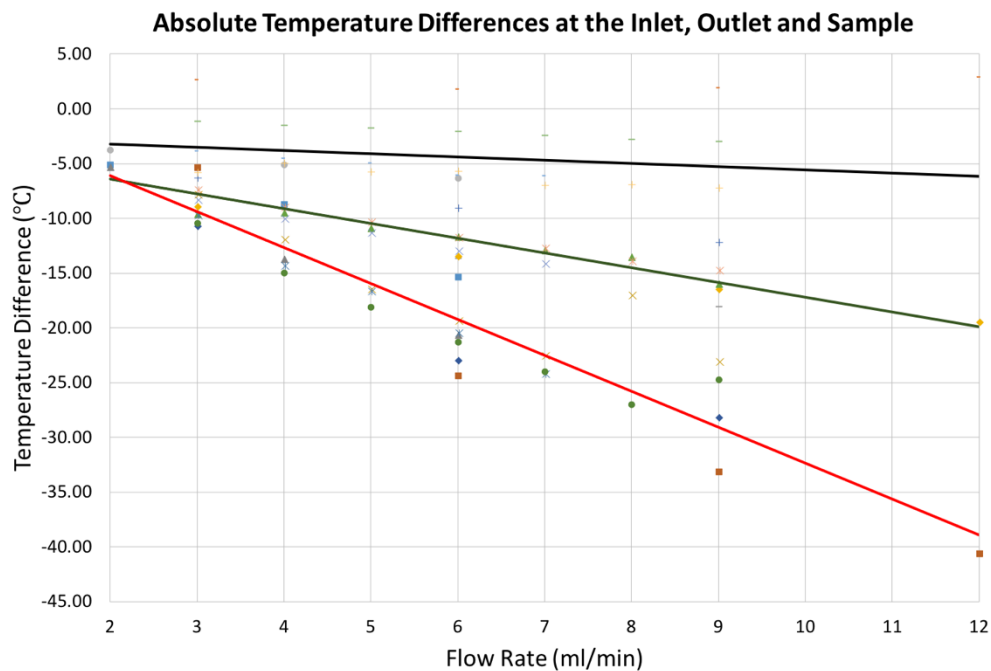
Fig 3.5: Absolute temperature differences comparing steady-state flow condition temperatures with no-flow condition temperatures ($T_{flow} - T_{no\text{-}flow}$). It is therefore a temperature drop/decrease. The red trend line depicts average ΔT at the outlet, green trend line for the inlet and black trend line for the sample.

As mentioned in *Chapter 2.5* there is already a large temperature gradient across the sample present even at no-flow conditions. Therefore, the absolute difference between inlet and outlet at steady-state flow conditions is not as important or representative as, e.g., the temperature drop at the outlet. For the sake of completeness and potential interpretation purposes in the discussion however, the discussed parameter is depicted in *Figure 3.6.* The difference becomes smaller with increasing flow rates while slight differences between the experiments can be observed.
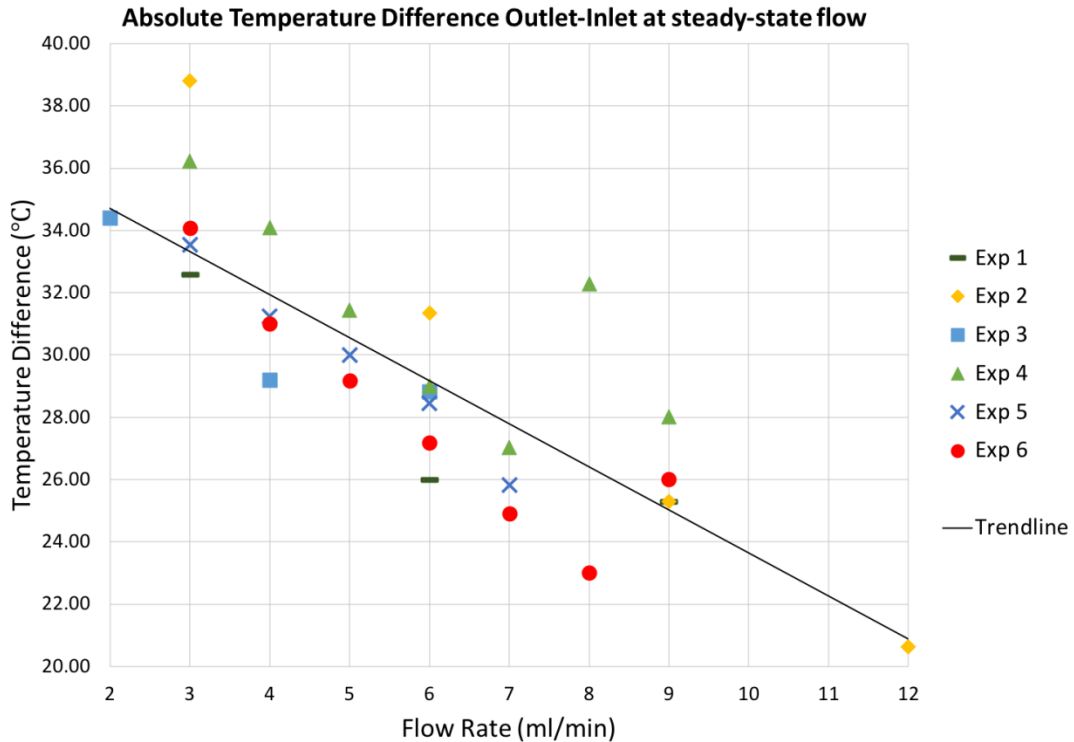
Fig 3.6: *Absolute temperature differences ($T_{out} - T_{in}$) at steady-state flow conditions of Experiments 1 – 6. The trend line depicts an average trend of all fractured sample experiments.*

3.1.2 Experiments 2 and 6 – as a function of fracture aperture

In addition to varying the flow rates, the fracture aperture was manually altered during Experiments 2 and 6. As described in *Chapter 2.4*, it is possible to increase the fracture aperture by forcing the steel wedges into the rock sample. For the set of sub-experiments that involve manual aperture variations, a constant flow rate of 6 ml/min was imposed on the rock sample. In Experiment 2, six sub-experiments were conducted where the fracture aperture instead of the flow rate is varied. In Experiment 6, five sub-experiments involved this procedure. Since the flow rate is constant while the aperture is altered, the average fluid velocity along the fracture changes as well. This is depicted alongside the temperature drops in percentage at the inlet and outlet in *Figure 3.7* (Experiment 2) and *Figure 3.8* (Experiment 6). While the fluid velocity decreases with increasing fracture aperture, the temperature decrease between no-flow and steady-state flow conditions at the inlet and outlet behave in a way that no clear trend can be seen. Trendlines suggest that no notable change occurs as the aperture is varied. Since the data points do not lie within high proximity of the trendlines, it is not very representative. The fluid velocity (u) along the fracture behaves in the following way depending proportionally on the flow rate (Q) and the fracture aperture (a_f): u ~ Q/a_f. If the fracture aperture approaches zero, the velocity approaches infinity.
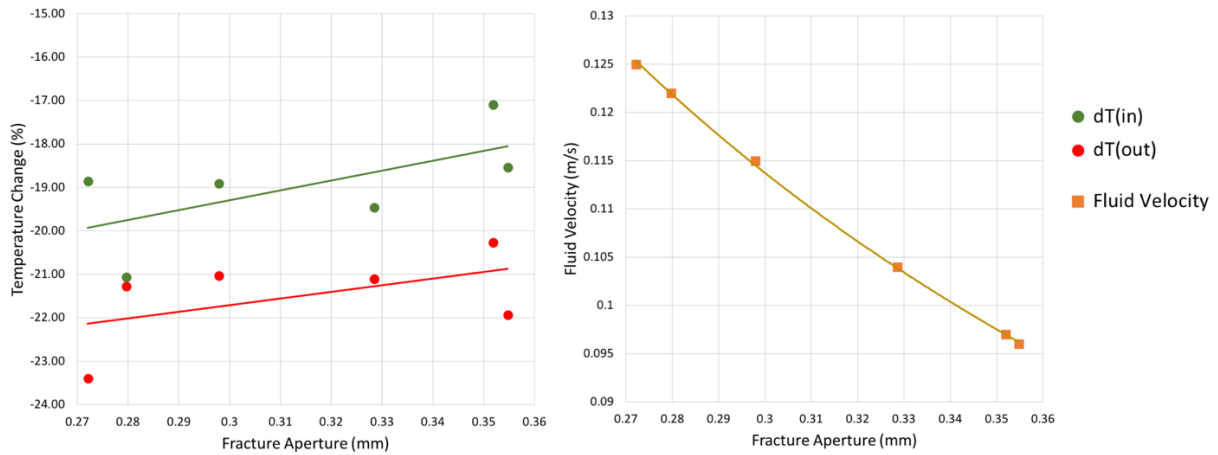
Fig 3.7: Results from Experiment 2. Inlet and Outlet temperature changes (left plot) and fluid velocity (right plot) along the fracture with varying fracture apertures. The colored lines in the left plot represent linear trendlines while the line in the right plot represents the proportionality relationship between velocity, flow rate and aperture. The flow rate is constant at 6 ml/min.
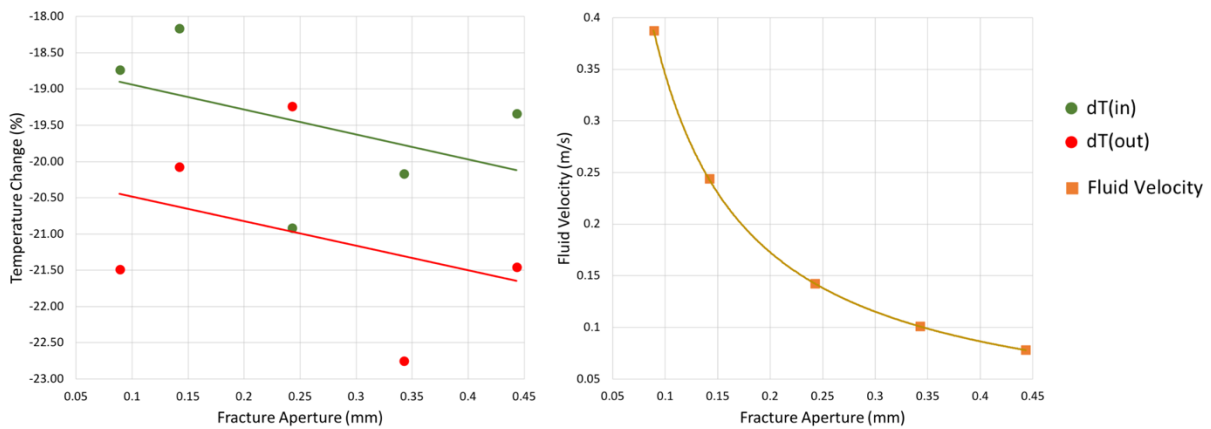
Fig 3.8: Results from Experiment 6. See description of Figure 3.7 above.

The permeability is expected to change upon altering the fracture aperture and therefore altering the size of the fluid pathway along the sample. As shown in *Chapter 2.6.1*, permeability based on the hydraulic fracture aperture *(Equation 7)* is most representative in this project. *Figure 3.9* depicts the trend in permeability with changing fracture apertures and constant flow rates. For reasons of comparison, the fluid velocity and the Reynolds Number are also plotted. As described in *Chapter 2.6.3*, the Reynolds number is a quantification for the flow regime predominant in the fractured rock. The hydraulic fracture permeability increases with higher fracture apertures while the permeability of the sample in Experiment 6 is generally higher compared to the permeability in Experiment 2. The Reynolds number stays constant across a wide range of fracture apertures. Other than in *Figure 3.7* and *Figure 3.8*, the fluid velocity is now combined for both experiments and also shows a declining trend with increasing aperture. Similar behavior can be observed for the directly measured pressure difference between inlet and outlet that decreases with increasing fracture aperture.

Results
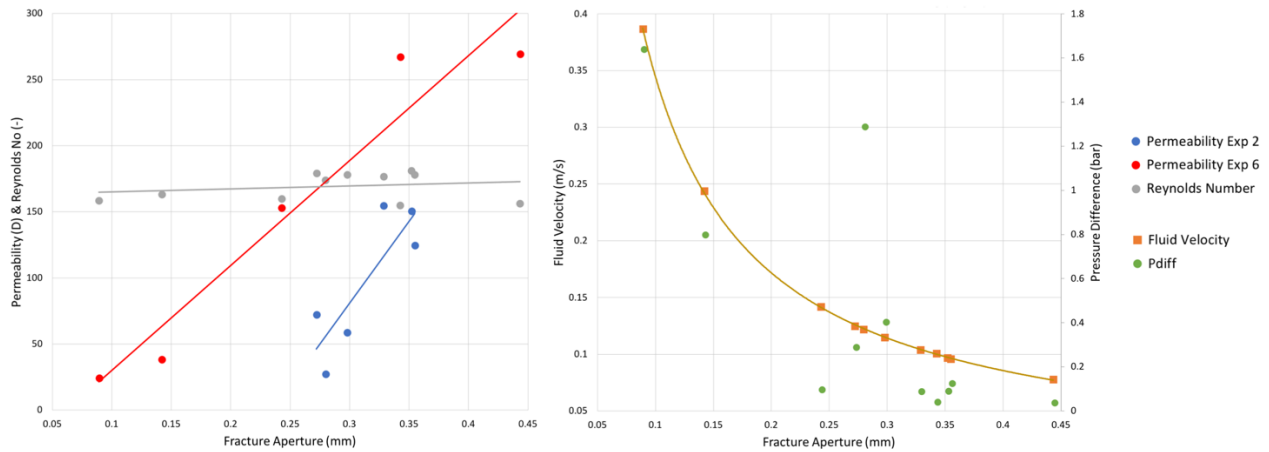
Fig 3.9: Permeability based on hydraulic fracture aperture and Reynolds Number as a function of fracture aperture at a constant flow rate of 6 ml/min (left plot). The blue and red linear trendlines depict the average trend for permeability of Experiment 2 and 6 respectively. The Reynolds Number in grey, the fluid velocity (right plot) in yellow and the pressure difference (right plot) in green are results of Experiments 2 and 6 combined.

3.1.3 Experiments 8 and 9 (benchmarking) – as a function of flow rate

For the two benchmarking Experiments 8 and 9, nine sub-experiments each were conducted with varying flow rates ranging from 2 ml/min to 10 ml/min.

Again, as shown in *Figure 3.2* for the fractured sample experiment, *Figure 3.10* depicts absolute temperature values of the benchmarking experiments at no-flow and steady-state flow conditions. The values plotted in *Figure 3.10* are listed in *Table 8.2* in the appendix. Initial temperatures could be held fairly constant prior to all sub-experiments throughout the experiments. Note that the target initial temperature for Experiment 8 was 100 °C (as for Experiments 1 – 6) while it was 60 °C for Experiment 9.
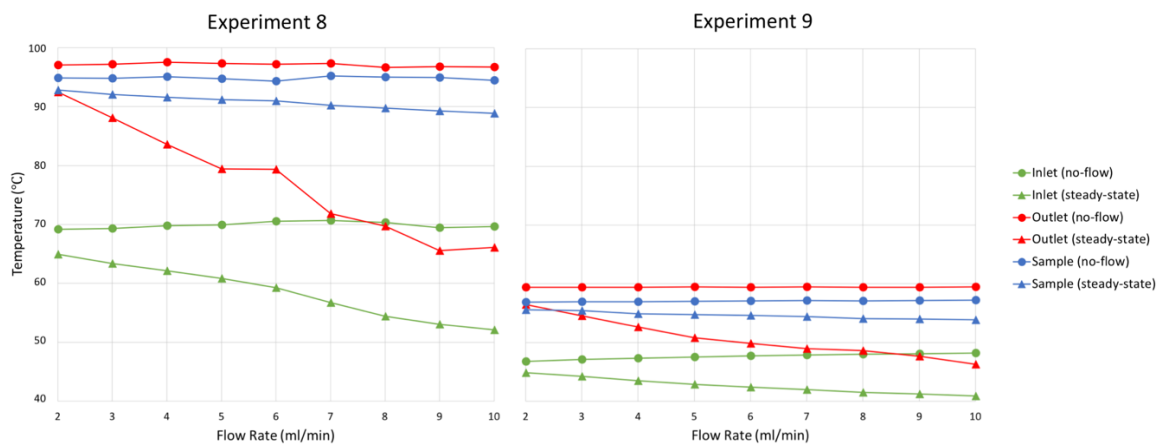
Fig 3.10: Absolute temperatures at the inlet, outlet and sample location measured during Experiment 8 and Experiment 9. Round markers show initial no-flow condition temperatures while triangular markers show temperatures at steady-state flow condition. Plotted values are listed in Table 8.2 (Appendix).

Comparable to *Chapter 3.1.1,* relative changes in temperatures expressed in percentage are depicted in *Figure 3.11* representing results of Experiment 8 and 9. The largest changes are again seen at the outlet with the highest initial temperatures at no-flow conditions as well. Temperature drops at the sample location only increase by a small amount with higher flow rates. Experiment 9 in general experiences less percentile changes compared to Experiment 8.
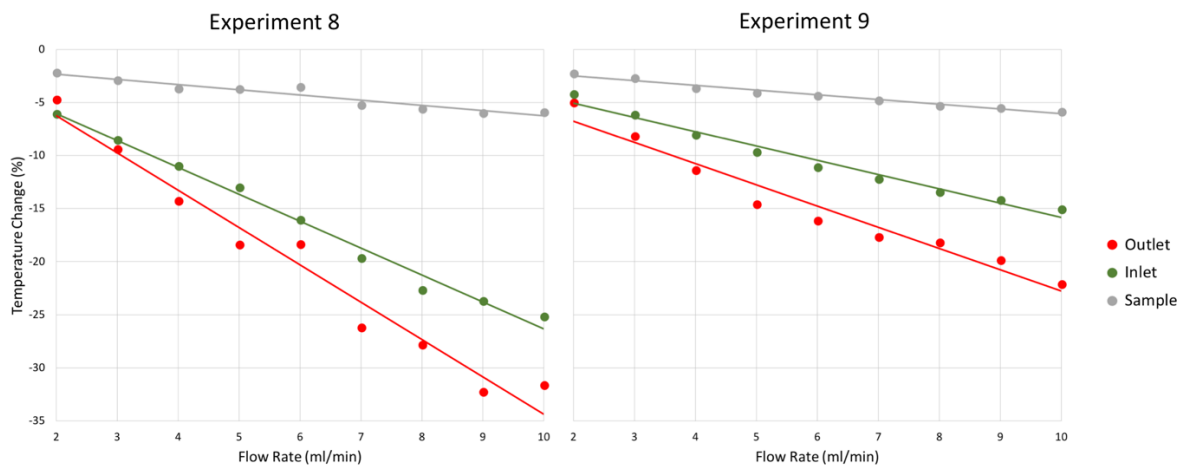
Fig 3.11: Results of Experiment 8 and 9. Relative changes of temperatures in percentage between no-flow and steady-state flow conditions. Flow rates 2 to 10 ml/min with steps of 1 ml/min were sequentially imposed. Linear curves represent trend lines.

Absolute temperature differences between the sample thermocouple location and the outlet at steady-state flow conditions are depicted in *Figure 3.12*. An increasing temperature gradient between the outer part of the sample and the outlet can be observed with higher flow rates.
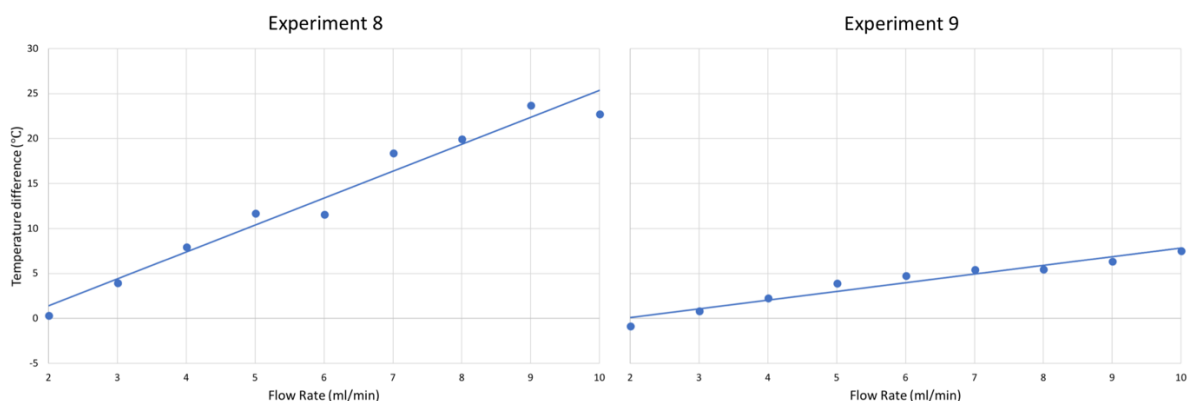
Fig 3.12: Results of Experiment 8 and 9. Absolute temperature differences between sample and outlet measurement locations at steady-state flow conditions ($T_{sample} - T_{out}$). The blue curves represent linear trendlines.

Results

Figure 3.13 shows temperature differences in absolute terms. Also plotted in the same figure is the temperature difference between outlet and inlet at steady-state flow conditions.
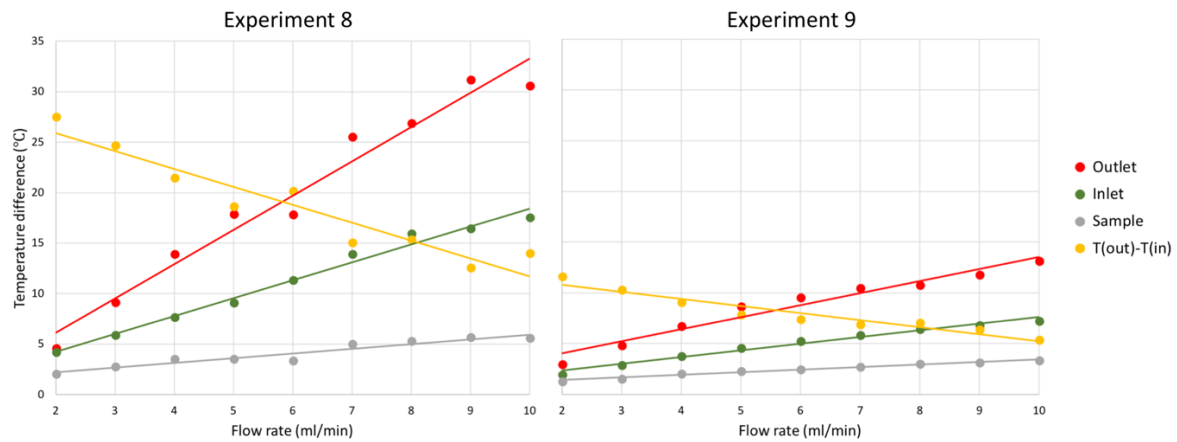
Fig 3.13: Results of Experiment 8 and 9. Absolute temperature differences at outlet, inlet and sample between no-flow and steady-state flow conditions. Temperature differences between outlet and inlet ($T_{out} - T_{in}$) at steady-state flow conditions are also plotted. Curves represent linear trendlines.

3.1.4 Exponential cooling and steady-state check

Exponential cooling curves of the temperature data from the inlet, outlet and sample thermocouple including their equations according to *Chapter 2.6.4* are shown in this section. All experiments are represented with the corresponding sub-experiment at a flow rate of 6 ml/min. The reason why this flow rate is chosen is that consistent data across all experiments exists. *Figures 3.14 – 3.17* depict the set of decay curves. According to *Equation 15* the formula for each exponential fitting curve consists of the variables a, b and c. a and c are temperature specific variables that define at what temperature the sub-experiment starts (a) and at what temperature it approaches a constant value (c). In order to interpret the cooling behavior itself, b is an important constant. That is why the exponential decay constant (λ or b) is compared between thermocouple locations. *Table 3.1* provides an overview of all λ-values taken from the functions shown in *Figures 3.14 – 3.17*. A decreasing trend of λ exists from inlet to outlet to sample. This trend is consistent throughout all experiments at a flow rate of 6 ml/min and is also visible in the average. Additionally, the exponential decay constants of all sub-experiments within Experiment 6 (flow rates 3 to 9 ml/min) and Experiment 8 (flow rates 2 to 10 ml/min) are listed in *Tables 3.2 and 3.3*.

Experiment	Inlet	Outlet	Sample
1	0.00815	0.00772	0.00703
2	0.0104	0.00698	0.000306
3	0.0254	0.00544	0.00398
4	0.00821	0.00626	0.00373
5	0.00795	0.00663	0.00545
6	0.00897	0.00649	0.0027
8	0.00708	0.00686	0.00344
9	0.00683	0.00525	0.00283
AVERAGE	**0.0104**	**0.0065**	**0.0037**

Table 3.1: Exponential decay constant λ or b at 6 ml/min at the inlet, outlet and sample location. In the bottom row, the average over all experiments is shown.

Flow Rate (ml/min)	Inlet	Outlet	Sample
3	0.0062	0.00797	0.00267
4	0.00681	0.00729	0.0024
5	0.00816	0.00821	0.00261
6	0.00897	0.00649	0.0027
7	0.00906	0.00782	0.00229
8	0.00927	0.00708	0.00193
9	0.00957	0.00568	0.0017
AVERAGE	**0.00829**	**0.00722**	**0.00233**

*Table 3.2: Exponential decay constant λ or b of **Experiment 6** at the inlet, outlet and sample location. In the bottom row, the average over all sub-experiments/flow rates is shown.*

Flow Rate (ml/min)	Inlet	Outlet	Sample
2	0.00571	0.0043	0.00387
3	0.00596	0.00626	0.00318
4	0.00713	0.00631	0.00347
5	0.00701	0.00393	0.00293
6	0.00708	0.00686	0.00344
7	0.00777	0.00586	0.00337
8	0.00788	0.00602	0.00282
9	0.00842	0.00623	0.00297
10	0.00881	0.00614	0.00344
AVERAGE	**0.00731**	**0.00577**	**0.00328**

*Table 3.3: Exponential decay constant λ or b of **Experiment 8** at the inlet, outlet and sample location. In the bottom row, the average over all sub-experiments/flow rates is shown.*

Results
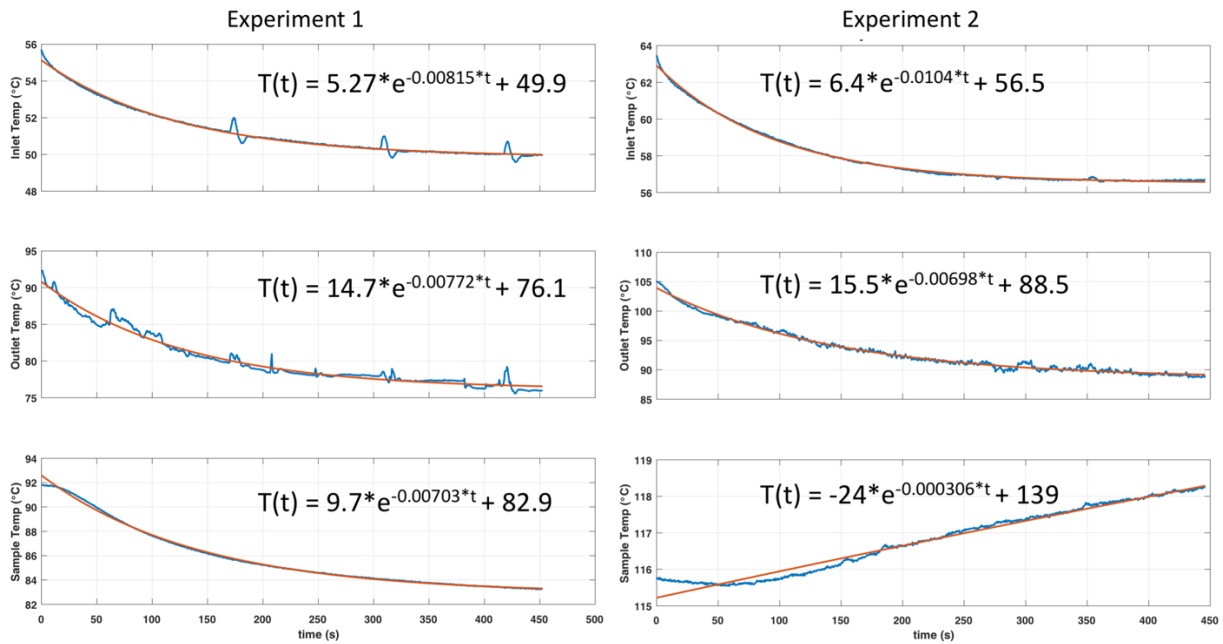
Fig 3.14: *Sub-experiments of Experiment 1 (left) and Experiment 2 (right) at a flow rate of 6 ml/min. First row depicts the temperature decay at the inlet, second row at the outlet and third row at the sample. The x-axis represents the time (s). Blue curve represents the recorded experimental data while the red curve is an exponential fitting curve of which functions are shown in each plot.*
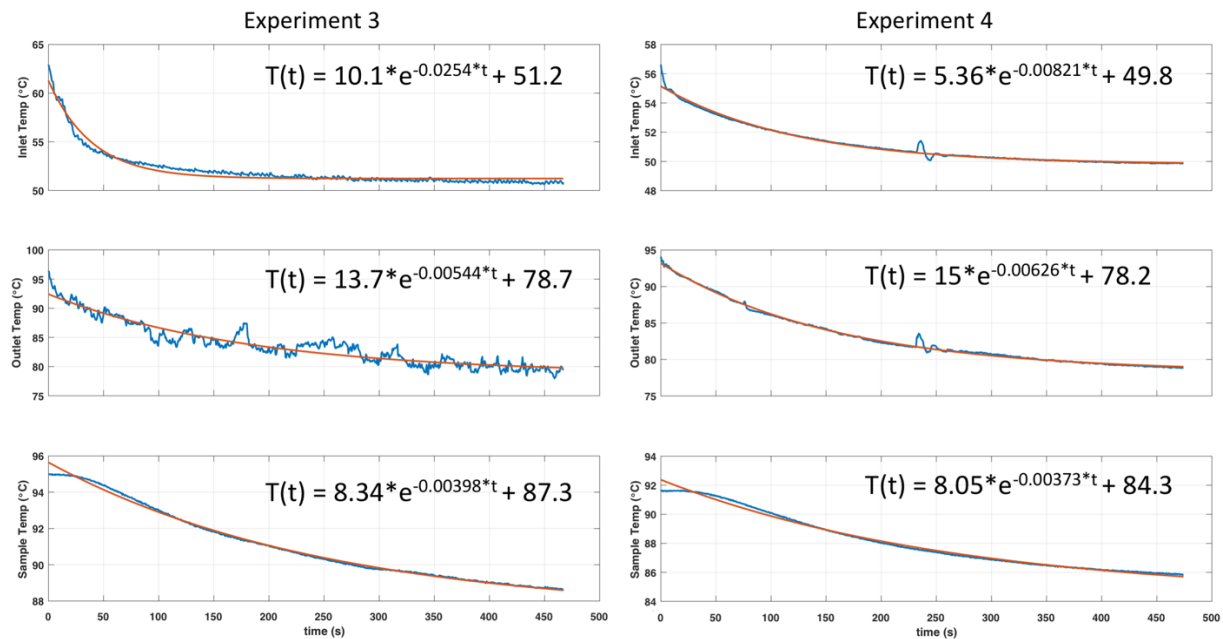
Fig 3.15: *Sub-experiments of Experiment 3 (left) and Experiment 4 (right) at a flow rate of 6 ml/min. For more information see Figure 3.14.*
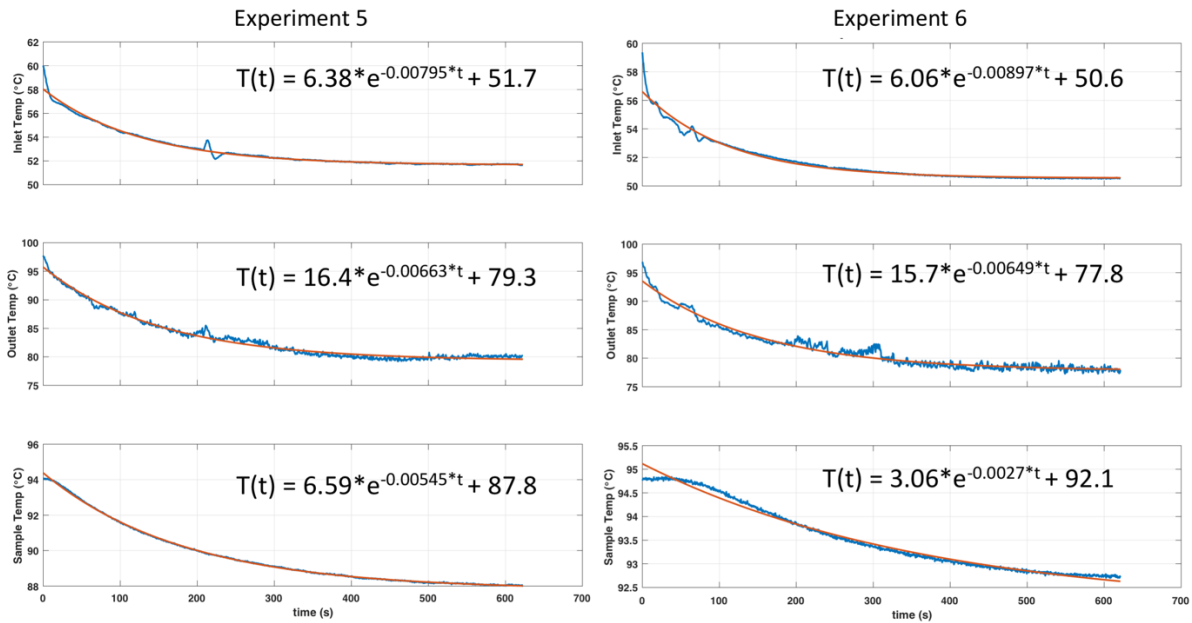
Fig 3.16: Sub-experiments of Experiment 5 (left) and Experiment 6 (right) at a flow rate of 6 ml/min. For more information see Figure 3.14.
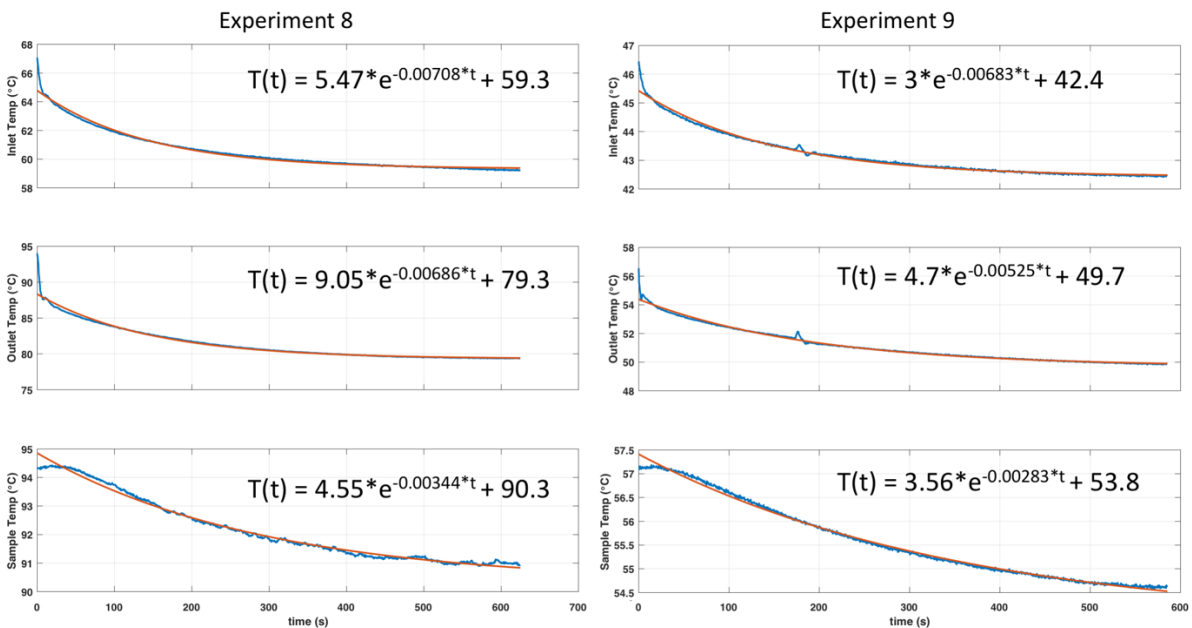
Fig 3.17: Sub-experiments of Experiment 8 (left) and Experiment 9 (right) at a flow rate of 6 ml/min. For more information see Figure 3.14.

The steady-state check (see *Chapter 2.6.4* for conditions) involves 47 sub-experiments to be analyzed within this project. 10 out of 47 sub-experiments experienced temperature fluctuations of more than 1% from the mean at the outlet or both the outlet and inlet within the last 60 seconds. This is 21.3% of sub-experiments that did not achieve steady-state per definition. However, this is mostly due to abnormal temperature peaks caused by unexpected flow rate fluctuations of the pumps. These fluctuations are usually equilibrated rather quickly.

3.2 3D Fracture Detection with AVIZO

In this subchapter, the results of the work done in the 3D image-analysis software AVIZO is presented. Each fracture/fluid pathway within the rock samples used in this project is presented and described in *Table 3.4*.

Exp.	Visualization	Description
1		The fracture is continuous from one side of the rock cylinder to the other. It is partly branched off in radial direction and slightly bent in axial direction.
2		The fracture is continuous. The direction of the fracture changes about halfway in axial direction and there are no major branches present.
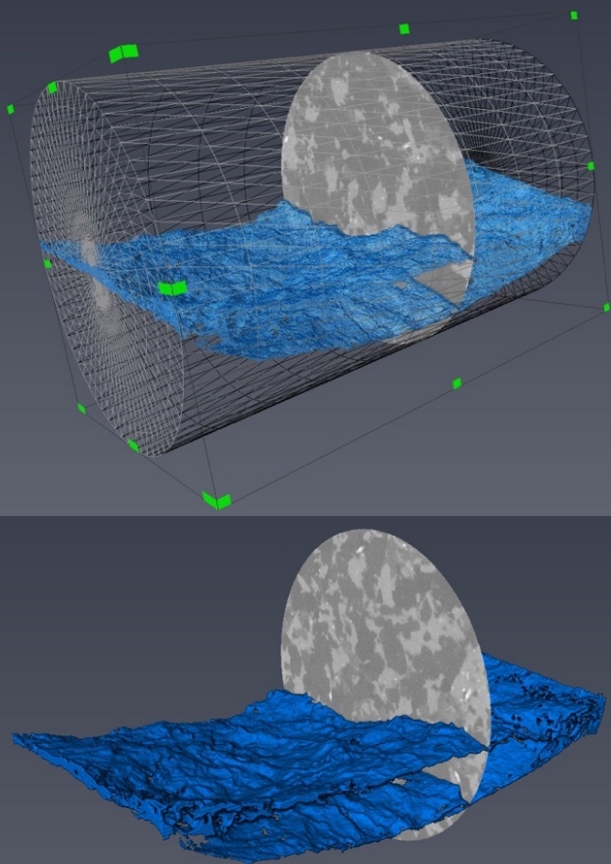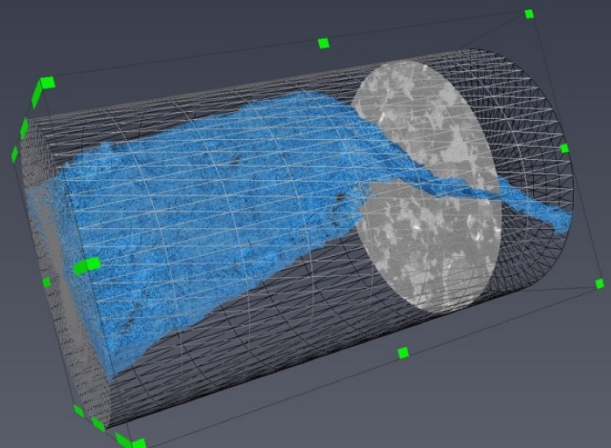
3		The fracture is continuous from one side of the cylinder to the other. There are no fracture branches visible and the fracture is slightly bent in axial direction.
4		The main fracture is continuous from one side to the other. There are no branches visible and the fracture is only slightly bent in axial direction. There is a small side fracture present that is not connected to the main fracture and not continuous from one side to the other.
5		The fracture is irregular compared to Experiments 1 – 4. The main fracture is continuous from one side of the cylinder to the other. One branch of the fracture runs until the middle of the sample in axial direction while another one branches off in radial direction to reach the side of the sample. The main fracture is bent in axial direction. Visualizations show the front view (top) and the back view (bottom)
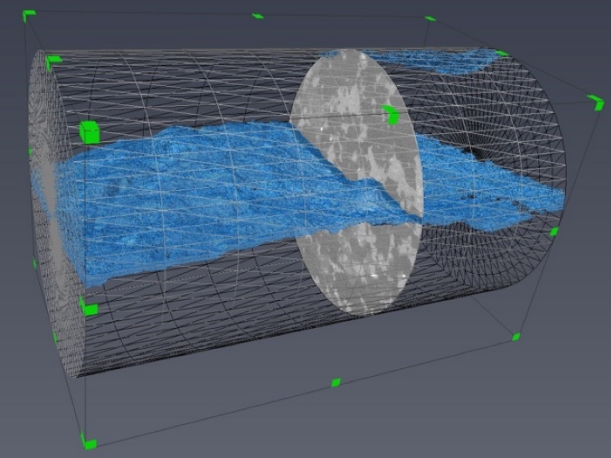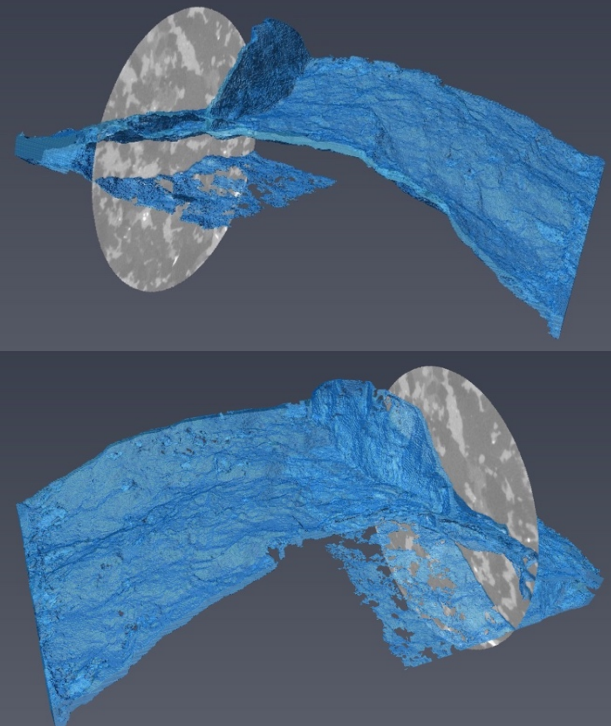
| 6 | | This experiment was supposed to be part of the benchmarking experiment series as explained in *Chapter 2.2*. The two saw-cut parts of the rock sample are most likely pressed closed during the experiment due to confining pressure. This is why the generated natural fracture is considered the main fracture where most of the fluid flow occurs. Two branches off the main natural fracture are visible. |
| 8 / 9 | | For benchmarking Experiments 8 and 9, the same sample was used with the same hole diameter. The drilled hole resulted in a very smooth fluid pathway with a diameter of 4 mm. |
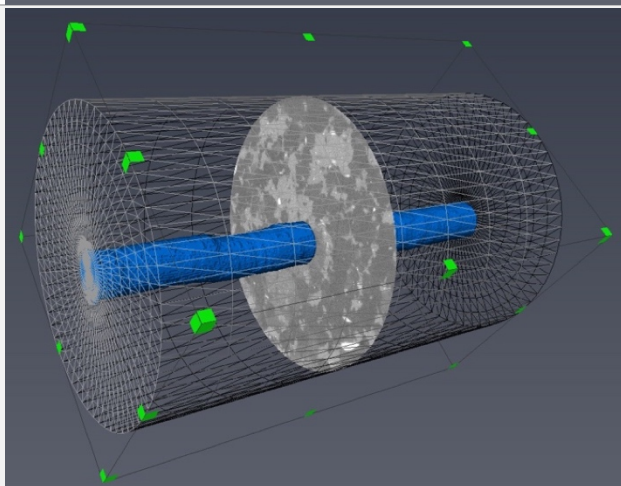
Table 3.4: Fractures or fluid pathways of Experiments 1 – 9 are coloured in blue. Most visualizations include a cylindrical rock sample outline a cross-section of the sample. Descriptions of the fluid pathways are in the right column.

Table 3.5 lists volume and area calculations for each fracture/fluid pathway in AVIZO. Area fractions are subtracted from the surface area calculations in AVIZO. The area fractions subtracted contain the edges of the fractures where either the fluid inlet and outlet are located or a border to the rubber jacket confining the sample. The total surface area therefore only represents rock material surface area. For reasons of comparison the volume of the fracture detected in AVIZO is also shown. It is not an important parameter in this project since it does not represent conditions found during experiments. It is expected that the fracture volume is much smaller due to 10 MPa of confining pressure squeezing the sample during experiments. However, the surface area is a reliable indicator of conditions occurring during experiments. The area ranking indicates which sample contains the highest fracture surface area (1; Exp 6) to the lowest fracture surface area (8; Exp 4 side). Number of branches is an indicator of the regularity of a fracture. Flatness is the ratio of the smallest to the medium eigenvalue of the covariance matrix. Flat objects have small values close to 0.

Experiment	Volume (mm³)	Surface Area (mm²)	Area subtracted (mm²)	Total Surface Area (mm²)	Area Ranking	Number of Branches	Flatness
1	765.1	4790.2	75.6	4714.6	4	1	0.049
2	769.7	5516.3	124.2	5392.1	2	0	0.096
3	743.8	3692.2	155.6	3536.6	6	0	0.026
4	1082.7	4556.7	163.9	4392.8	5	0	0.016
4 side	34.4	412.7	6.7	406.1	8	0	0.015
5	1074.2	5036.8	162.9	4874.0	3	2	0.171
6	1528.5	9722.2	206.2	9516.1	1	2	0.350
8 / 9	668.2	767.2	25.1	742.1	7	0	0.985

Table 3.5: Overview of measurements conducted in AVIZO for fractures/fluid pathways of each experiment

3.3 Numerical Simulations with COMSOL Multiphysics

3.3.1 Model with Constant Temperature Boundaries (2D)

Figure 3.18 depicts temperature distributions of the model at each flow rate simulated. The temperature distribution largely depends on the thermal conductivity of different materials used in the model.
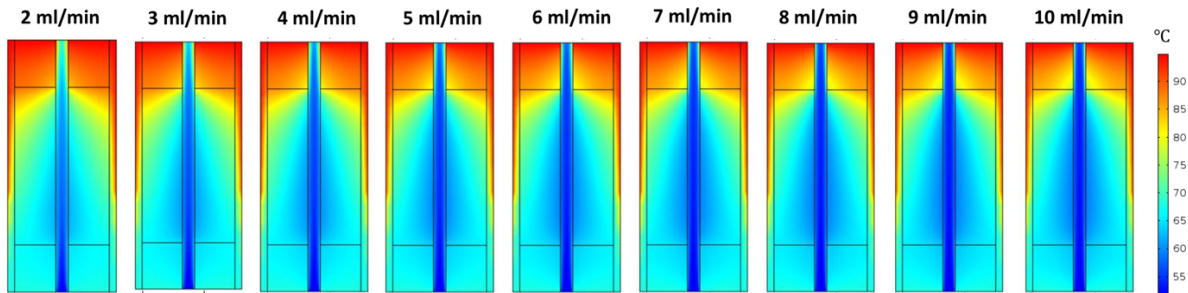
Fig 3.18: Temperature distribution in the model at steady-state flow conditions

Outlet minus inlet temperatures of the simulations are plotted in *Figure 3.19*. Additional to a simulated sample with a 4 mm diameter hole, the same tests were run with a 1 mm hole. The difference of the two curves in *Figure 3.19* is a vertical offset. A sharp drop in temperature differences can be seen at low flow rates for both sets of simulations. The curves look similar to an exponential decrease.
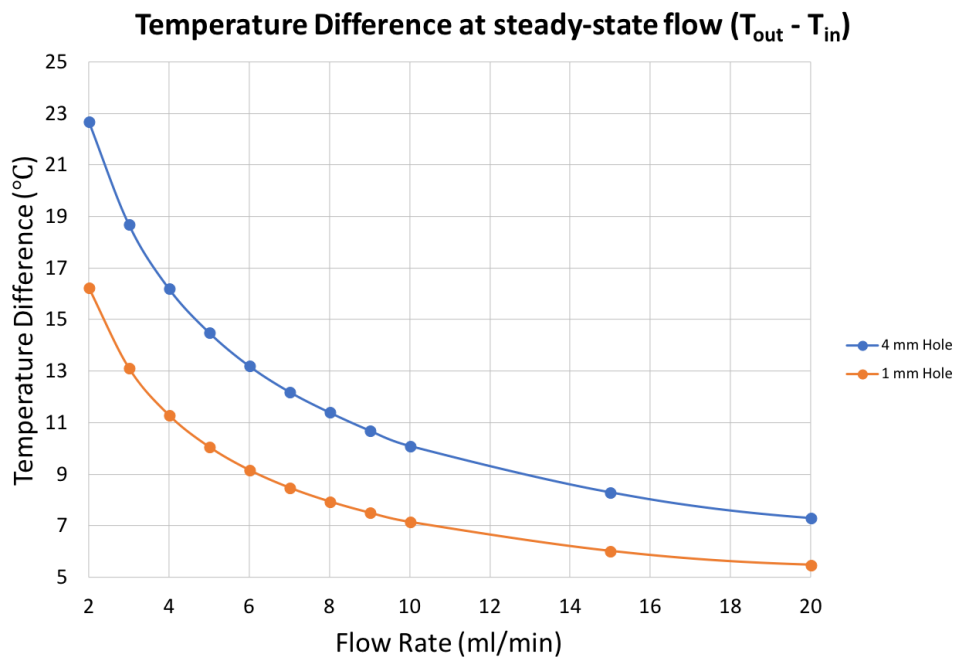
Fig 3.19: Outlet minus Inlet temperatures at steady-state flow conditions with constant Inlet temperatures for 2 different cases of drilled hole samples

3.3.2 Model with Constant Temperature Boundaries and Open Boundaries (2D)

a) Varying flow rates at constant aperture

3 different sets of simulations were conducted each with an individual aperture of 0.1 mm, 0.2 mm and 1 mm respectively. Resulting temperature differences between inlet and outlet are presented in *Figure 3.20*. It is clearly seen that there is practically no difference of the heat absorbed by the water at different apertures. Even at a flow along a fracture that is 10 times wider than originally, at a constant flow rate, the achieved temperature difference of the water is still the same. It should be noted, however, that an increasing fracture aperture at a constant flow rate causes a decrease of the fluid velocity along the fracture. It can be noticed that in all three sets of simulations, the temperature difference (absorbed heat by water) is decreasing with increasing flow rates. This happens at an increasingly lower rate at higher flow rates.
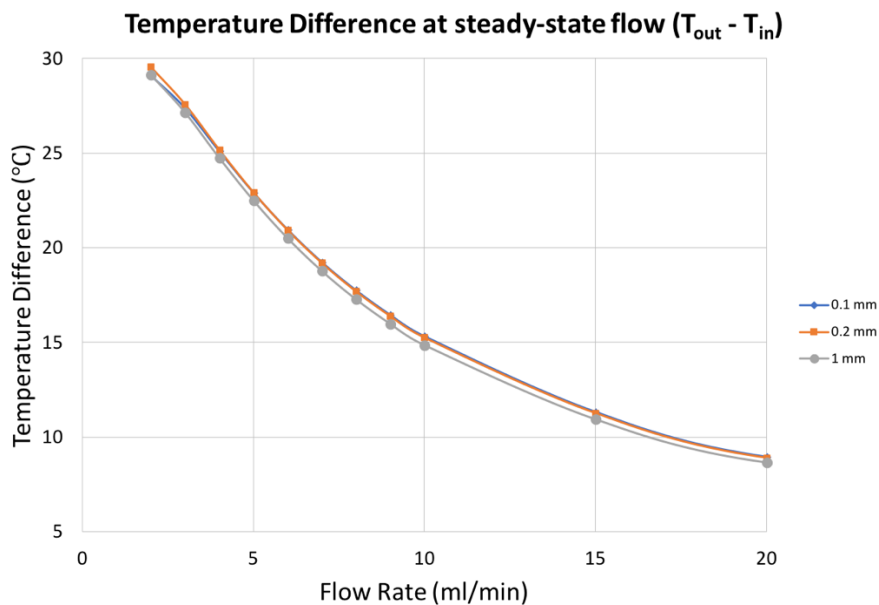
Fig 3.20: Outlet minus inlet temperatures at steady-state flow conditions with constant inlet temperatures for 3 different cases of individual fracture apertures (0.1 mm, 0.2 mm, 1 mm). Plotted values are listed in Table 8.3 (Appendix).

Referring to the similarity of the 3 graphs in *Figure 3.20*, it is expected that the temperature distribution inside the sample is very similar for all 3 sets of simulations. For more results focusing on aperture variations only, see section **b)** of this chapter. Therefore, only one case (sample with fracture aperture of 1 mm) of the evolution of temperature distribution over different flow rates is depicted in *Figure 3.21*. As the flow rate is increasing, the blue cold front across the sample is increasingly reaching closer to the outlet and causes a higher rate of cooling from the fracture towards the side boundaries of constant temperature.
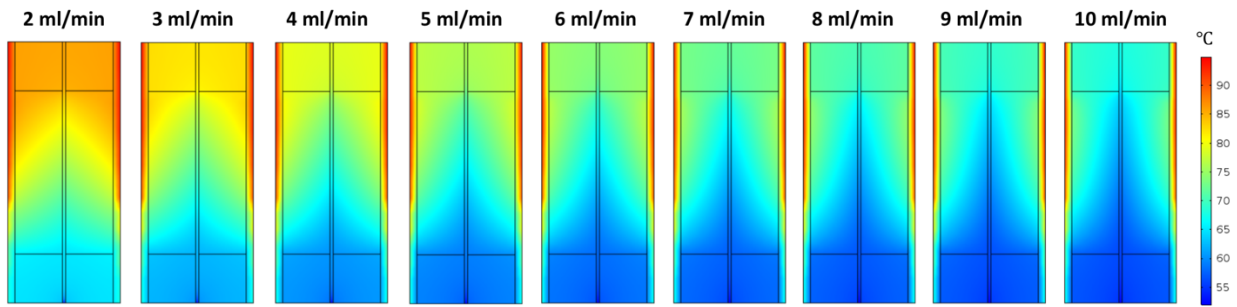
Fig 3.21: Temperature inside the sample at steady-state flow conditions as simulated in COMSOL at different flow rates. The color bar on the right shows the color scale of temperatures in °C.

b) Constant Flow Rates versus Constant Velocity at varying Fracture Aperture

In Experiments 2 and 6, part of the workflow was to vary the fracture aperture while keeping the flow rate constant. This case was simulated in COMSOL as well. Since it is known that a constant flow rate at changing fracture aperture results in varying fluid velocities, one set of simulations was fixed at a realistic fluid velocity of 0.033 m/s at varying fracture apertures. *Figure 3.22* depicts the results from both sets of simulations. Practically no difference is seen in heat exchange as the fracture aperture increases at a constant flow rate. Increasing the fracture aperture by 80 times (from 0.05 mm to 4 mm) results in a decrease of temperature difference of only 1.07 times (from 21.1 °C to 19.8 °C). However, similar to an exponential decay, the temperature difference between inlet and outlet decreases sharply as the fracture aperture increases at a constant velocity.
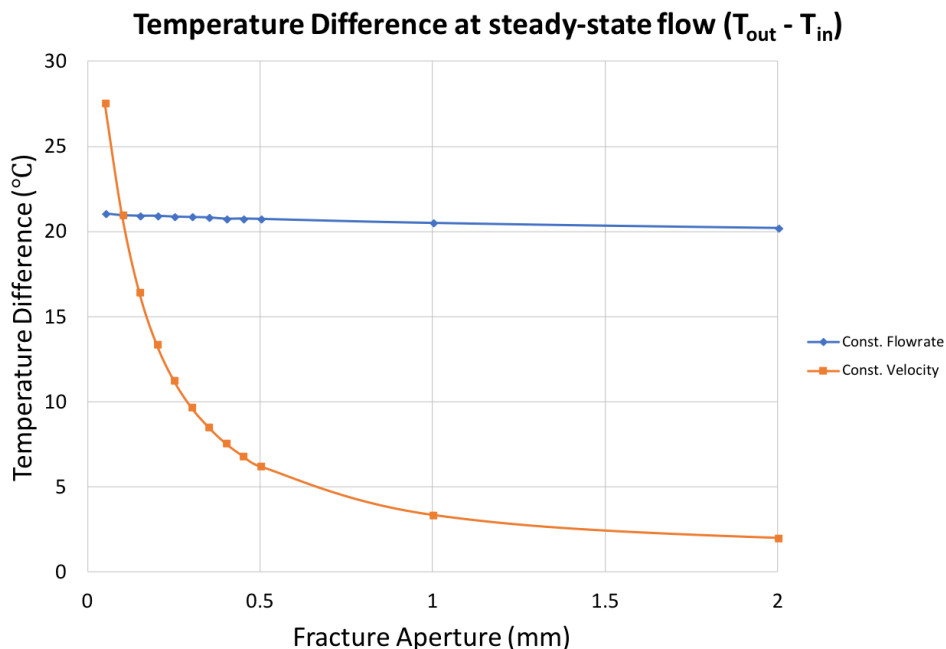
Fig 3.22: Outlet minus Inlet temperatures at steady-state flow conditions with constant injection temperatures. Blue graph depicts the results at a constant flow rate of 6 ml/min throughout the entire aperture range. Orange graph depicts the results at a constant fluid velocity of 0.033 ml/min over the entire aperture range (which matches with the flow rate of 6 ml/min at an aperture of 0.1 mm). Plotted values are listed in Table 8.4 (Appendix).

Since there is a significant alteration of temperature differences with varying fracture aperture at a constant fluid velocity, the temperature distribution of this simulation set is presented in *Figure 3.23*. As the fracture is widened, the sample is increasingly cooled down. This goes hand-in-hand with the increased fluid volume flushed through the sample at larger apertures.
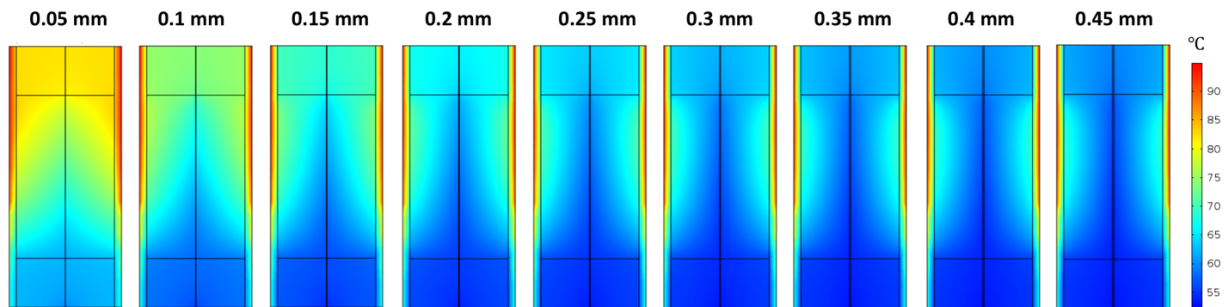
Fig 3.23: Temperature inside the sample at steady-state conditions as simulated in COMSOL at different fracture apertures. The color bar on the right shows the color scale of temperatures in °C.

c) *Varying Geometry and its impact on temperature difference and distribution*

As seen in the experimental part of the thesis, every fracture generated has an individual geometry that is difficult to predict. Different fracture geometries are incorporated in the simulation part as well. The straight main fracture in the middle of the sample was not changed while side-fractures are added for this simulation. In the first case, one side fracture was added with approximately the same aperture and length as the main fracture. In the second case, another side fracture was added by mirroring the first side fracture along the main fracture axis. The third case is basically a modification of the second case by extending the length of the fluid pathway on both sides of the main fracture. The geometry of the three cases and the heat distribution at varying flow rates are depicted in *Figure 3.24*. Comparing the three geometrical cases, it is seen that the blue cold front is propagating further towards the outlet in the first case as compared to the second and third case. A reduced temperature difference between inlet and outlet is therefore expected in simpler geometrical cases. Cases 2 and 3 are nearly identical in terms of temperature distribution in the sample.
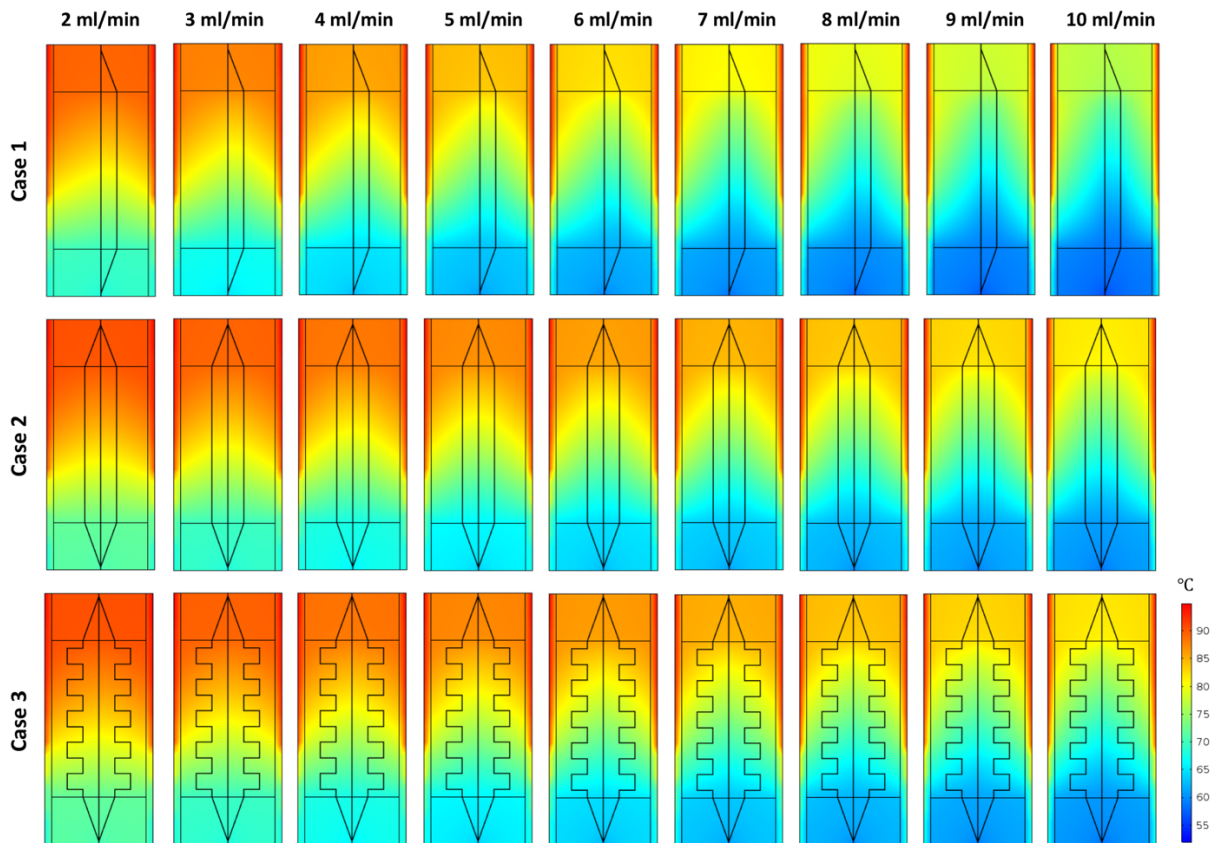
Fig 3.24: Temperature inside the sample at steady-state flow conditions as simulated in COMSOL at different flow rates. The top row shows the first geometrical case with 1 side fracture; the middle row depicts the second geometrical case with 2 side fractures; the bottom row depicts case 3 with two modified side fractures. The color bar on the bottom right shows the color scale of temperatures in °C.

Water injection temperatures for the simulations are still kept constant at 52.1 °C for all cases. Since the calculated inlet temperatures do not match with the set injection temperature at lower flow rates, the constant injection temperature is taken as a reference for the derived temperature differences. *Figure 3.25* illustrates the development of temperature differences with increasing flow rates in three different geometrical fracture settings. Section **a)** of this subchapter presents the temperature behavior for a single straight fracture with varying flow rates. For comparative reasons, the results of a single straight fracture are plotted along the three new geometrical cases as illustrated in *Figure 3.24* above. The temperature differences are the smallest for the simple straight fracture case throughout all flow rates. A shift upwards towards higher temperature differences can be seen as we move to a more extensive fracture network of Case 1 and Case 2. The curves of Cases 1 and 2 are also less curved at lower flow rates, therefore the temperature difference does not drop as fast as it is the case for the straight single fracture. Again, the results of Cases 2 and 3 are nearly identical.
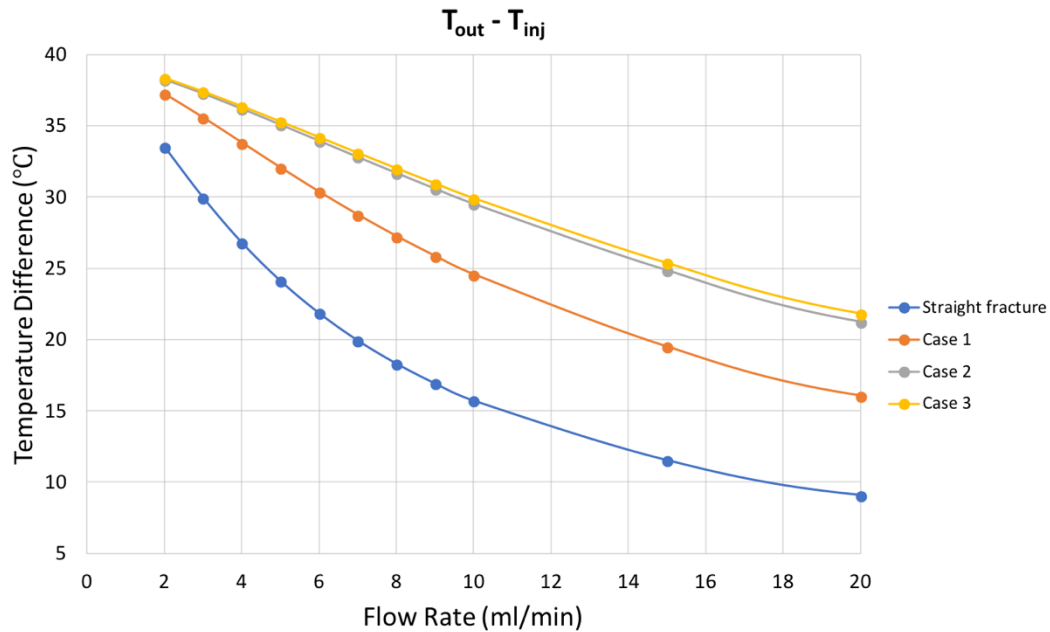
Fig 3.25: Outlet minus injection temperatures at steady-state flow conditions with constant injection temperature (52.1 °C) for 3 different cases of individual fracture geometries. Straight fracture results as shown in Figure 3.20 (blue); Case 1 with one side fracture (orange); Case 2 with two side fractures (grey); Case 3 with two modified side fractures (yellow). Plotted values are listed in Table 8.5 (Appendix).

3.3.3 Axisymmetric extended model

a) Time-dependent no-flow conditions (Stage A and B of Figure 3.1)

Firstly, the simulation is run over a short time period of 3 minutes with time steps of 20 seconds. Note that the simulations in section **a)** are now run time-dependent unlike simulations of *Chapter 3.3.1 – 3.3.2* that are run in stationary mode. Initial convective and heating behavior of the oil is investigated. The laminar flow along the fluid pathway is set to 10^{-4} ml/min, so no-flow conditions can be assumed. *Figure 3.26* illustrates the temperature distribution every 20 seconds as the model is heated up. A clear temperature variation between bottom and top of the model can be seen with the top heating up quickly and the bottom staying at a relative constant temperature of 25 °C.

Results
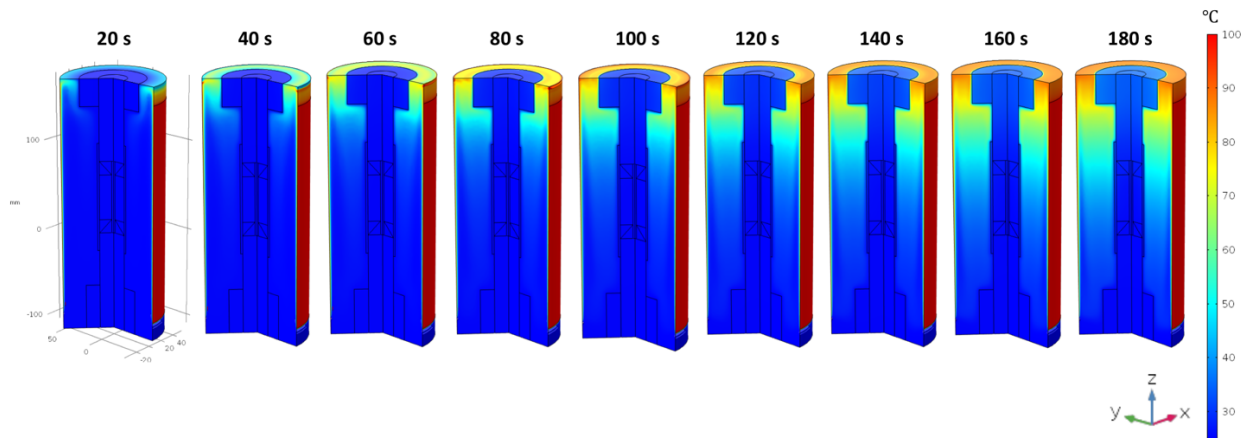
Fig 3.26: Temperature distribution at every time step of 20 s with heating furnace set to 100 °C.

In order to illustrate the temperature distribution at different heights (z-coordinate) of the apparatus, cross-sections of the xy-coordinate space after 180 s are depicted in *Figure 3.27*.
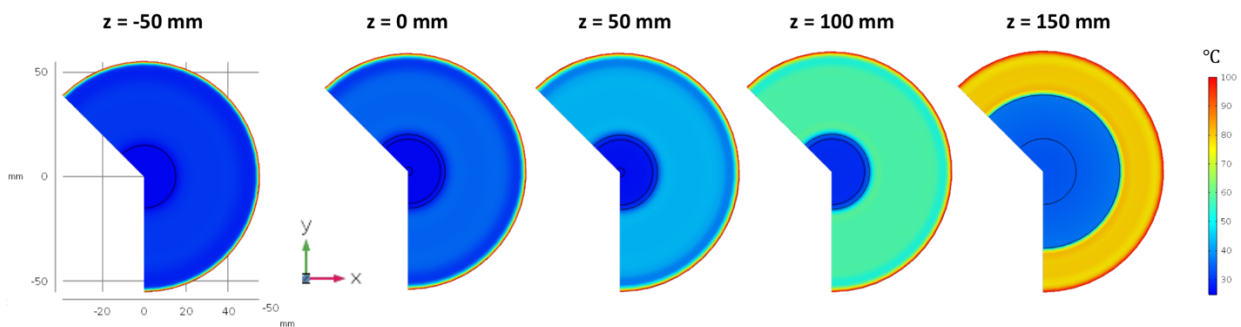
Fig 3.27: Temperature distribution of xy-plane cross-sections at heights (z) from -50 mm to 150 mm. At time point 180 s (see Figure 3.26).

Secondly, the simulation is run over a long time period of 120 min with time steps of 1 min. No-flow conditions are applied again. In addition to the heat distribution trend depicted in *Figure 3.28*, the temperature at the sample location (T_{sample}), the outlet temperature (T_{out}) and inlet temperature (T_{in}) are plotted against time in *Figure 3.29*.
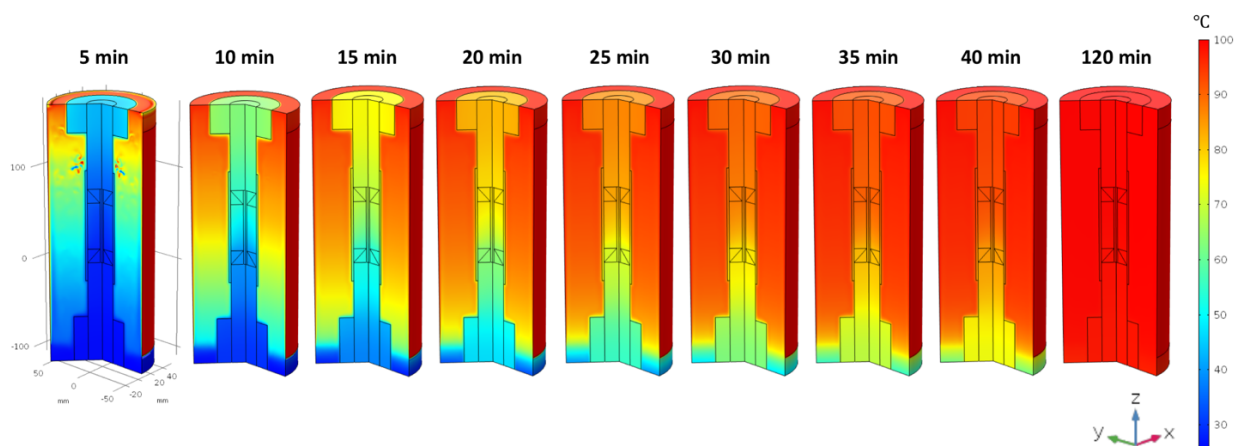
Fig 3.28: Temperature distribution over a time period of 120 min with heating furnace set at 100 °C.

Figure 3.28 clearly shows the gradual heating from the top of the setup to the bottom. After a certain time, a uniform temperature distribution is achieved which represents a stationary condition with no more changes in temperatures over time. This achievement of a stationary temperature condition is also depicted in *Figure 3.29* where temperatures at three different locations are calculated at each time step of 1 min. The temperatures at the outlet (T_{out}) and sample (T_{sample}) are increasing at a similar rate while the heating at the inlet (T_{in}) is slightly delayed due to the vertical temperature gradient during the heating period. However, after approximately 120 min all three temperatures reach an equilibrium at 100 °C.
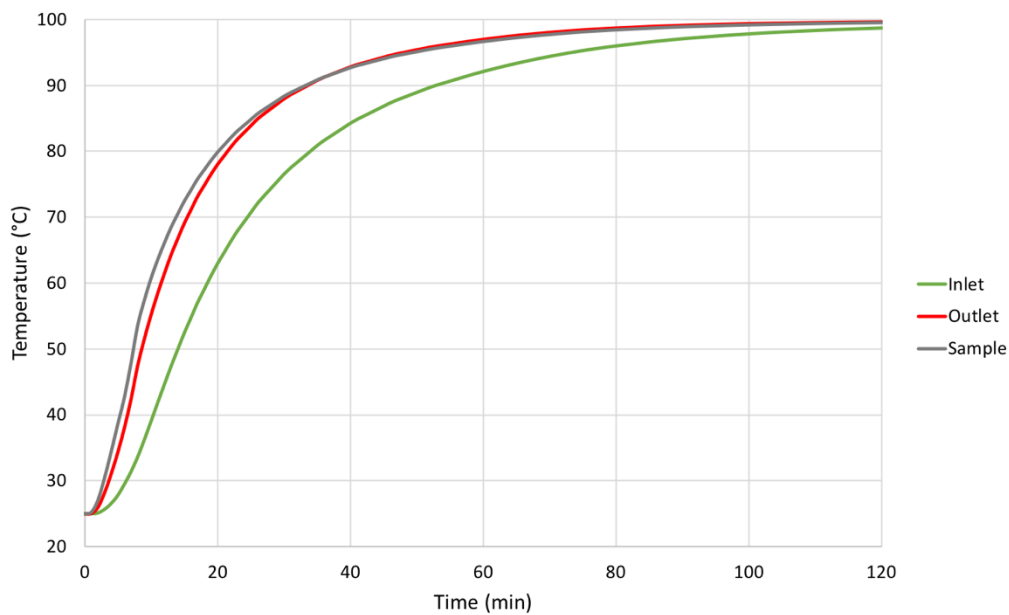
Fig 3.29: Temperatures ($T_{in}, T_{out}, T_{sample}$) over a time period of 120 min with heating furnace set at 100 °C.

A uniform temperature was achieved throughout the entire apparatus at a state of equilibrium. This does not represent the conditions occurring in the experiments where a vertical temperature gradient is observed even at an equilibrium. Therefore, the solution of the simulation after 120 min shown in *Figure 3.28* is reevaluated with a constant heat sink at the top and bottom metal parts. A constant temperature boundary condition of 40 °C instead of an open boundary is applied. *Figure 3.30* depicts the heat distribution with altered boundary conditions. A notable vertical temperature gradient can then be seen at a state of equilibrium. The temperature at the inlet was computed to be 65.8 °C, at the outlet 71.5 °C and at the sample 76.5 °C.
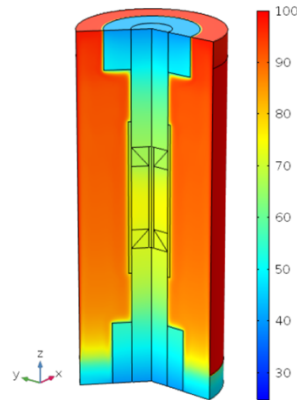
Fig 3.30: Heat distribution once thermal equilibrium is achieved (120 min). Same simulation as in Figure 3.28 apart from the top and bottom metal parts assigned as constant-temperature heat sinks instead of open boundaries.

b) Stationary flow conditions (End of Stage C of Figure 3.1)

Now, the model is solved with an imposed constant flow rate along the fluid pathway in a state of equilibrium (stationary solver). Flow rates of 2 ml/min to 10 ml/min and their corresponding heat distribution is displayed in *Figure 3.31*. In order to compare heat transfer behavior at different fluid pathway widths, the diameter of the drilled hole was first kept at 4 mm (same as Experiment 8) for the first set of simulations and then altered to 1 mm. As the flow rate increases, the sample and the metal parts at the top and bottom of the sample are increasingly reaching lower temperatures. The surrounding oil stays at a relatively constant temperature. In both cases with 4 mm and 1 mm diameter, the temperature distribution alteration with flow rate is relatively similar.
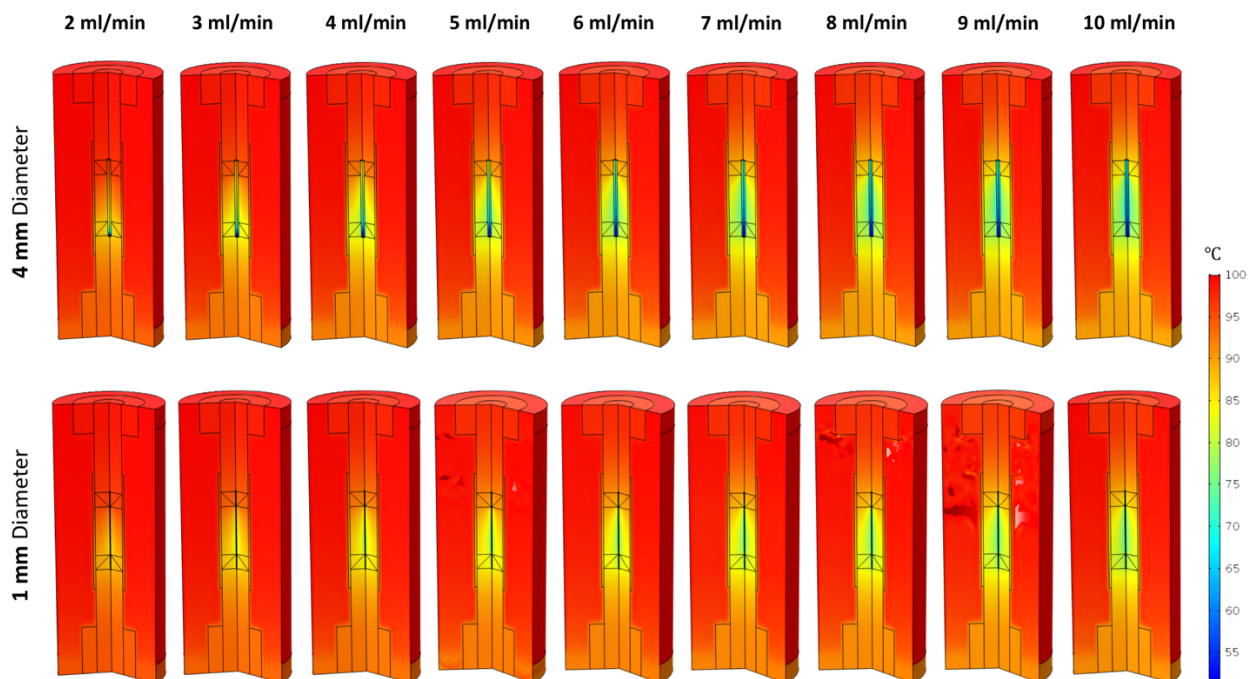
Fig 3.31: Temperature distribution at varying constant flow rates with a cylindrical fluid pathway of 4 mm (top row) and 1 mm (bottom row) in diameter. Steady-state flow conditions are achieved.

Figure 3.32 displays graphs of the calculated temperatures at each of the three measurement locations with varying flow rates. The inlet temperatures slightly change with each flow rate and do not match with the constant injection temperature (52.1°C). The outlet temperatures experience the most significant decrease as the flow rate is increased whereas the sample temperatures stay inside a range of less than 10 °C variation throughout flow rates 2 ml/min to 20 ml/min.
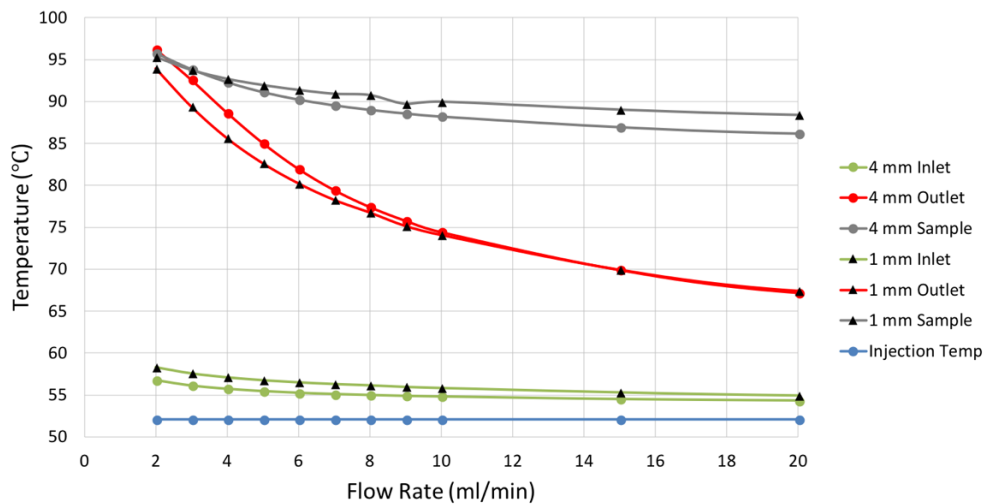
Fig 3.32: Absolute temperature values at three locations of the models plus the constant fluid injection temperature at steady-state flow conditions. Both cases with a 4 mm diameter fluid pathway and 1 mm diameter are displayed. Plotted values are listed in Table 8.6 (Appendix).

In order to quantify heat production efficiency, the temperature differences between the fluid outlet (production) and the fluid inlet location are plotted in *Figure 3.33*. Due to initial heating of the injection fluid, the inlet and injection temperature do not match and the injection temperature is taken as a reference. As the flow rate increases the temperature difference (ΔT) decreases. This occurs at an increasingly slower rate. Both diameter cases show similar values with larger differences at small flow rates and a convergence with increasing flow rates. At flow rates higher than 10 ml/min, both cases do virtually match.
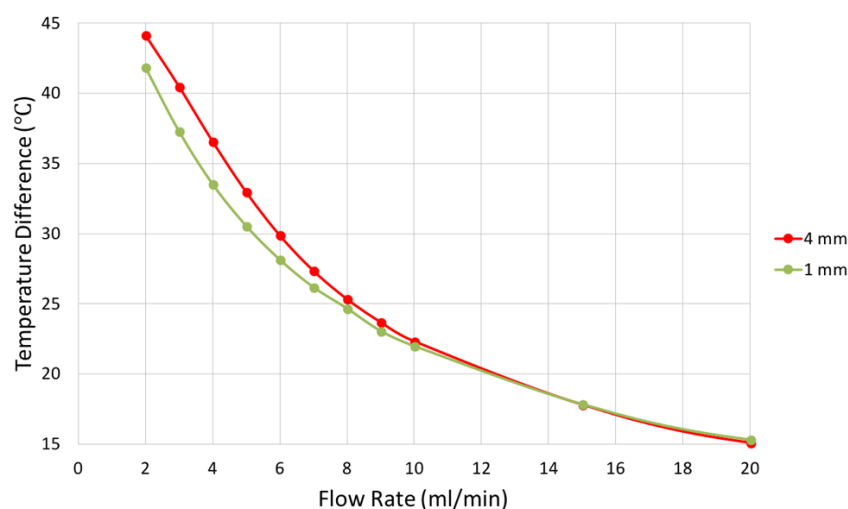
Fig 3.33: Outlet temperature (T_{out}) minus injection temperature (T_{inj}) plotted against the flow rate. Both cases of fluid pathway diameter of 4 mm as well as 1 mm are represented. Plotted values are listed in Table 8.7 (Appendix).

Results

c) Time-dependent flow conditions (Stage C of Figure 3.1)

Rather than flow at a stationary condition, the results of a time-dependent sub-experiment simulation are now presented. Firstly, the temperature development at the inlet, outlet and sample location are documented in *Figure 3.34*. An exponential cooling behavior can be seen at the sample and outlet location while the inlet temperature is governed by the constant injection temperature during flow conditions. The sample temperature reaches an equilibrium at about 90 °C, while the temperature equilibrium for the outlet lies at around 82 °C.
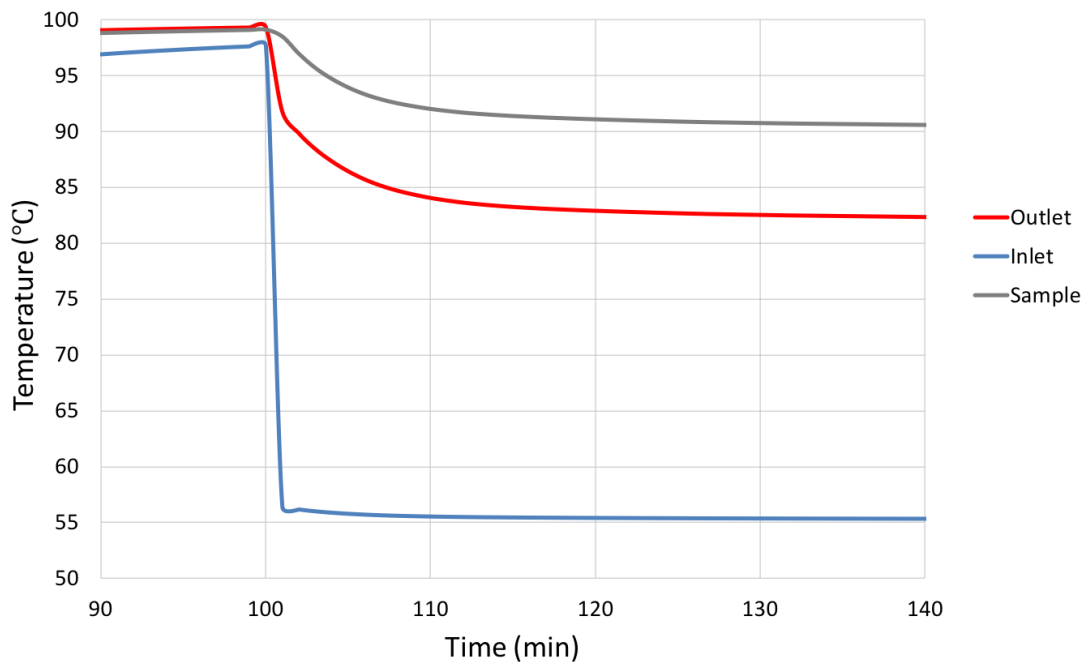
Fig 3.34: Time-dependent temperatures of a simulated sub-experiment with a flow rate of 6 ml/min. The flow is imposed (constant injection temperature of 52.1 °C) starting at 100 min.

In order to see the temperature distribution along the fluid pathway and how it evolves with time, *Figure 3.35* depicts this evolution starting at 101 min. A clear trend towards temperature equilibrium can be seen as time progresses. An initially steeper temperature gradient between inlet and outlet slightly flattens as time progresses. The temperature gradient between inlet and outlet is not a linear curve but is rather bent. The fluid heats up quickly close to the inlet and takes up increasingly less heat as it travels towards the outlet. A temperature spike is observed across the entire time range at the height of about 48 mm inside the rock sample.
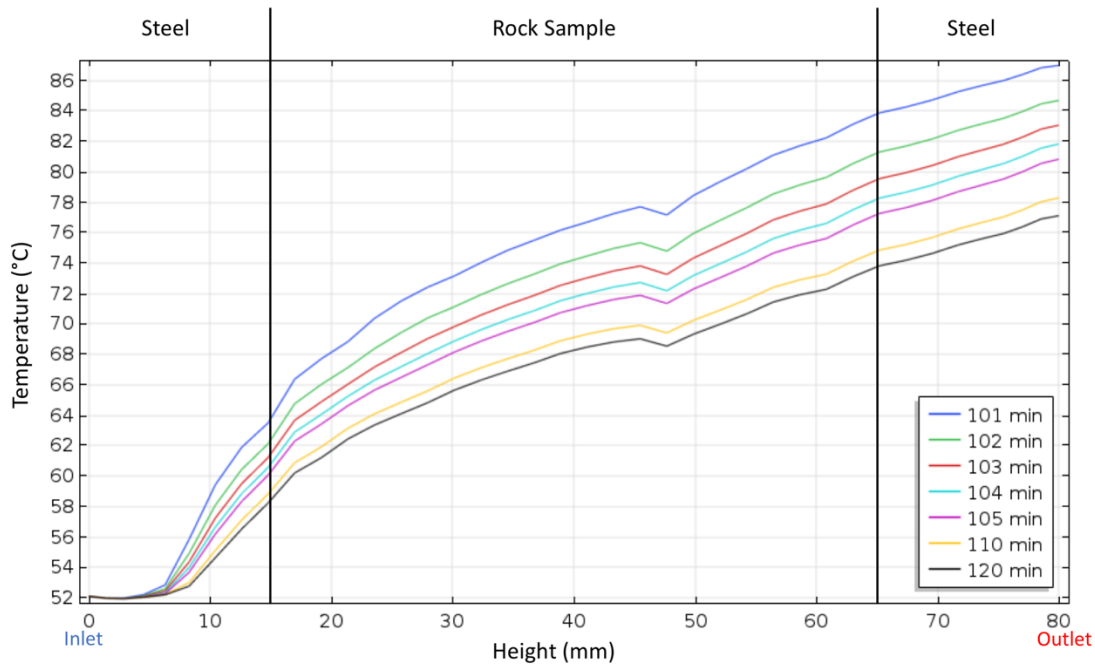
Fig 3.35: Temperature distribution along the middle of the cylindrical fluid pathway of the sample during the simulated sub-experiment at a flow rate of 6 ml/min. Seven different curves are computed ranging from 101 min (1 min after flow started) to 120 min. The x-axis represents the height of the sample including steel wedges/cylinders with the inlet at 0 mm and the outlet at 80 mm. The y-axis represents the temperature at each location along the fluid pathway.

In *Figure 3.36* the temperature distribution inside the apparatus is depicted at the same time points of the simulated sub-experiment as in *Figure 3.35.* Initially a relatively constant temperature distribution predominates before flow condition occurs. The rock sample increasingly cools down as time progresses. As also seen in *Figure 3.34*, after about 20 minutes of imposing a constant flow rate, a temperature equilibrium is practically reached. Increasingly smaller temperature changes can be observed the longer a flow is imposed due to the exponential cooling behavior.
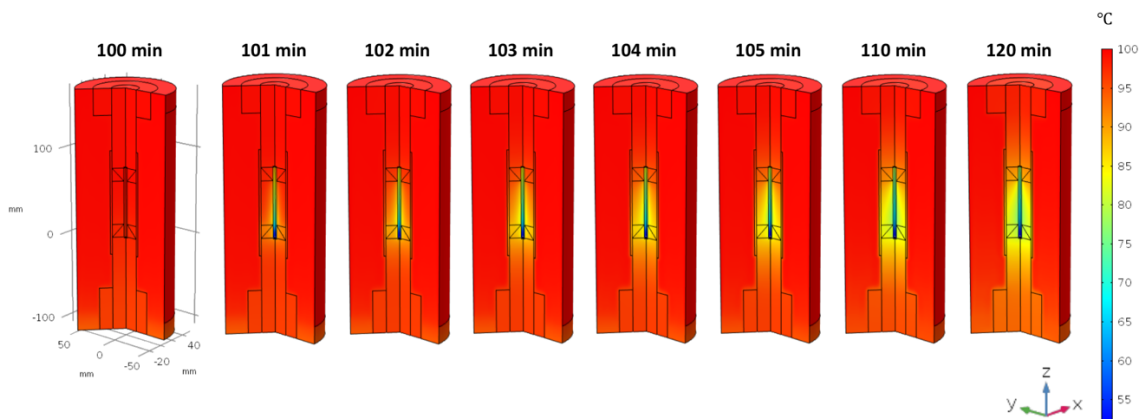
Fig 3.36: Temperature distribution inside the apparatus after a constant flow of 6 ml/min is imposed at 100 min.

Results

According to the plots of *Figure 3.34* an exponential cooling behavior is observed at the outlet and the sample location. Similar to *Chapter 3.1.4* an exponential fitting curve is computed for the simulation case which is depicted in *Figure 3.37.* The curve functions yielded suggest a higher and faster temperature drop at the outlet compared to the sample thermocouple location as well as a lower equilibrium temperature.

$$T(t) = 14.64 * e^{-0.0059*t} + 83.3$$

$$T(t) = 8.65 * e^{-0.0034*t} + 90.9$$
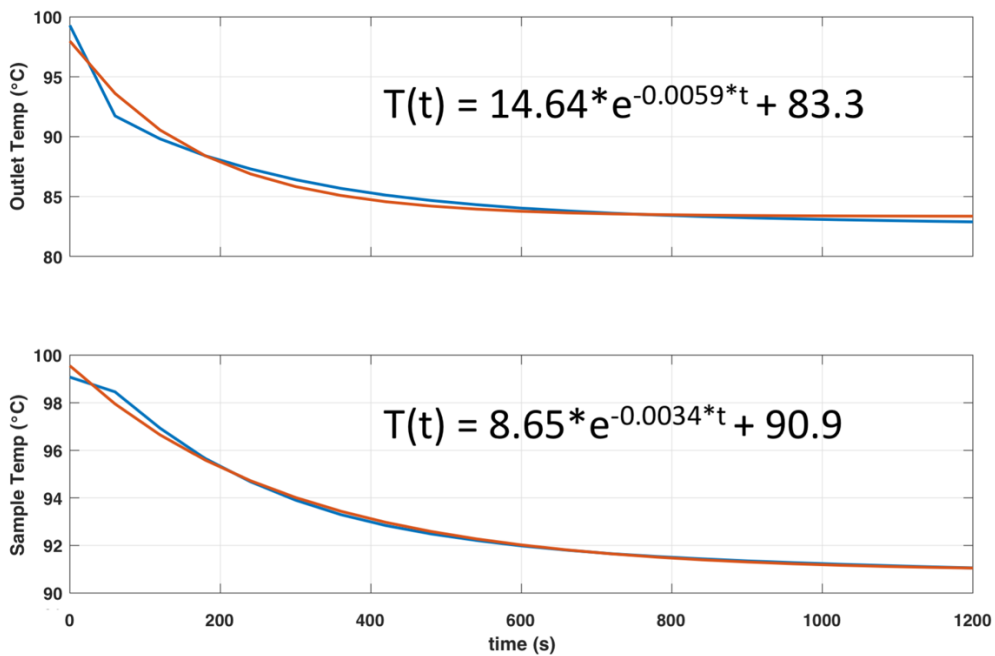
Fig 3.37: Sub-experiment simulated in COMSOL at a flow rate of 6 ml/min. Top figure depicts the temperature decay at the outlet, bottom figure at the sample. The x-axis represents the time (s). Blue curve represents the computed temperature values of the simulation while the red curve is an exponential fitting curve of which functions are shown in each plot.

4. Discussion

4.1 Effect of crucial parameters on heat transfer

Several parameters were varied throughout different experiments and simulations. The parameters flow rate, fracture aperture and rock temperature were altered manually and in a controlled manner while, e.g., the fracture permeability and the pore fluid pressure were indirectly changed depending on the aforementioned parameters. The fracture geometry and therefore fracture surface area naturally varies between experiments and was manually altered in simulations. The results have shown that all these parameters have an impact on the heat transfer processes within the system in either a direct or indirect way. This impact (or lack thereof while expected) on the heat transfer between fluid and solid will be discussed in detail from one parameter to the other.

Summarizing the results, it was generally observed that increased flow rates cause decreased heating per unit volume of fluid and at the same time increased cooling of the rock. It means that at increased flow rates, more heat is withdrawn from the system per unit time. Varying fracture apertures (between 0.05 and 0.5 mm in experiments and 0.05 to 4 mm in simulations) at constant flow rates did not cause a notable difference in heat transferred while it did at constant fluid velocities. Increased rock temperatures result in increased heating of the fluid. The fracture surface area does not seem to have a high impact on heat transfer. However, altering the extent of the fracture, i.e., generate additional branches while both the fracture surface area and volume are changed does have an impact.

4.1.1 Volumetric Flow Rate

The experiments generally imply that there is a notable difference in exchanged heat between solid and fluid as the volumetric flow rate is altered. *Figure 3.2* already shows, as the volumetric flow rate increases the temperature measured at different locations at steady-state flow conditions decrease significantly. Since higher flow rates at a relatively constant fracture aperture imply higher fluid velocities along the fluid pathway as well, the fluid-rock or fluid-fluid contact (the time each water particle "touches" a rock particle or another water particle) occurs within a shorter time period. Due to the no-slip condition along the fracture walls, the fluid velocity at the solid-fluid contact is equal to that of the solid boundary, therefore zero (Day, 1990). At zero velocity condition, the predominant heat transfer process is conduction according to Fourier's law. The further we move towards the middle of the fluid pathway; the more convective/advective heat transfer dominates over conductive heat transfer (Arslan and Huber, 2013). Therefore, the higher the velocity/flow

Discussion

rate, the more convection/advection dominates and the less heat is transferred by conduction from the solid to the fluid which results in less fluid heating. In other words, at higher flow rates water generally spends less time within the fracture and thus there is less time to heat up. In *Figure 3.3* temperature changes in percentage between no-flow and steady-state flow conditions at the outlet, inlet and sample are illustrated. The rate at which this temperature change decreases with increasing flow rates is higher at the outlet than at the inlet and sample. This empirical fact implies that the heat taken up by the fluid is most sensitive to flow rate alterations along the fracture between inlet and outlet rather than in other parts of the apparatus. There is heat transfer occurring prior to the inlet location as the fluid flows through the pore fluid lines within the pressure vessel towards the sample. This is why the non-constant inlet fluid temperature is measured throughout the experiments. Fluid temperature drops at the inlet occur at a lower rate as the smaller temperature variations with changing flow rates show. This fact can be explained with the length of the fluid pathway leading to the inlet as compared to the fracture length. Since the fluid pathway prior to the inlet is much longer, the fluid is exposed to a hot environment over a longer period of time. Similar to exponential cooling of materials, heating of materials (water here) also occurs in an exponential pattern approaching a temperature equilibrium. At any flow rate, the water therefore is closer to an equilibrium temperature than it is flowing along the "short" fracture. Close to a state of equilibrium, changes occur at a lower rate than far from a state of equilibrium.

At the sample location, the temperature changes very little between no-flow and steady-state flow in the range of about -8 to 2% across all sub-experiments. It is important to mention that temperature changes at the sample greatly depend on the placement of the thermocouple with respect to the orientation of the fracture. Initially not much attention was spent to place the sample thermocouple on the in-tact rather than the fractured side of the rock sample. At the sample thermocouple location, solid-fluid heat transfer occurs, so that hot fluid (oil) is transferring heat to the colder solid (rubber). This is different than heat exchange along the fluid pathway, where hot solid (rock) is transferring heat to the colder fluid (water). In an ideal case where the thermocouple is placed on the in-tact side of the sample, heat is withdrawn by conductive heat transfer from the outside of the sample towards the fluid pathway. In a non-ideal case, there is only the rubber jacket in between the convecting oil outside the sample and the convecting/advecting water along the fluid pathway. *Figure 4.1* illustrates the ideal and non-ideal case of thermocouple placement.
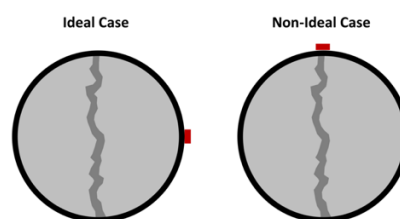
Fig 4.1: Ideal and non-ideal case of sample thermocouple placement (red). Cross-section of a rock sample with a fracture along the middle and rubber jacket in black.

A slight negative temperature change in 5 out of the 6 fracture experiments imply that more heat is withdrawn by conductive behavior than heat is resupplied by convecting oil outside of the sample. Similar to the inlet and outlet temperature, this is only the case until a thermal equilibrium has established where the withdrawn heat equals the supplied heat (see also *Chapter 4.4*). Such small temperature changes at the sample location also imply that in fact the entire rock sample is cooling down, but the temperature drop response is delayed due to conduction being less efficient as compared to advection occurring along the fluid pathway. As seen in COMSOL simulations, the proximity to the heat withdrawing location (fluid pathway) defines to what degree a specific part of the rock is cooled down at steady-state flow conditions. *Figure 4.2* illustrates the predominant heat transfer processes in the conducted experiments.
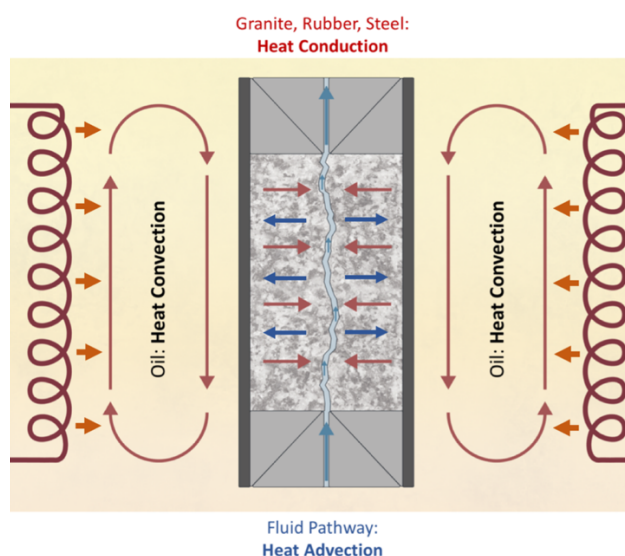
Fig 4.2: Heat Transfer domains within the experimental samples and surrounding oil volume. The winding wires on the side depict the heat source (furnace).

An interesting trend can be observed in *Figure 3.4* as well, where the temperature difference between sample (T_{sample}) and outlet (T_{out}) is increasing as the flow rate is increasing. This again makes sense since the higher the flow rate, the more heat is withdrawn from the rock at the fracture location that needs to be resupplied by conductive heat transfer in a state of equilibrium. Higher temperature differences in a certain material along a fixed distance lead to higher heat transfer rates (Wendl, 2015).

The trend of less heat extraction of the fluid at increasing flow rates as observed in the experiments can be reproduced accurately in the COMSOL simulations as well. *Figure 3.21* clearly depicts a temperature distribution trend inside the sample at increasing flow rates. At a low volumetric flow rate such as 2 ml/min, the heat can still be efficiently resupplied originating from the constant temperature boundaries on the side of the sample sketch. At high flow rates such as 10 ml/min the cold front has propagated much further in a state of equilibrium and therefore imposes smaller temperature differences between inlet and outlet. These

Discussion

smaller temperature differences in turn result in a lower heat production per unit volume of fluid. *Figure 3.20* shows the trend of decreasing temperature differences with increasing flow rates that is independent from the fracture aperture. The curve behaves in an exponential way and approaches zero temperature difference as the flow rate runs to infinity. Zero temperature difference is however never achieved since the fluid always takes up a certain fraction of heat that increasingly cools down the rock. This small fraction of heat taken up by the fluid at very high flow rates might however barely be measurable due to very high fluid volumes.

Using *Equation 8* of *Chapter 2.6*, a potential power production for the fluid flow simulated in COMSOL Multiphysics is calculated based on the resulting temperature differences and flow rates. Calculated from results of *Table 8.3, Figure 4.3* shows a trend of increasing Power Production at higher flow rates. Initially a sharp increase in power production can be seen as the flow rate is increased within the timeframe of the experiments or simulations, which means that more energy is produced at higher flow rates. However, the rock is then also increasingly cooled down which depletes the sample/reservoir around the fracture. In our experimental case, a heat exchange equilibrium was achieved due to heat being resupplied by the furnace. This is however not the case in most natural reservoirs where there is no nearby high heat flux present (the equivalent to an experimental furnace might be a magma chamber or dyke in nature). There is terrestrial heat, but that does not heat up rocks quickly enough to achieve a steady-state heat transfer. Higher flow rates in natural reservoirs therefore result in a quicker propagation of the cold front towards the production well (outlet) instead of an achievement of an equilibrium. High flow rates therefore initially increase the power production, but only as long as the cold front does not reach the production well. Lower flow rates on the other side make the achievement of an equilibrium between the heat sink at the fluid pathway and the local terrestrial heat flux more likely. The graph shown in *Figure 4.3* therefore only applies in case there is a high heat flux present nearby that allows a steady-state heat transfer. Due to the achievement of a stationary condition, time-dependence is not added to *Figure 4.3* which makes it non-comparable to reservoir conditions.
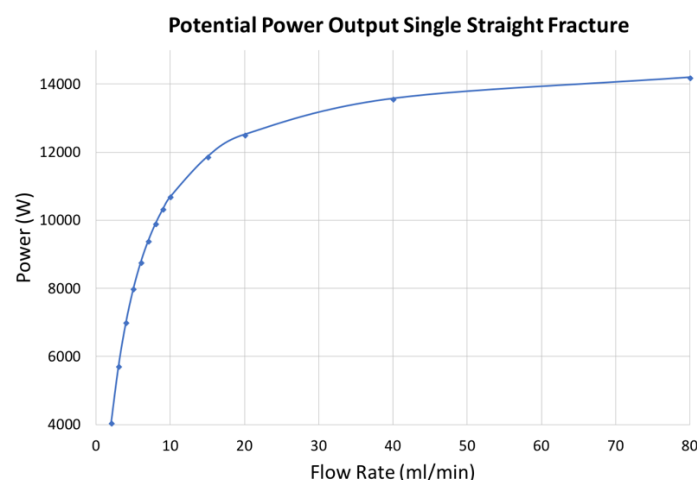
Fig 4.3: Theoretical power output at varying flow rates in the case of a single straight fracture based on the simulation results of Table 8.3 (Appendix).

4.1.2 Fluid Velocity

At a constant fracture aperture and thus fracture volume, the fluid velocity is proportional to the volumetric flow rate. *Equation 17* shows the relationship between flow rate and fluid velocity assuming laminar flow:

$$v_{avg} = Q/A_f \qquad\qquad (Eq.\ 17)$$

where v_{avg} is the average laminar fluid velocity (m/s), Q is the flow rate (m^3/s) and A_f is the cross-sectional fracture area (m^2) (product of fracture aperture and depth/diameter of the sample). As Reynolds Number values in the result section have shown, it is adequate to assume a completely laminar flow along the fractures in the present experiments and simulations conducted. A laminar flow profile is a parabolically shaped curve where the fluid velocity at the walls are zero with the maximum reached in the middle of the flow pathway assuming no-slip conditions at the solid-fluid contact. This characteristic laminar flow profile is depicted in *Figure 4.4* that is generated from one COMSOL simulation with a straight fracture and an imposed average fluid velocity of 0.022 m/s. Therefore, in a perfectly laminar flow case, the majority of the fluid does not come into direct contact with the solid but passes by at higher velocities along the middle of the fluid pathway. However, we can expect that fluid conduction and mixing occurs that transfers a certain amount of heat towards the middle of the fluid pathway as well. It should also be noted that *Figure 4.4* represents a perfectly smooth and straight flow pathway. In natural fractures such as the ones generated in the experiments (*Chapter 3*), the velocity profile almost certainly differs from a perfectly laminar one and small turbulences are expected to occur too. Therefore, generally more mixing of the fluid is expected along natural fractures as compared to a perfectly laminar case. It is difficult to tell whether and to what degree the velocity profile inside the fractures generated during the experiments differs from a laminar profile. The measurement of flow rates during the experiments only represents an average bulk velocity that does not consider varying velocities in different areas of the fracture. We are therefore dependent on assumptions; in general, the flow profile is of laminar kind during the experiments with local turbulences.
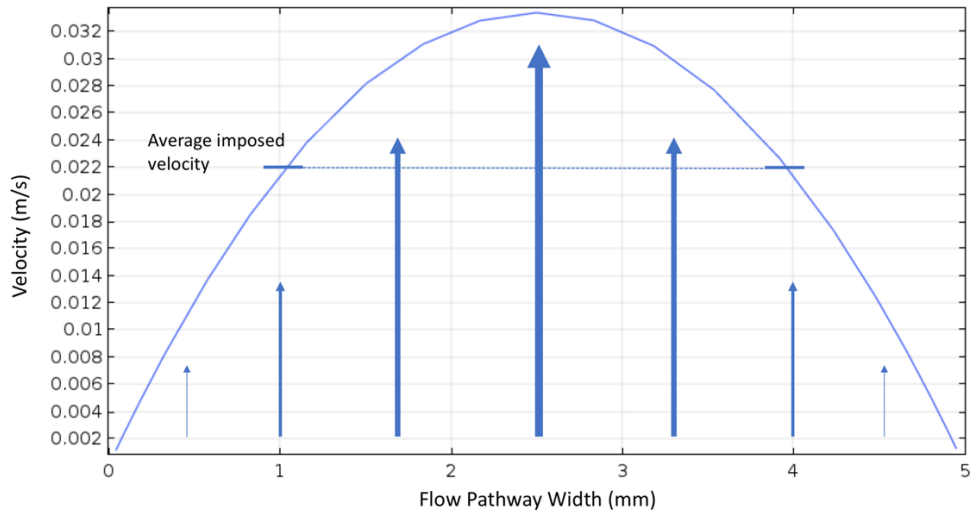
Fig 4.4: Characteristic Laminar Flow Velocity Profile simulated with COMSOL Multiphysics. The flow pathway is 5 mm wide in this case where the fracture walls are at 0 mm and 5 mm width. Maximum fluid velocity is reached at 2.5 mm width.

The volumetric flow rate and the fluid velocity are closely related as shown in *Equation 17* and have an impact on heat transfer between solid and fluid as the fracture aperture is altered. Fracture aperture alterations and its implications on flow rates, fluid velocities and heat transfer will be discussed in more detail in *Chapter 4.1.3*.

4.1.3 Fracture Aperture

It was attempted to find a correlation of varying fracture apertures and resulting heat exchange between solid and fluid. At an experimental scale this was done in Experiments 2 and 6, where the volumetric flow rate was kept constant while manually altering the fracture aperture. No clear trend was observed, the linear trendlines show no unequivocal effect of the varying apertures on fluid temperature variations (see *Figures 3.7* and *3.8*). Similar conditions were simulated in COMSOL Multiphysics; varying fracture apertures while keeping a constant flow rate. As seen in *Figure 3.22*, the temperature difference between inlet and outlet does practically not vary notably. Therefore, the noisy data from Experiments 2 and 6, where trendlines suggest no change in temperature difference could be confirmed with numerical simulations. This result suggests that varying apertures do not cause the heat exchange and produced energy per unit volume to change as long as the volumetric flow rate is kept constant. As depicted in *Figures 3.7* and *3.8*, the average fluid velocity decreases as the aperture is widened at a constant volumetric flow rate. It was covered before that as the fracture void space is increased, it takes more time to replace the entire volume of water inside the fracture at a constant external flow rate. The retention time of the fluid is thus increased which results in a longer heating period of the fluid. At the same time a higher volume of fluid is passing through along the middle of the fluid pathway without being directly heated up by the rock. As hot fluid masses from the fracture walls mix with relatively cooler fluid masses from the middle, the average outlet fluid temperature is still the same

as compared to smaller fracture apertures. The inversion of this case where the fluid velocity was kept constant is also simulated in COMSOL Multiphysics. As expected, the temperature difference between inlet and outlet would now decrease with increasing fracture aperture since the volumetric flow rate is indirectly increased as well.

From the observations in the experiments and from the corresponding model calculations fracture aperture variations in the geothermal reservoir are expected to have a minimal impact on the effective heat production performance, as long as a certain target flow rate can be maintained. Target flow rates could, for example, not be maintained in a low permeability reservoir where high pressure differences would have to be imposed. The volumetric flow rate is therefore the most important parameter in *Equation 17* correlating flow rate, velocity and fracture aperture. Local and average fluid velocities are indirectly altered but do not alone lead to a certain temperature difference between inlet and outlet.

4.1.4 Fracture Surface Area

As presented in *Chapter 3.2*, the generated fractures of each experiment were analyzed with a 3D visualization and analysis software using input data from CT scans and the fracture surface areas were measured. Since the rock-fluid contact and therefore the heat exchange between granite and water occurs on the fracture surface, it is expected that there is a direct correlation between the outlet fluid temperature and the fracture surface area, i.e., a larger fracture surface area leads to more heat exchanged. In the following two plots, a comparison between the results of *Figure 3.3* (depicting ΔT_{out} of fracture Experiments $1 - 6$ in percentage) and the results of *Table 3.5* (listing the fracture surface areas of Experiment $1 - 6$) was established. It is uncertain what fraction of the fracture in Experiment 6 was involved in fluid flow. As mentioned in the results section, the saw-cut part of the fracture network might have been closed due to the confining pressure during the experiment and was thus inaccessible to fluid flow. This assumption would reduce the fracture surface area of Experiment 6 by about 3000 mm^2 to 6500 mm^2.

Discussion
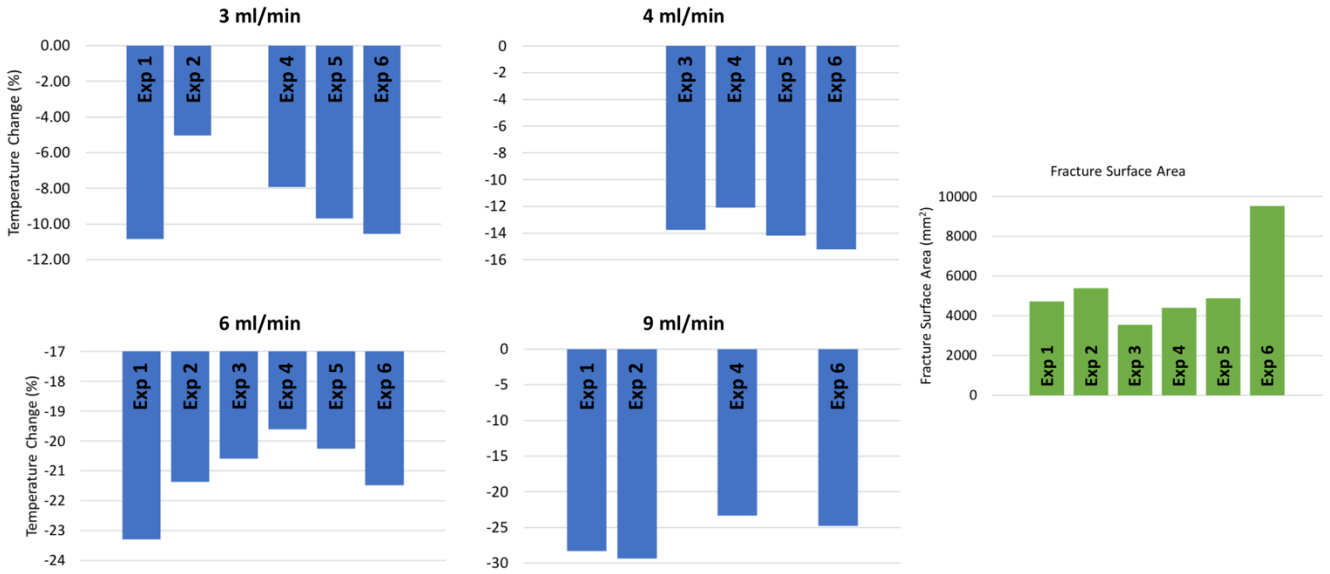
Fig 4.5: ΔT_{out} as a good indicator of heat transfer along the fluid pathway at selected flow rates showing Experiments 1 – 6. Empty fields mean that this particular flow rate was not imposed during the corresponding experiment. The Fracture Surface Area of each Experiment is depicted on the right side with green columns.
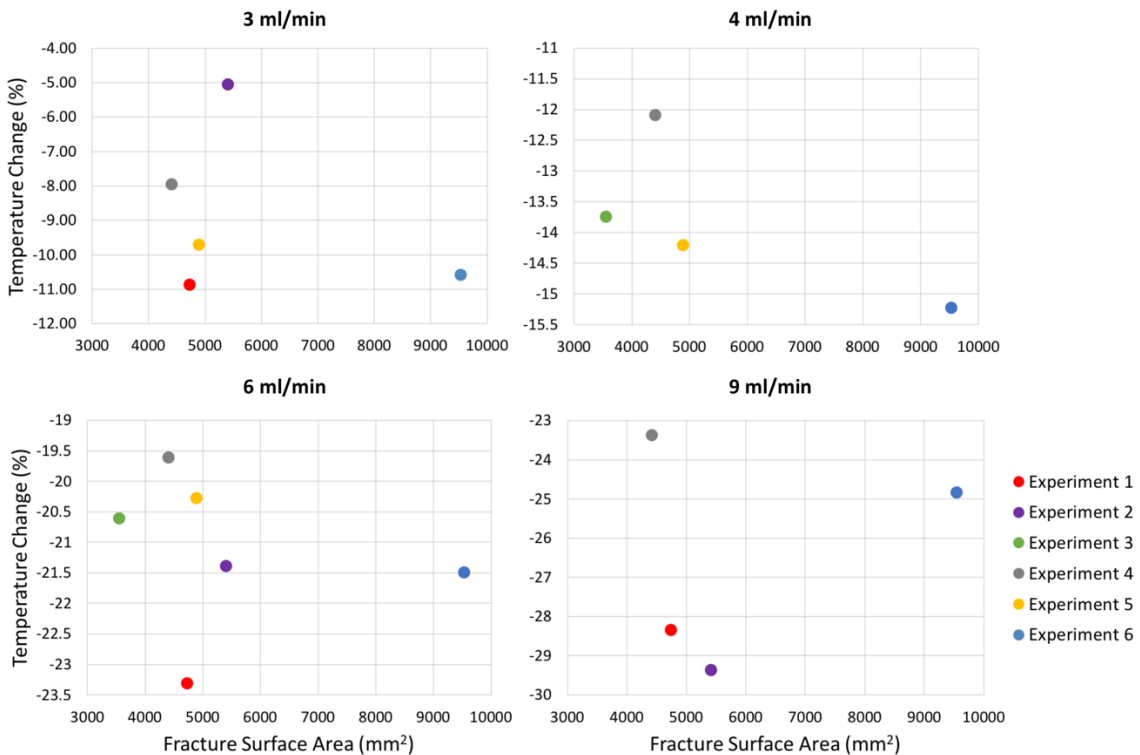
Fig 4.6: Measured Fracture Surface Areas (mm^2) is correlated with ΔT_{out} at several flow rates. Data points represent a specific Experiment as shown in the legend.

A correlation trend between these two parameters cannot be recognized from *Figures 4.5* and *4.6*. The temperature decrease at the outlet in Experiment 1 is generally higher compared to the other experiments. This would suggest less heat extraction of the water and therefore a smaller area where this heat extraction/transfer occurs. However, the fracture surface area in Experiment 1 is not notably smaller

compared to any other experiment except Experiment 6. There are no clear observable trends in the data to suggest a correlation between the two parameters. Also *Figure 4.6,* where the temperature difference is plotted versus the surface area, does not show any clear correlation for the different experiments. The data points are scattered in an almost random pattern and no conclusion can be drawn from these results. It is most probable that in the present experiments, variations in fracture surface area do not affect the amount of heat exchanged between solid and fluid. On the basis of the results found in this project, fracture roughness/topology caused by varying fracture surface areas does not seem to notably influence the observed temperature changes. Flatness values of each fracture measured in Avizo and listed in *Table 3.5* could be a relevant quantification of fracture roughness. Significant variations of Flatness (between 0.015 and 0.985) are found between different experiments, which does not seem to have an impact on heat exchange either. However, fracture roughness and topology can influence the permeability and thereby the achieved flow rates. Nevertheless, this affect is most likely rather small in the present experiments.

Looking at the results of the COMSOL Multiphysics simulations in *Figure 3.24*, it is useful to compare Case 2 with Case 3 to compare different fracture surface areas and their impact on heat exchange. Case 2 includes three nearly straight fractures along the entire sample length. Case 3 also includes three fractures, but two of them have a winding pattern increasing the fracture surface area notably compared to Case 2. However, results of the simulation confirm the experimental findings that an increased fracture surface area does not have an impact on the heat exchange. The temperature distribution in *Figure 3.24* as well as ΔT curves of *Figure 3.25* comparing Cases 2 and 3 are nearly identical and therefore confirms the non-correlation.

Varying surface areas at sample scale do not affect heat exchange. One of the possible explanations may be a conduction-dominated regime. Heat conduction through the rock sample might be the limiting factor for heat transfer between solid and fluid. See *Chapter 4.4* for more elaborate explanations on a conduction-dominated regime.

4.1.5 Fracture Geometry

Varying fracture geometries are closely related to varying fracture surface areas. However, the focus in this subchapter lies on generated side fractures that increase the number of possible fluid pathways across the sample. Not all fractures formed in Experiments 1 – 6 consist of a single fluid pathway. In some experiments side fractures were, unintentionally, generated. It is difficult to quantify side fractures since some of them are non-continuous, not connected to the main fracture or isolated in the rock such that no fluid flow is possible. In this case, only side fractures that are connected to the main fracture and allow fluid flow are counted. Experiments 1, 5 and 6 include side fractures while Experiments 2 – 4 are considered single straight fractures

Discussion

(See *Table 3.5*). Experiments have shown that the temperature decrease at the outlet is generally higher for Experiments 1, 5 and 6 as shown in the column plot of *Figure 4.5*. This suggests that the fluid along the fluid pathway is heated less in these experiments with side fractures as compared to the other experiments with only a single fracture. However, the indication of side fractures having an impact on heat exchange is not very strong in the present experiments. While at a flow rate of 3 ml/min, Experiments 1, 5 and 6 clearly show the highest temperature drops, this trend is not well developed at other flow rates. It should be added that the rock between different fracture branches in the examined samples is rather thin and therefore cools down quickly. These rock sections in between then do not contribute to the heat exchange anymore and all the heat absorbed by the fluid needs to be provided from the sides. The geometry case could then be treated similarly to a single fracture.

In contrast to the experiments, COMSOL simulations show a clearer trend regarding a correlation between heat exchange and number of fluid pathways. Looking at *Figures 3.21* and *3.24*, the temperature distribution inside the sample clearly changes as additional fluid pathways are added. As the fluid flushes through a single fracture, it does not absorb as much heat and generally cools down the rock to a lower temperature at steady-state. As the number of fluid pathways is increased, the water is heated up more and the rock is at a higher average temperature at steady-state flow conditions. This trend can also be seen in *Figure 3.25* where a shift to higher temperature differences is observed as the number of flow pathways is increased. It is most likely that the fluid velocity along the fractures cause a difference in heat exchange as the fracture geometry is altered. As an additional fluid pathway is added to the sample, the fracture volume also doubles and therefore the average fluid velocity would be reduced to half at a constant flow rate. It was discussed previously that lower fluid velocities allow a prolonged contact between solid and fluid and allow a higher heat transfer. Therefore, at a state of a thermal equilibrium the cold front propagates further towards the fluid outlet as fewer fluid pathways are available requiring constant volumetric flow rates.

In order to correlate fracture surface and volume alterations, it is useful to introduce a fracture surface to volume increase ratio that likely has a high impact on heat exchange in geothermal reservoirs. As explained in *Chapter 4.1.3*, fracture aperture variations alone do not seem to cause the heat output to change. Fracture aperture variations are equal to fracture volume variations without changing the fracture surface area. In *Chapter 4.1.4*, it was found that solely fracture surface area variations do not have a notable impact on heat exchange either. However, as we increase the surface area at the same rate as the fracture volume, i.e., adding additional fracture branches with similar aperture, the heat exchange is altered. It is then the lower fluid velocity that allows for an increased heat production. *Chapter 4.3* discusses the surface-volume ratio of fractures in more detail based on results of the axisymmetric COMSOL simulations as well.

4.1.6 Fracture Permeability and Pressure Difference

Figure 3.9 shows the permeability trend based on hydraulic fracture aperture with varying fracture aperture. Generally, the permeability of the fracture increases as the aperture and therefore volume of the fracture becomes higher. The fracture permeability of Experiment 6 is higher than the one of Experiment 2. This can be explained with the sample of Experiment 6 consisting of several fracture branches while the sample of Experiment 2 only contains a single fracture/fluid pathway. As the permeability increases, the pressure difference across the sample (P_{diff}) becomes smaller due to the decreased flow resistance. The Reynolds Number, which determines the flow regime of a fluid, does not vary with changing apertures (within the variation range of present experiments). This can be explained by looking at *Equation 12*. An increasing fracture aperture causes D_h to increase while the velocity u decreases at the same time. One parameter therefore compensates the other. However, in a hypothetical case where the fracture aperture would be very small, very high pressure differences would have to be imposed on the sample in order to achieve a constant flow rate. The fluid velocity within the fracture would then also be very high such that turbulent flow is likely to occur. Turbulent flow could not be achieved in the experiments conducted within this project due to the limitations in pressure difference. A more extensive fracture network that results in higher permeability is favorable to enhance heat exchange as was discussed in *Chapter 4.1.5*.

4.1.7 Rock Temperature

The benchmarking Experiments 8 and 9 were run at identical conditions, except for the target rock temperature. While Experiment 8 was run at 100 °C, Experiment 9 was run at 60 °C. As seen in *Figure 3.10*, temperatures at all measurement locations are higher in Experiment 8 compared to Experiment 9. Consequently, the temperature gradients between different measurement locations are also smaller in Experiment 9: As seen in *Figure 3.12*, the temperature difference between outlet and sample thermocouple is much smaller for Experiment 9 for all flow rates, which also suggests a smaller heat flow through the rock by conduction. Ultimately, the absolute temperature difference between inlet and outlet is also smaller in Experiment 9 compared to Experiment 8. The comparison of these experiments shows that increased rock temperatures increase the heat production of the geothermal system notably. By increasing the rock temperature from 60 °C to 100 °C, the thermal production, i.e., the fluid temperature difference between inlet and outlet can be increased by a factor of roughly 2.5 at all flow rates. For example, ΔT was measured to be 25 °C in Experiment 8 while it is 10 °C in Experiment 9 at a flow rate of 3 ml/min.

4.2 Comparison between Benchmarking and Fracture Experiments

Firstly, the benchmarking Experiment 8 is compared with all fracture experiments. *Figure 4.7* depicts the temperature changes in percentage at the outlet and inlet comparing fracture and benchmarking experiments. Absolute temperature differences between inlet and outlet at a steady-state flow condition are also displayed.
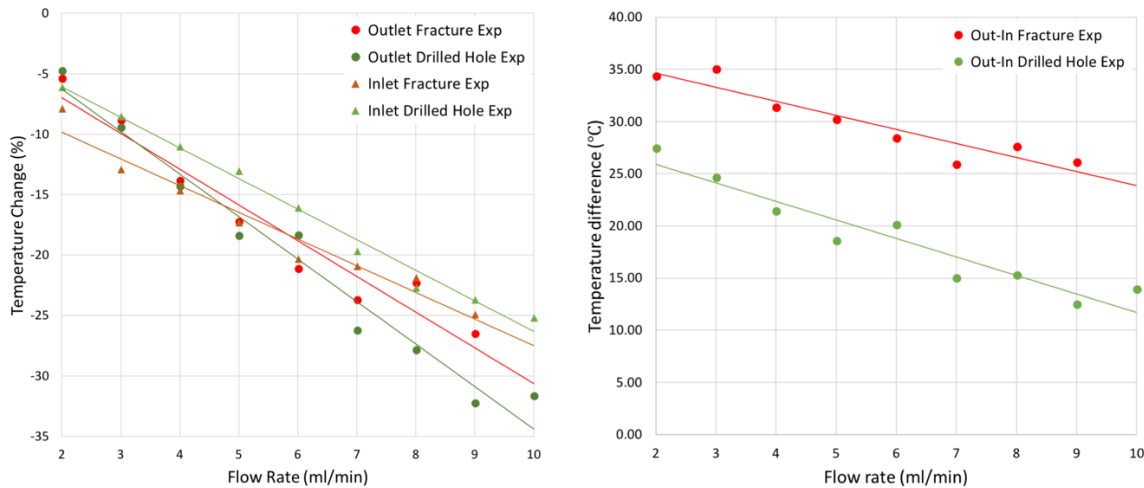
Fig 4.7: Comparison between Fracture Experiments and Drilled Hole Experiment 8. Left side: Temperature change in percentage at the outlet and inlet (ΔT_{out} and ΔT_{in}) for averaged values of Experiment 1-6 and Experiment 8. Right side: Absolute temperature differences between outlet and inlet at steady-state flow for the same data sets as the graphs on the left side.

No major differences are seen for both the inlet temperature changes as well as the outlet temperature changes in percentage. However, different absolute temperature differences between the inlet and outlet comparing the two sets of experiments can be observed. At each flow rate the difference is around 10 °C. However, this difference is explained by initially different temperature conditions. While an average of 100 °C at the outlet and 63 °C at the inlet at no-flow conditions is achieved for the fracture experiments, 97 °C at the outlet and 70 °C at the inlet is achieved for Experiment 8. As mentioned before, absolute temperature differences between inlet and outlet are not largely representative across the conducted experiments.

It is not straight-forward to compare heat transfer along a cylindrical hole with heat transfer along natural fractures due to different geometries. However, the surface area and the volume of the fluid pathways can be analyzed. As seen in *Table 3.5* the fluid pathway surface area of the drilled hole sample is only 742 mm^2, whereas the smallest fracture surface area of Experiment 3 at 3537 mm^2 is still more than 4 times larger than the area of the drilled hole. As for the fluid pathway volume, 668.2 mm^3 were measured for the drilled hole sample. Exact fracture volumes as present during the pressurized experiments cannot be accurately determined. An estimation yields 450 mm^3 assuming an aperture of 0.3 mm, sample length of 50 mm and diameter of 30 mm. Since the fracture aperture varies throughout the experiments, the volume is expected

to vary notably as well. The volumes of both the drilled hole and fractures might therefore lay within the same range. Theoretically, only the surface area varies notably in this comparison. As explained in *Chapter 4.1.4*, surface area variations alone suggest no major impact on heat exchange as can be seen in this comparison of fracture and benchmarking experiments. Of course, due to the small amount of data collected and the non-comparable geometries (rough planar thin fracture versus smooth cylindrical hole), a correlation remains somewhat speculative.

It was initially expected that benchmarking and fracture experiments yield completely different observations in terms of thermal behavior. Apparently, this was not the case and suggests that artificially and naturally formed fluid pathways of any shape might deliver similar temperature results in the present triaxial apparatus.

4.3 Axisymmetric extended model discussion & Area-Volume increase ratio

Initially, a simple modelling geometry was created including only the sample assembly itself without the surrounding oil. By extending the model in size, the heat source (constant temperature boundary) was then moved from the rock sample boundaries to the heating furnace itself, which is expected to represent experimental conditions more accurately. The material between the heating furnace and the rock sample assembly being oil of the type MultiTherm PG-1®, convective heat transfer is expected to dominate over conductive heat transfer. The heating period of the experimental apparatus before any fluid flow is imposed on the rock sample can realistically be simulated. This is essentially interesting to determine the source of the vertical temperature gradient across the sample observed during all experiments. The heating period and the temperatures of all three measurement locations of Experiment 1 are shown in *Figure 4.8*. As a comparison, the temperatures of the COMSOL model displayed in *Figure 3.29* are plotted along with the experimental results.
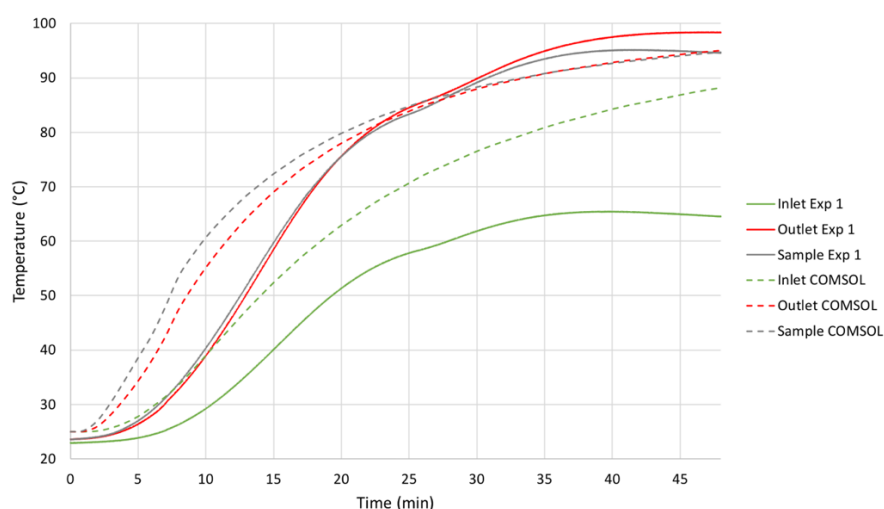
Fig 4.8: First 48 min of the heating period starting at room temperature at the inlet, outlet and sample location. Values of Experiment 1 are displayed as continuous lines and values from the COMSOL simulation (see Figure 3.29) as dashed lines.

Discussion

The heating behavior of the experiment and the simulation is generally quite comparable (see *Figure 4.8*). However, while the temperatures at the outlet and sample reach 90-100 °C already after around 30 min, the heating of the inlet is lagging behind. This can be explained with the temperature-dependent density of the oil causing convection. Since hotter oil has a lower density, it rises to the top of the oil-filled space and gradually starts heating from the top down. This behavior can be seen in *Figure 3.26* and *Figure 3.28*. The inlet location is vertically lower located and thus experiences heating at a later time. While there is initially a significant temperature gradient between the inlet and outlet in the COMSOL model (maximum around 15 °C), it is gradually overcome by reaching an eventual uniform temperature in the entire apparatus. This achievement of a uniform temperature does not occur in the experimental case and the temperature gradient stays at around 33 °C between inlet and outlet in a state of thermal equilibrium. In an altered COMSOL simulation shown in *Figure 3.30* however, a vertical temperature gradient could also be achieved in a state of thermal equilibrium. Random constant heat sink boundary conditions at the top and bottom of the model resulted in such a gradient. The temperature difference between the inlet and outlet is computed to be 5.7 °C (65.8 °C at the inlet and 71.5 °C at the outlet) which is still much smaller than in the experimental case. The reason for the observed vertical temperature gradient during the experiments is most likely a combination of **non-uniform heat influx of the furnace** and considerable **heat sink behavior** within the metal parts that connect the inside of the apparatus to the outside (room temperature). These two reasons are discussed as follows.

- While the furnace in the COMSOL model was set to a uniform temperature, it is likely that the furnace in the experimental case imposes lower temperatures at the bottom and higher temperatures at the top as a result of the oil convection. As the COMSOL model has shown, vertically non-uniform temperatures in a fluid cause convection to occur that is trying to achieve a temperature uniformity. A continuous convective behavior of the oil is therefore likely throughout an entire experiment due to the non-ideal heating pattern of the furnace. The furnace gets a constant electrical power supply, and as the current goes through the wires of the furnace it is converted in to heat due to the resistance of the wire. A different design of the furnace could impose vertically more uniform temperatures. Such a design could consist of three sets of heating coils instead of only one as it is now. Convection is generally a faster heat transfer process than conduction. This was also shown in COMSOL simulations and is illustrated in *Figures 3.26 and 3.27*. While the oil heats up rather quickly and transports the heat downwards in vertical direction, the solid parts of the experimental setup are not yet heated up. One of the main drivers for a vertical temperature gradient within solid material parts is therefore the oil temperature beside it.

- Another reason the vertical temperature gradient cannot be overcome in our experimental case is probably the occurrence of heat sinks at the top and bottom of the apparatus. While there is insulation present on the side of the apparatus, the top and bottom are poorly insulated due to the vertical extent of the axial piston and the load cell which are made of steel, which has a high thermal conductivity. Due to this, heat is most likely lost through the metal parts of the apparatus at the top and bottom. This requires constant heating of the furnace and continuous convection of the oil to resupply the lost heat. Placing insulation material at the top and bottom of the apparatus could reduce heat loss.

Similar to the experiments and the COMSOL 2D simulation, the temperature difference between inlet and outlet is decreasing with increasing flow rates. This goes hand-in-hand with a forward shift of the cold front. This is observed in *Figure 3.33*. As already mentioned in the results, there is a difference in the heat transfer as the hole diameter is altered. This difference is slightly larger compared to a fracture aperture variation in the COMSOL 2D case depicted in *Figure 3.23*, but only at low flow rates. This is most likely due to a surface area and volume increase of the fluid pathway that a diameter increase results in. While a cylindrical fluid pathway experiences both an area and volume increase as the diameter is increased, a cubic fracture fluid pathway only increases its volume at increased apertures while the surface area stays constant. As shown in *Figure 3.24* and *3.28*, a surface area and volume increase at the same time needs to be achieved to have an impact on the heat transfer between solid and fluid. Taking the increase in hole diameter in *Figure 3.31* and *Figure 3.32* as an example, the surface area of the fluid pathway increases at the same rate as the diameter. So, going from 1 mm to 4 mm diameter means a surface area increase by a factor of 4 too. This is based on the area calculation of a cylinder side ($A = 2\pi rh$). However, the volume of the fluid pathway increases by a factor of 4 times higher, so 16 times in this case. This is based on the volume calculation of a cylinder ($V = \pi r^2 h$). The ratio of area increase/volume increase is therefore 1/4 in this case. The ratio of area increase/volume increase in the COMSOL 2D case in *Figure 3.24* as additional fracture branches were added is 1/1. The ratio in case of a fracture aperture variation is always -/x, i.e., there is no change in the surface area (-) while there is a certain change in the fracture volume proportional to the aperture variation (x).

To summarize, a fracture aperture or volume variation alone does not show alterations in heat production (ΔT). An equal change of surface area and volume, e.g., both values are doubled does show significant differences in ΔT while an alteration ratio of 1/4 only shows small differences. It can be suggested that the higher the volume change of a fluid pathway compared to the surface area change is, the lower the difference in heat transfer. On the other side, surface areas were altered while the volume remained relatively constant. This was observed comparing fracture experiments with each other and explained in *Chapter 4.2.* The findings imply that a fracture surface area alteration alone only results in minor impacts on heat exchange.

Discussion

In section **c)** of *Chapter 3.3.3* the results of a sub-experiment that was numerically simulated using the axisymmetric geometry are presented. The goal was to investigate in the cooling behavior of the rock sample and apparatus that occurs during the experiments once a constant fluid flow is imposed. Exponential cooling behavior was found at the outlet and sample location. This is elaborated in more detail in the last part of *Chapter 4.4*. Something that could not be measured during the experiments is represented in *Figure 3.35*; a continuous temperature profile from the inlet to the outlet along the middle of the fluid pathway and how it evolved throughout time. It is clearly seen that the temperature is initially barely increasing along the first 7 mm, i.e., the water is not taking up any heat. Heated water along the pathway walls does initially not reach the middle, so mixing does initially not occur in this case of laminar flow. Through both conductive and convective processes, heating of the fluid furthest away from the fluid pathway walls sets in 8 mm after the inlet location in this case. Initially, heating of the fluid occurs at a high rate and flattens out the closer it gets to the outlet. Heating along the steel part of the assembly occurs at a higher rate before reaching the rock sample. As found in *Table 2.3*, which lists all the properties of the materials used in the experiments, steel is significantly more conductive than granite rock. This suggests that the system is conduction-dominated, i.e., the higher the thermal conductivity of a material the more heat is transferred from solid to fluid. Therefore, the amount of heat that can be extracted is limited by conduction. As we move further in time in *Figure 3.35* the temperature curves become increasingly flatter and reach lower temperatures at the outlet, i.e., the temperature gradient along the sample reduces. This is due to an increasingly colder rock sample with time that does not provide as much heat to the fluid anymore. The increasingly cooler rock can be seen in *Figure 3.36*. As we progress in time, the shape of the temperature profile curves however stays the same. An initially unsteady heat transfer finally reaches a steady state heat transfer as a thermal equilibrium has established, i.e., inward heat flux equals outward heat flux.

4.4 Exponential cooling during sub-experiments – A conduction-dominated regime

Every temperature development observed in the experiments (*Chapter 3.1.4*) could accurately be fit with an exponential cooling/decay curve and expressed by a time-dependent function. The difference between T_0 and T_{end} represents the temperature difference between no-flow and steady-state flow conditions, as explained in *Chapter 2.6.4*. Generally, this difference is the largest at the outlet, followed by the inlet or sample measurement. The highest amount of cooling therefore occurs at the outlet which makes sense considering the temperature gradient along the sample suggesting highest temperatures at the top. T_{end} or the temperature at steady-state flow conditions consistently shows a decreasing trend from sample (hottest) to outlet to inlet (coldest). This is related to the vertical temperature gradient in the apparatus on one side and the proximity to the heat source on the other side. While the outlet thermocouple lies vertically at the highest position in the apparatus, the sample thermocouple is located more closely to the heating furnace. In a state

of thermal equilibrium, a declining temperature trend from the heating furnace to the cooling fluid flow along the fracture is therefore observed.

The exponential cooling functions found for each sub-experiment are correlated to Newton's law of cooling. With the same type of function, Newton's law of cooling states that

$$T(t) = T_{env} + (T_0 - T_{env}) * e^{-rt} \qquad \textit{(Eq. 18)}$$

Where T is the temperature of the object's surface, T_{env} is the temperature of the environment and r is a positive constant characteristic of the system which is expressed as

$$r = {hA}/{C} \qquad \textit{(Eq. 19)}$$

Where h is the heat transfer coefficient (W/m²K), A is the heat transfer surface area (m²) and C is the heat capacity of the system. The parameter r is equivalent to λ (exponential decay constant) in our case. The exponential decay constant determines how quickly a system cools down and therefore defines the shape/slope of the curve. The higher this constant is, the more quickly the system reaches a state of equilibrium. It was found throughout all sub-experiments that λ was highest at the inlet, followed by the outlet and sample. That means that fast cooling occurs at the inlet while the slowest response is recorded at the sample location. This nicely represents the stepwise conductive cooling of the rock where the cold front starts at the bottom and propagates towards the top and side of the sample. This is also shown in COMSOL simulations (see, e.g., *Figure 3.21*). The inlet and outlet temperatures both represent the fluid temperature. However, a cooling behavior that is exponential suggests that these fluid temperatures are closely related to the decreasing rock temperature. The heat transfer inside the rock is governed by conduction. According to results in *Tables 3.1 − 3.3, the* λ values at the outlet and sample are fairly consistent across experiments as well as across sub-experiments with varying flow rates within Experiment 6 and 8. According to *Equation 19, constant r (or* λ *in our case)* values suggest a constant heat transfer coefficient which in turn depends on the heat flux, i.e., thermal power per unit area. The heat flux through the experimental apparatus is governed by convection in the pressurized oil. Since sample temperature variations are much smaller compared to inlet and outlet, a nearly constant temperature boundary is located at the oil-jacket interface. Conduction in the rock sample is therefore fairly constant over a large range of sub-experiments. Even if high rates of heat transfer are required due to high flow rates or large differences between fluid and solid temperatures, constant heat conduction in the solid limits the process. The heat (power integrated over time) taken up by the fluid flowing along the fracture is therefore highly dependent and limited by the conductive heat flux in the rock. While at the outlet and sample location, no clear trend of λ between sub-experiments is observable, λ shows an increasing trend with increasing flow rates at the inlet (see *Tables 3.2* and *3.3*). Since inlet cooling does not depend on the interaction of materials within the system as much as at the outlet and sample (due to a fluid injected from the outside), cooling behavior cannot be attributed to conductive heat transfer.

Discussion

The amount of heat that a fluid flowing through a rock absorbs therefore highly depends on how quickly the surrounding rock can recharge lost heat by means of conduction. In the present experiments a state of thermal equilibrium is reached (steady-state heat transfer), i.e., the heat supply governed by conduction through the rock equals the heat withdrawn by fluid along the fracture. Even at different flow rates, the rock cools down at the same rate governed by the conduction in the rock, but the end temperatures at equilibrium are different (see *Chapter 3.1.4*). These equilibrium temperatures at steady-state flow define how far the cold front has propagated. The cold front is, e.g., moving closer to the heat source at higher flow rates.

In section **c)** *Chapter 3.3.3* exponential cooling in time-dependent numerical simulations was identified as well. As *Figure 3.37* shows, exponential fitting curves were computed notably accurately. These numerical findings can be compared with the cooling behavior of Experiment 8 since the geometry of the fluid pathway matches with the one in the axisymmetric model (cylindrical fluid pathway of 4 mm diameter). The simulation case shows higher temperature drops both at the outlet and the sample as compared to the experimental case. The reason for this is mostly likely the higher initial temperature conditions in the simulations where no heat sinks are applied. A steady-state flow condition (thermal equilibrium) is achieved after approximately 10-20 min which is comparable to the experiments. The exponential decay constant λ is very similar in the experimental and numerical case. It was found to be 0.00686 (experimental) and 0.0059 (numerical) at the outlet and 0.00344 (experimental) and 0.0034 (numerical) at the sample. This finding suggests that heat transfer and conductive behavior in the numerical simulations are fairly accurately representing experimental conditions.

4.5 Answers to research questions

In the beginning of this project, three research questions were formulated (see *Chapter 1*). All these research questions could successfully be answered in the course of this project. Answers are found both in the results and discussion sections. This subchapter serves to coherently summarize the answers to the research questions and where they are found. First of all, flow rates and fluid velocities along a fracture do change the amount of heat exchanged between fluid and solid. Generally, the higher the flow rate/fluid velocity, the less heat is taken up by a certain unit volume of fluid and the more extensively the adjacent rock cools down due to higher temperature differences between rock and fluid. This trend is represented in *Chapter 3.1.1* in *Figures 3.3 – 3.6* found in the experiments. The same conclusion was drawn in numerical simulations depicting the trend in *Figures 3.18 – 3.21 of the 2D model* and in *Figures 3.24, 3.25, 3.31, 3.32* and *3.33* of the 2D axisymmetric model. The impact of flow rate on heat exchange is also extensively discussed in *Chapter 4.1.1*.

Another research question is what effect different fracture geometries/surface areas have on the heat exchange. In *Chapter 3.2* the individual fracture geometries and surface areas of each experiment were analyzed. Surface areas and temperature changes were correlated and discussed in *Chapter 4.1.4*. Such correlations are illustrated in *Figures 4.5 – 4.6.* It was suggested that varying surface areas do not have a notable impact on heat exchange within the present experimental scale. This was also confirmed in numerical simulations by comparing Case 2 and 3 in *Figures 3.24 – 3.25* where no notable differences in heat transfer behavior were observed. A varying number of fracture branches were numerically simulated and illustrated in *Figures 3.21, 3.24* and *3.25*. It was found that the more fracture branches are added, the more heat can be extracted and the less the adjacent rock cools down. This is also discussed in *Chapter 4.1.5*.

The third research question is dealing with fracture aperture/fluid pathway width and how their variation has an impact on heat exchange. Experimental findings are suggesting that fracture aperture variations (range between 0.05 and 0.5 mm) do not impact heat exchange at a constant volumetric flow rate as seen in *Figures 3.7 – 3.8.* These findings were confirmed with the help of numerical simulations depicted in *Figure 3.22.* Constant fluid velocities however do change the amount of heat exchanged at varying apertures as *Figures 3.22 – 3.23* confirm. This is discussed in *Chapter 4.1.3*. A ratio of fracture area increase/volume increase was introduced in *Chapter 4.3* which states that surface area changes or volume changes alone do not have a notable effect on heat exchange.

4.6 Comparison with existing literature

The experimental procedures in this project are rather unique. No publication was found that deals with heat exchange in tensile fractures while varying parameters such as flow rate or fracture aperture. As mentioned in *Chapter 1*, Luo et al. (2017) conducted experiments on similar fractured rock types under temperature conditions. However, in that study, the rock samples were fractured prior to loading into the apparatus using the Brazilian splitting method which made mechanical fracture aperture variations during the experiments impossible. Fracture aperture variations were registered by controlling the confining pressure. Furthermore, in the tests conducted by Luo et al. the aperture is much smaller (μm) compared to the present thesis (mm). Rock temperatures were varied similar to Experiments 8 and 9 in this project. Similar rates of thermal efficiency increase from 60 °C to 100 °C were found. Area ratios of fractures were determined to evaluate fracture roughness. Similar to this thesis project, it was found that variations in fracture roughness/topology do not show significant impacts on heat exchange. *Figure 4.9* depicts the improvement of heat transfer with increased rock temperatures in the study of Luo et al. (2017). Additionally, similar values of specific thermal exchange rates can be identified between examined samples #4, #5 and #6 despite their non-identical area ratios.
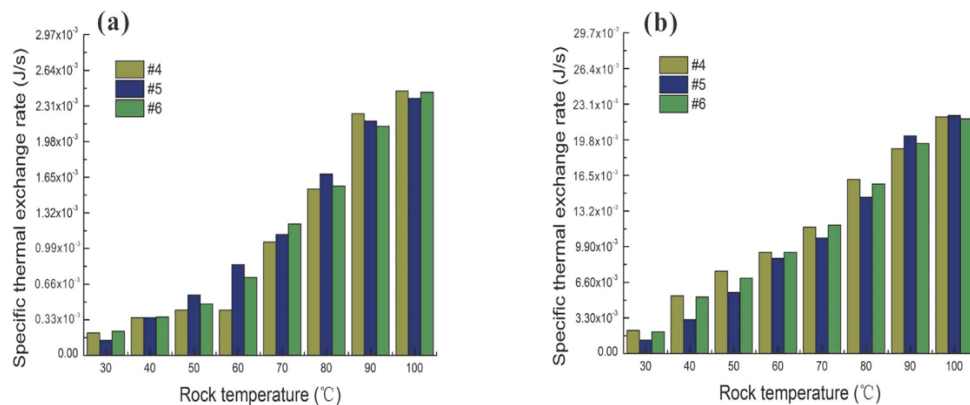
Fig 4.9: Specific thermal exchange rates at different rock temperature. Examined sample #4, #5 and #6 have area ratios of 4.394, 3.818 and 4.341. Experimental conditions of panel (a) are 0.1 MPa hydraulic pressure 8 MPa confining pressure and of panel (b) 0.9 MPa hydraulic pressure and 8 MPa confining pressure. Results and figure according to Luo et al. (2017).

Most other studies about flow through fractured rocks do not include a temperature component. They primarily focus on parameters such as permeability, transmissivity, and hydraulic conductivity of rock fractures at sample scale such as the studies of Kluge et al. (2017), Hofmann et al. (2016), Zimmerman and Bodvarsson (1996) and Milsch et al. (2016).

4.7 Implications on EGS (upscaling)

Investigations within this project were limited to sample scale for both the experiments and the numerical simulations. However, the findings could serve to better understand and improve the development of large-scale geothermal reservoirs. This sub-chapter attempts to state similarities and differences between the project investigations and natural large-scale conditions. It also attempts to hypothetically upscale experimental and numerical results into reservoir-scale.

As partly discussed in *Chapter 4.1.1* heating conditions in geothermal reservoirs differ from the experiments. On the laboratory scale, a steady-state heat transfer was achieved in all experiments where a thermal equilibrium was reached. This equilibrium suggests no thermal depletion of the sample-size thermal reservoir even over a long period of time, i.e., heat is available indefinitely. A constant temperature boundary in the experiments (furnace) is located relatively close to the heat withdrawing location (fluid pathway). However, geothermal reservoirs in the scale of kilometers do not have a constant temperature boundary in proximity to the heat withdrawing location in most cases. The closest constant temperature boundary in the subsurface is the lithosphere-asthenosphere boundary at a depth of roughly 100 km (Plomerová et al., 2002). This is much deeper than the deepest geothermal reservoir. Therefore, resupply of heat towards the fracture network occurs by conduction only. Conduction is a relatively slow process that might not reheat an EGS within its lifetime of less than 100 years. Unsteady heat transfer causes the cold front to propagate towards the outlet location over time which eventually results in decreasing outlet/production fluid temperatures. Also, since fluids reside in EGS much longer than they reside in the rock sample during experiments, fluid temperatures in geothermal reservoirs are probably (nearly) equal to the adjacent rock temperature. Thus, increased flow rates in reservoirs do not directly result in decreasing outlet temperatures but rather cause the cold front to propagate towards the outlet more rapidly.

As discussions in *Chapter 4.1.5* more extensive fracture networks with additional branches result in higher temperature differences between inlet and outlet (higher heat production) and less cooling of the rock sample. This behavior is expected in an EGS as well, so that the cold front propagates more slowly as a more extensive fracture network is generated. This is in general favorable and increases the lifetime of a reservoir. It was found that fracture surface area and fracture aperture variations in the experiments and numerical simulations do not influence the heat exchange. This is probably also the case in EGS, where a conduction-dominated regime governs how much heat could possibly be transferred from the rock to the fluid. It is more important to maintain a certain permeability in the reservoir that is closely related to the fracture aperture. Higher fracture apertures result in higher permeability and therefore less flow resistance across the reservoir.

Less flow resistance in turn means smaller pressure differences that was shown in *Figure 3.9*. Smaller pressure differences in EGS mostly require reduced pump power to inject fluids which is favorable.

4.8 Suggestions for future research

- A time dependence component could be added to the experiments conducted within this project. That means, similar to a geothermal reservoir, the apparatus/rock is initially heated up to a certain target temperature. Once a thermal equilibrium is achieved, any heating source is turned off and a constant fluid flow is imposed on the rock. Unlike in the experiments of this project, a steady-state heat transfer is then not achieved. The system rather cools down at a certain rate (unsteady heat transfer) until it is completely depleted and no more heat can be produced. This could be conducted at different flow rates and serve to determine "lifetimes" of the system.

- It could be favorable to investigate the heat sink behavior as well as the non-uniform heating of the furnace inside the experimental apparatus by means of sophisticated numerical models. Existing models could be enhanced to match the exact heating behavior observed during the experiments. This would serve as an accurate tool to consistently back-test experiments conducted on this specific apparatus (involving a temperature component) with numerical models.

- As mentioned in the project, an experiment with a sample cut apart to provide a perfectly smooth and straight planar "fracture" was not conducted due to one failed setup and time-constraints. This however would be a valuable addition to provide further insights into the difference between natural fractures and straight fractures. It would probably serve as another confirmation that individual fracture geometries do not have a notable impact on heat exchange.

- Experiments within this project were consistently exposed to a vertical temperature gradient inside the apparatus. This made the interpretation of results somewhat difficult and somewhat ambiguous. Future experiments could be conducted that a uniform temperature in the entire vessel is established. This might be possible by either modifying the existing triaxial apparatus by replacing the furnace and insulating the heat sinks or conducting similar experiments in a different apparatus.

- The research could be continued on other rock samples by incorporating fractured or non-fractured porous specimens such as sandstone. This could show whether findings in this project are applicable in other types of geothermal reservoirs.

5. Conclusions

Several research questions have been answered throughout the course of this thesis project. The main goal was to investigate in heat exchange processes as they occur in deep fractured geothermal reservoirs. Several parameters were therefore varied in experiments and numerical models such as volumetric flow rates, fracture aperture, surface area and fracture geometries in order to investigate their impact on heat exchange. To conclude, the experimental results were useful but difficult to interpret mainly due to the large temperature gradient observed in vertical direction. On one hand, it was confirmed that increasing flow rates decrease the heat exchanged per unit volume fluid due to a smaller retention time and increased cooling of the rock. On the other hand, experiments did not show evidence of varying fracture surface areas and geometries having an impact on the heat transfer. Variations of average fluid velocities which are proportional to flow rates at constant cross-sectional areas of fluid pathways are shown to have a high impact on heat transfer. Even though temperature differences between inlet and outlet decrease with increasing fluid velocities, the potential power output of the "geothermal reservoir" is still increasing. This however is only the case if the surrounding rock can efficiently recharge its lost heat through conduction. This brings us to the point that most of the heat transfer along the fracture is limited by heat conduction occurring within the rock. High flow rates are more likely to thermally deplete a reservoir than low flow rates. Both experiments and numerical simulations have shown that variations in fracture aperture do not have an impact on the heat production within the investigated range. This brings us to a ratio of fracture surface area versus fracture volume increase. The more this ratio is favoring a volume increase (e.g., if the fracture aperture is increased, only the fracture volume becomes larger and not the surface area) of the fluid pathway, the less impact there is on the heat transfer as the fracture size is altered. It was found in COMSOL simulations that the highest impacts on heat transfer are observed when the fracture surface area is increased at the same rate as the volume (ratio of 1/1), which indicates additional fracture branches in most cases and therefore a more extensive fracture network. It was also found that the rock permeability of an otherwise impermeable rock is closely related to the fracture aperture. Due to this close relation, it can be concluded that varying permeabilities do not have a significant impact on heat exchange. It was however proven in Experiment 8 and 9 that increased average rock temperatures do rise the heat production significantly at comparable fluid flow rates. The experiments conducted within this project are considered rather unique and incomparable to existing literature. It was also found that several outcomes from this project can be upscaled and applied to reservoir-scale.

6. Acknowledgments

7. References

Arslan, U., Huber, H. (2013) *Characterization of heat transport processes in geothermal systems. International Journal of Low-Carbon Technologies 8, pp 71-79.*

Bendall, B., Huddlestone-Holmes, C., Goldstein, B. (2013) *The current status of geothermal projects in Australia – A national review. Thirty-Eighth Workshop on Geothermal Reservoir Engineering.*

Brown, D.W., Duchane, D.V., Heiken, G., Hriscu, V.Th. (2012) *Mining the Earth's Heat: Hot Dry Rock Geothermal Energy. Chapter 2, pp 17-40.*

Covert, T., Greenstone, M., Knittel, C.R. (2016) *Will we ever stop using fossil fuels? Journal of Economic Perspectives, pp 117-138.*

Darcy, H. (1856) *Les fontaines publiques de la ville de Dijon.*

Day, M. A. (1990) *The No-Slip Condition of Fluid Dynamics. Volume 33, pp 285-296.*

Dye, S. T. (2012) *Geoneutrinos and the radioactive power of the earth. Review of Geophysics 8.*

Fridleifsson, I.B, Bertani, R., Huenges, E., Lund, J.W., Ragnarsson, A., Rybach, L. (2008) *The possible role and contribution of geothermal energy to the mitigation of climate change. IPCC Scoping Meeting on Renewable Energy Sources, pp 59-80.*

Glassley, W.E. (2014) *Renewable Energy and the Environment. 2nd Edition.*

Goldstein, B., Hiriart, G., Bertani, R., Bromley, C., Gutierrez-Negrin, L., Huenges, E., Muraoka, H., Ragnarsson, A., Tester, J., Zui, V., Blackwell, D., Demayo, T., Heath, G., Lee, A., Lund, J.W., Mongillo, M., Newell, D., Sanyal, S., Williamson, K.H., Wyborne, D., Zemedkun, M.T., Wratt, D. (2011) *Renewable Energy Sources and Climate Change Mitigation; Special Report of the Intergovernmental Panel on Climate Change. pp 401-436.*

Golewski, G.L. (2017) *Generalized Fracture Toughness and Compressive Strength of Sustainable Concrete Including Low Calcium Fly Ash. Materials 10.*

Hao, Y., Fu, P., Johnson, S.M., Carrigan, C.R. (2012) *Numerical Studies of Coupled Flow and Heat Transfer Processes in Hydraulically Fractured Geothermal Reservoirs. GRC Transactions 36, pp 453-458.*

Hofmann, H., Blöcher, G., Milsch, H., Babadagli, T., Zimmermann, G. (2016) *Transmissivity of aligned and displaced tensile fractures in granitic rocks during cyclic loading. International Journal of Rock Mechanics & Mining Sciences 87, pp 69-84.*

Huenges, E. (2016) *Enhanced geothermal systems: review and status of research and development. Geothermal Power Generation, pp 743-761.*

Jaeger, J.C, Hoskins, E.R. (1966) *Rock Failure under the Confined Brazilian Test. Journal of Geophysical Research 71, pp 2651-2659.*

Kell, G.S. (1975) *Density, Thermal Expansivity, and Compressibility of Liquid Water from 0° to 150 °C: Correlations and Tables for Atmospheric Pressure and Saturation Reviewed and Expressed on 1968 Temperature Scale. Journal of Chemical and Engineering Data 20, pp 97-105.*

Khoshnaw, F., Jaf, P., Farkha, S. (2015) *Pore, Abnormal Formation and Fracture Pressures Prediction. International Journal of Engineering Technology Science and Research 2, pp 51-59.*

Kissling, W.M., Ellis, S.E., McNamara, D., Massiot, C. (2015) *Modelling fluid flow through fractured rock: Examples using TVZ geothermal reservoirs. Proceedings 37th New Zealand Geothermal Workshop.*

Kluge, C., Milsch, H., Blöcher, G. (2017) *Permeability of displaced fractures. Energy Procedia.*

Kolditz, O. (1995) *Modelling Flow and Heat Transfer in Fractured Rock, Geothermics 24, pp 451-470.*

Lund, J.W., Bjelm, L., Bloomquist, G., Mortensen, A.K. (2008) *Characteristics, development and utilization of geothermal resources – a Nordic perspective. Episodes 31, pp 140-147.*

References

Lund, J.W., Freeston, D.H., Boyd, T.L. (2005) *Direct application of geothermal energy: 2005 Worldwide review. Geothermics 34, pp 691-727.*

Luo, J., Zhu, Y., Guo, Q., Tan, L., Zhuang, Y., Liu, M., Zhang, C., Xiang, W., Rohn, J. (2017) *Experimental investigation of the hydraulic and heat-transfer properties of artificially fractured granite. Scientific Reports 7.*

Milsch, H., Hofmann, H., Blöcher, G. (2016) *An experimental and numerical evaluation of continuous fracture permeability measurements during effective pressure cycles. International Journal of Rock Mechanics & Mining Sciences 89, pp 109-115.*

Moore, J.N., Simmons, S.F. (2013) *More Power from Below. Science 340, pp 933-934.*

Multitherm LLC. (2018) *https://www.multitherm.com as of July 2018.*

National Institute of Standards and Technology (NIST), U.S. Department of Commerce (2018) *https://www.nist.gov as of July 2018.*

Olasolo, P., Juárez, M.C., Morales, M.P., D'Amico, S., Liarte, I.A. (2015) *Enhanced geothermal systems (EGS): A review. Renewable and Sustainable Energy Reviews 56, pp 133-144.*

Paterson, M.S. and Wong, T. (2005) *Experimental Rock Deformation - The Brittle Field. Second Edition.*

Patil, M.P, Yadav, A.P., Patil, P.A. (2015) *Comparative Study between Heat Transfer through Laminar Flow and Turbulent Flow. International Journal of Innovative Research in Science, Engineering and Technology 4, pp 2223-2226.*

Plomerová, J., Kouba, D., Babuška, V. (2002) *Mapping the lithosphere-asthenosphere boundary through changes in surface-wave anisotropy. Tectonophysics 358, pp 175-185.*

Reynolds, O. (1883) *An Experimental Investigation of the Circumstances which determine whether the Motion of Water shall be Direct or Sinuous, and of the Law of Resistance in Parallel Channels. Philosophical Transactions of the Royal Society of London 174, pp 935-982.*

Schlichting, H., Gersten, K. (2017) *Boundary-Layer Theory. Ninth Edition, pp 416-419.*

Selvadurai, A.P.S., Boulon, M.J., Nguyen, T.S. (2005) *The Permeability of an Intact Granite. Pure and Applied Geophysics 162, pp 373-407.*

Stober, I. (2011) *Depth- and pressure-dependent permeability in the upper continental crust: data from the Urach 3 geothermal borehole, southwest Germany. Hydrogeology Journal 19, pp 685-699.*

Vik, H.S., Salimzadeh, S., Nick, H.M. (2018) *Heat recovery from multiple-fracture enhanced geothermal systems: The effect of thermoelastic fracture interactions. Renewable Energy 121, pp 606-622.*

Walsh, J.B. (1981) *Effect of Pore Pressure and Confining Pressure on Fracture Permeability. International Journal of Rock Mechanics and Mining Sciences & Geomechanics Abstracts 18, pp 429-435.*

WEC (2013) *Survey of energy resources. London: World Energy Council. pp 352-413.*

Wendl, M. (2015) *Theoretical Foundations of Conduction and Convection Heat Transfer.*

Willems, C.J.L., Nick, H.M., Weltje, G.J., Bruhn, D.F. (2017) *An evaluation of interferences in heat production from low enthalpy geothermal doublet systems. Energy 135, pp 500-512.*

Witherspoon, P. A., Wang, J. S., Iwai, K., and Gale, J. E. (1980) *Validity of cubic law for fluid flow in a deformable rock fracture. Water Resources Research 16, pp 1016–1024.*

Wright, M. (1989) *Nature of Geothermal Resources. Geothermal Direct Use Engineering and Design Guidebook Chapter 3, pp 23–54.*

Zimmerman, R.W., Bodvarsson, G.S. (1996) *Hydraulic Conductivity of Rock Fractures. Transport in Porous Media 23, pp 1-30.*

8. Appendix

8.1 MATLAB Scripts

Chapter 2.6 mentions MATLAB scripts used to analyze and calculate experimental data.

Script 1 documented is used to convert experimental data written on a .txt file into a .mat file. It also plots experimental data and allows to select specific time ranges to plot and to save in another .mat file.

```matlab
%% TerratekData General Plot Script - Dr. Richard Bakker, modified by Marco Balmer
close all
clear all
lw       = 2; % linewidth
% sample parameters
diameter  = 29.30;  %in mm
length   = 49.2;
%% read in new data file (.log, not converted to .mat yet)
B = importdata('Experiment01.txt','\t');
   % data read as one string per line
tmp = strsplit(B{1},'\t');
   % temporary split of string to determine number of data columns
A  = zeros(numel(B),size(tmp,2)-2);
DT = cell(numel(B),2);
   % initiate table A for all data
for n=1:numel(B)
C        = strsplit(B{n},'\t'); % temporary variable C with data per line
A(n,:)  = str2double(C(1:27)); % convert substrings to numbers and write to A
DT(n,:) = C(28:29);           % writes timestamps to DT as strings
end
% assign sample sensor arrays
time   = A(:,1);        % elapsed time since start of file [sec]
PC     = A(:,2);        % cell pressure (confining pressure) [bar]
load   = A(:,11);       % axial load [kN]
lvdt1  = A(:,13);       % displacement sensor 1 [mm]
lvdt2  = A(:,14);       % displacement sensor 2 [mm]
extn   = A(:,12);       % extensometer (chain lvdt) [mm]
temp   = A(:,17:20);    % temperatures 1:4 (nx4 data) [degC]
% assign oil pump data arrays:
Prad_SP = A(:,3);        % radial pressure setpoint [bar] (before pressure intensifier)
Prad_PV = A(:,4);        % radial pressure pointvalue [bar] (before pressure intensifier)
Pax_SP = A(:,5);         % axial pressure setpoint [bar] (before piston, inside enerpac)
Pax_PV = A(:,6);         % axial pressure pointvalue [bar] (before piston, inside enerpac)
% assign pore pressure pump arrays:
QpA     = A(:,22);      % flow rate pump A [mL/min]
QpB     = A(:,25);      % flow rate pump B [mL/min]
VpA     = A(:,23);      % volume   pump A [mL]
VpB     = A(:,26);      % volume   pump B [mL]
PpA     = A(:,24);      % pressure  pump A [bar]
PpB     = A(:,27);      % pressure  pump B [bar]
% % assign pore pressure difference array
Pdiff   = A(:,7);       % pressure difference [bar]
%% save variables (optional)
filename = 'Experiment01.mat';
save(filename,'time','PC','load','lvdt1','lvdt2','extn',...
             'Prad_SP','Prad_PV','Pax_SP','Pax_PV',...
             'QpA','QpB','VpA','VpB','PpA','PpB',...
             'DT','temp','Pdiff')
%% load variables from .mat file (if file once before processed)
filename = 'Experiment01.mat';
load(filename);
```

Appendix

```matlab
%% plotting raw data (complete file)
% setup figure
figure(2)   = figure('position',[100 100 1000 1000]); % figure size in pixels
hax2(1) = axes('position',[0.07 0.050 0.9 0.12]);  % axes window 1 in normalized
hax2(2) = axes('position',[0.07 0.225 0.9 0.12]);  % axes window 2 in normalized
hax2(3) = axes('position',[0.07 0.375 0.9 0.12]);  % axes window 3 in normalized
hax2(4) = axes('position',[0.07 0.525 0.9 0.12]);  % axes window 4 in normalized
hax2(5) = axes('position',[0.07 0.675 0.9 0.12]);  % axes window 4 in normalized
hax2(6) = axes('position',[0.07 0.825 0.9 0.15]);  % axes window 4 in normalized
deltaT = (temp(:,3)) - (temp(:,4)); %Temperature difference between Inlet and Outlet
% plot all data
time_min = time/60; %Convert time from seconds to minutes
hp21 = plot(hax2(1),time_min,load,'LineWidth',1.5);
hp22 = plot(hax2(2),time_min,extn,'LineWidth',1.5);
hp23 = plot(hax2(3),time_min,QpA,time_min,QpB,'LineWidth',1.5);
hp24 = plot(hax2(4),time_min,Pdiff);
hp25 = plot(hax2(5),time_min,deltaT,'LineWidth',1.5);
hp26 = plot(hax2(6),time_min,temp(:,2),...
                time_min,temp(:,3),...
                time_min,temp(:,4),'LineWidth',1.5);
%% making stuff look fancy
set(get(hax2(1),'Ylabel'),'String','Load (kN)')
set(get(hax2(2),'Ylabel'),'String','Extn (mm)')
set(hax2(2),'XTickLabel',[])
set(get(hax2(3),'Ylabel'),'String','Flowrate (ml/min)')
set(hax2(3),'XTickLabel',[])
set(get(hax2(4),'Ylabel'),'String','Pdiff (bar)')
set(hax2(4),'XTickLabel',[])
set(get(hax2(5),'Ylabel'),'String','\DeltaT ({\circ}C)')
set(hax2(5),'XTickLabel',[])
set(get(hax2(6),'Ylabel'),'String','Temp ({\circ}C)')
set(hax2(6),'XTickLabel',[])
set(get(hax2(1),'Xlabel'),'String','time (min)')
set(hax2,'Xgrid','on','Ygrid','on')
set(hax2,'FontSize',12,'FontWeight','bold')
%% define data window example
%Display data only within a defined time range
tmp2 = ginput(2);
[~,ind21] = min(abs(time-tmp2(1,1)));
[~,ind22] = min(abs(time-tmp2(2,1)));
rng2 = [ind21:ind22];
% rng gives all indices between the two points (in time) defined by g-input
% useful for analysing part of the experiment.
time_min = (time(rng2)-time(ind21))/60;
% example:
% show all data within the range:
hp21 = plot(hax2(1),time_min,load(rng2),'LineWidth',1.5);
hp22 = plot(hax2(2),time_min,extn(rng2),'LineWidth',1.5);
hp23 = plot(hax2(3),time_min,QpA(rng2),time(rng2),QpB(rng2),'LineWidth',1.5);
hp24 = plot(hax2(4),time_min,Pdiff(rng2));
hp25 = plot(hax2(5),time_min,deltaT(rng2),'LineWidth',1.5);
hp26 = plot(hax2(6),time_min,temp(rng2,2),...
                time_min,temp(rng2,3),...
                time_min,temp(rng2,4),'LineWidth',2);
set(get(hax2(1),'Ylabel'),'String','Load (kN)')
set(get(hax2(2),'Ylabel'),'String','Extn (mm)')
set(hax2(2),'XTickLabel',[])
set(get(hax2(3),'Ylabel'),'String','Flowrate (ml/min)')
set(hax2(3),'XTickLabel',[])
set(get(hax2(4),'Ylabel'),'String','Pdiff (bar)')
set(hax2(4),'XTickLabel',[])
set(get(hax2(5),'Ylabel'),'String','\DeltaT ({\circ}C)')
set(hax2(5),'XTickLabel',[])
set(get(hax2(6),'Ylabel'),'String','Temp ({\circ}C)')
set(hax2(6),'XTickLabel',[])
```

```matlab
set(get(hax2(1),'Xlabel'),'String','time (min)')
set(hax2,'Xgrid','on','Ygrid','on')
set(hax2,'FontSize',12,'FontWeight','bold')
%% Select a time point to write data at this time
%At selected time point parameter values will be saved
%Useful to analyse specific parameters at specific time points
[x,y] = ginput(1);
[c1 index1] = min(abs(time-x));  %find best match in the time vector
time1 = time(index1);
temp_out1 = temp(index1,3);  %write corresponding outflow temperature
temp_in1 = temp(index1,4);  %write corresponding inflow temperature
temp_sample1 = temp(index1,2); %write corresponding sample temperature
deltaT1 = deltaT(index1); %write corresponding temperature difference
extn1 = extn(index1); %extensometer
Pdiff1 = Pdiff(index1); %differential pressure
QpA1 = QpA(index1); %flow rate pump A
QpB1 = QpB(index1); %flow rate pump B
load1 = load(index1);
%% Select second time point for averaging a range
% At a second selected time point parameter values will be saved
[a,b] = ginput(1);
[c2 index2] = min(abs(time-a));  %find best match in the time vector
time2 = time(index2);
temp_out2 = temp(index2,3);  %write corresponding outflow temperature
temp_in2 = temp(index2,4);  %write corresponding inflow temperature
temp_sample2 = temp(index2,2); %write corresponding sample temperature
deltaT2 = deltaT(index2); %write corresponding temperature difference
extn2 = extn(index2); %extensometer
Pdiff2 = Pdiff(index2); %differential pressure
QpA2 = QpA(index2); %flow rate pump A
QpB2 = QpB(index2); %flow rate pump B
load2 = load(index2);
%% Save isolated data range between index1 and index2 as separate .mat file
%Withing selected time range all parameters defined below will be saved in new file
%Useful to isolate sub-experiments and then individual analysis
time3 = time(index1:index2);
temp_out3 = temp(index1:index2,3);
temp_in3 = temp(index1:index2,4);
temp_sample3 = temp(index1:index2,2);
deltaT3 = deltaT(index1:index2);
extn3 = extn(index1:index2);
Pdiff3 = Pdiff(index1:index2);
QpA3 = QpA(index1:index2);
QpB3 = QpB(index1:index2);
filename = 'Experiment01_6ml.mat';
save(filename,'time3','temp_out3','temp_in3','temp_sample3','deltaT3','extn3','Pdiff3','QpA3','QpB3');
```

Appendix

Script 2 used parameter values from Script 1 of either one selected time point or a selected time range. At this time point or time range, properties such as aperture, permeability based on three different methods elaborated in *Chapter 2.6* and Reynolds number are calculated.

```
%% Properties calculation - Marco Balmer
%% Input parameters
n = input('Enter 1 for exact time point or 2 for averaged over time range: ');
switch 2
    case 1   %taking only one time selected time point
T = (temp_out1+temp_in1)/2; %Water temp in degrees Celcius (taking the average between inflow and outflow here)
extn_init = extn(1); %Extensometer initial value (mm)
extn_curr = extn1; %Extensometer current value (mm)
Pdiff = abs(Pdiff1); %Differential Pressure between inflow and outflow (bar)
Q = (abs(QpA1)+abs(QpB1))/2; %Flow rate (ml/min) through sample
    case 2   %taking a selected time range
T = (mean(temp(index1:index2,3))+mean(temp(index1:index2,4)))/2;
extn_init = extn(1);
extn_curr = mean(extn(index1:index2));
Pdiff = mean(abs(Pdiff(index1:index2)));
Q = (mean(abs(QpA(index1:index2)))+mean(abs(QpB(index1:index2))))/2;
end
%% Calculated parameters
T_K = T + 273.15; %Water temp in Kelvin
mu1 =   2.414*10^(-5)*10^(247.8/(T_K-140)); %Viscosity of water in Pa*s
mu2 = mu1*10^3; %Viscosity of water in cP
Pdiff_atm = Pdiff * 1.0197; %Pressure in atm
length_cm = length/10; %Length in cm
r_cm = (diameter/10)/2; %Radius in cm
circ = 2*pi*r_cm; %Circumference in cm
delta_circ = (extn_curr/10) - (extn_init/10); %Change in Circumference due to fracturing or expansion in cm
circ_new = circ+delta_circ; %New circumference in cm
A = (circ_new^2)/(4*pi); %Cross section of sample in cm^2
Q_new = Q/60; %Flow rate in cm^3/s
%% Permeability calculation (Darcy Permeability or Sample Permeability)
K = ((Q_new*mu2)/A)*(length_cm/Pdiff_atm); %Permeability in Darcy
K_mD = K*1000; %Permeability in mD
%% Permeability based on mechanical fracture aperture (Km = am?2 / 12)
am = (delta_circ/100)/2; %mechanical fracture aperture [m] assuming parallel plate correlation without taking into account roughness
Km = (am^2)/12; %mechanical fracture permeability in m?2
Km_D = Km*1.013249966*10^12; %in Darcy
Km_mD = Km_D*1000; %in mD
%% Permeability based on hydraulic fracture aperture (Kh = ah?2 / 12)
K_sqm = K*9.869233*10^(-13); %sample permeability in m?2
r_m = r_cm/100; %Sample radius in m
ah = nthroot(6*pi*K_sqm*r_m,3); %hydraulic fracture aperture
Kh = (ah^2)/12; %hydraulic fracture permeability in m?2
Kh_D = Kh*1.013249966*10^12 %in Darcy
Kh_mD = Kh_D*1000; %in mD
am_mm = am*1000 %aperture in mm
%% Reynolds number calculation (laminar flow occurs when Re<2300 and turbulent flow occurs when Re>2600)
Dh = 2*am;  %hydraulic diameter assuming a fully filled rectangular duct (filled fracture) where b (diameter) >> a (aperture)
rho_w = 1000;  %Density of water in kg/m^3
Q_m = Q_new * 10e-6;  %Flow rate in m^3/s
A = am*(diameter/1000);  %Cross sectional area of the "pipe" or fracture here
u = Q_m/A  %Fluid velocity m/s
Re = (rho_w*u*Dh)/mu1    %Reynolds number
```

Script 3 represents the potential geothermal power calculation again based on selected time points or time ranges in Script 1.

```matlab
%% Geothermal Power - Marco Balmer
close all;
%% Input parameters
n = input('Enter 1 for exact time point or 2 for averaged over time range: ');
switch n
    case 1
T3 = temp_out1; %Outflow temperature of water in degrees Celcius
T4 = temp_in1; %Inflow temperature of water in degrees Celcius
Q = (abs(QpA1)+abs(QpB1))/2; %Flow rate in ml/min
    case 2
T3 = mean(temp(index1:index2,3));
T4 = mean(temp(index1:index2,4));
Q = (mean(abs(QpA(index1:index2)))+mean(abs(QpB(index1:index2))))/2;
end
%% Calculated parameters
dT = T3 - T4; %Delta T, temperature change of water throughout the "reservoir"
Q_new = Q/60; %Flow rate in g/s
C_per_g = dT * 4.184; %Heat capacity of 1 g water at the set temperature change in Joules
P = C_per_g * Q_new %Potential power output in Watt or J/s
```

Script 4 represents the underlying calculations for the exponential fitting curves of sub-experiments and the evaluation of steady-state conditions.

```matlab
%% Exponential Fitting Curve and Steady-State Check - Marco Balmer
clc
clear all
close all
%% Load relevant data range from .mat file (sub-experiment)
filename = 'Experiment09_10ml.mat';
load(filename);
%% Exponential fit for temperature decay curve
n = size(time3);   %Determine size of time vector
t_init = time3(1);  %Starting time needs to be set to zero
time3_new = time3 - t_init;
x=time3_new;
y1=temp_in3;
y2=temp_out3;
y3=temp_sample3;
f1 = @(b,x) b(1).*exp(b(2).*x)+b(3);              % Exponential function for fit of inflow decay curve
B = fminsearch(@(b) norm(y1 - f1(b,x)), [7; -0.007; 50]);       % Estimate Parameters
f2 = @(c,x) c(1).*exp(c(2).*x)+c(3);              % Exponential function for fit of outflow decay curve
C = fminsearch(@(c) norm(y2 - f2(c,x)), [10; -0.007; 65]);      % Estimate Parameters
f3 = @(d,x) d(1).*exp(d(2).*x)+d(3);              % Exponential function for fit of sample decay curve
D = fminsearch(@(d) norm(y3 - f3(d,x)), [5; -0.007; 90]);       % Estimate Parameters
%% Plot data range
figure(1)   = figure('position',[100 100 700 1000]); % figure size in pixels
hax(1) = axes('position',[0.07 0.070 0.9 0.17]);  % axes window 1 in normalized
hax(2) = axes('position',[0.07 0.310 0.9 0.17]);  % axes window 2 in normalized
hax(3) = axes('position',[0.07 0.550 0.9 0.17]);  % axes window 3 in normalized
hax(4) = axes('position',[0.07 0.790 0.9 0.17]);  % axes window 4 in normalized
% plot all data
hp1 = plot(hax(1),x,deltaT3,'LineWidth',2);
hp2 = plot(hax(2),x,y3,x,f3(D,x),'LineWidth',2);
hp3 = plot(hax(3),x,y2,x,f2(C,x),'LineWidth',2);
hp4 = plot(hax(4),x,y1,x,f1(B,x),'LineWidth',2);
set(get(hax(1),'Ylabel'),'String','\DeltaT ({\circ}C)')
set(get(hax(1),'Xlabel'),'String','time (s)')
set(get(hax(2),'Ylabel'),'String','Sample Temp ({\circ}C)')
```

```matlab
set(hax(2),'XTickLabel',[])
set(get(hax(3),'Ylabel'),'String','Outlet Temp ({\circ}C)')
set(hax(3),'XTickLabel',[])
set(get(hax(4),'Ylabel'),'String','Inlet Temp ({\circ}C)')
set(hax(4),'XTickLabel',[])
set(hax,'Xgrid','on','Ygrid','on')
set(hax,'FontSize',12,'FontWeight','bold')
title(filename,'FontSize',20,'Interpreter','none')
%% Steady state check
%If the temperature variation of the sample, inflow and outflow is less than 1% from the mean in the last 60 seconds of a flow experiment,
it is considered steady-state
a = time3(end)-60;   %Find time 60s from end
[c time_index] = min(abs(time3-a));  %Find best match in time vector 60s from end
temp_sample3_60s = temp_sample3(time_index:end);  %Create vector of sample temperatures of the last 60s
%Percentage difference from mean value to highest and lowest value
mean_sample_percchange_max = ((max(temp_sample3_60s)-mean(temp_sample3_60s))/mean(temp_sample3_60s))*100
mean_sample_percchange_min = ((mean(temp_sample3_60s)-min(temp_sample3_60s))/min(temp_sample3_60s))*100
temp_out3_60s = temp_out3(time_index:end);  %Create vector of outflow temperatures of the last 60s
mean_out_percchange_max = ((max(temp_out3_60s)-mean(temp_out3_60s))/mean(temp_out3_60s))*100
mean_out_percchange_min = ((mean(temp_out3_60s)-min(temp_out3_60s))/min(temp_out3_60s))*100
temp_in3_60s = temp_in3(time_index:end);  %Create vector of outflow temperatures of the last 60s
mean_in_percchange_max = ((max(temp_in3_60s)-mean(temp_in3_60s))/mean(temp_in3_60s))*100
mean_in_percchange_min = ((mean(temp_in3_60s)-min(temp_in3_60s))/min(temp_in3_60s))*100
if (mean_out_percchange_max <= 1) && (mean_out_percchange_min <= 1) &&...
        (mean_sample_percchange_max <= 1) && (mean_sample_percchange_min <= 1) &&...
        (mean_in_percchange_max <= 1) && (mean_in_percchange_min <= 1)
    disp('Steady state is reached (change smaller than 1%)')
else
    disp('Steady state is NOT reached (change larger than 1%)')
end
```

8.2 Experimental and Numerical Data

In this part of the appendix, experimental data of each experiment conducted within this project is presented. Parameters shown include temperatures at the outlet, inlet and sample thermocouple (T_{in}, T_{out}, T_{sample}), pump flowrates of pump A (Q_A), pore fluid pressure difference (P_{diff}), axial load (σ_a) and confining pressure (P_{cell}). The figures are chronologically in order starting with Experiment 1. All experiments are shown in the time range when the apparatus is heated up until the last sub-experiment is completed. In *Tables 8.1* and *8.2* absolute temperature values at no-flow and steady-state flow conditions are listed according to *Figures 3.2* and *3.10*. In *Tables 8.3 – 8.7* temperature values computed in the numerical simulations are listed according to *Figures 3.20, 3.22, 3.25, 3.32* and *3.33*.
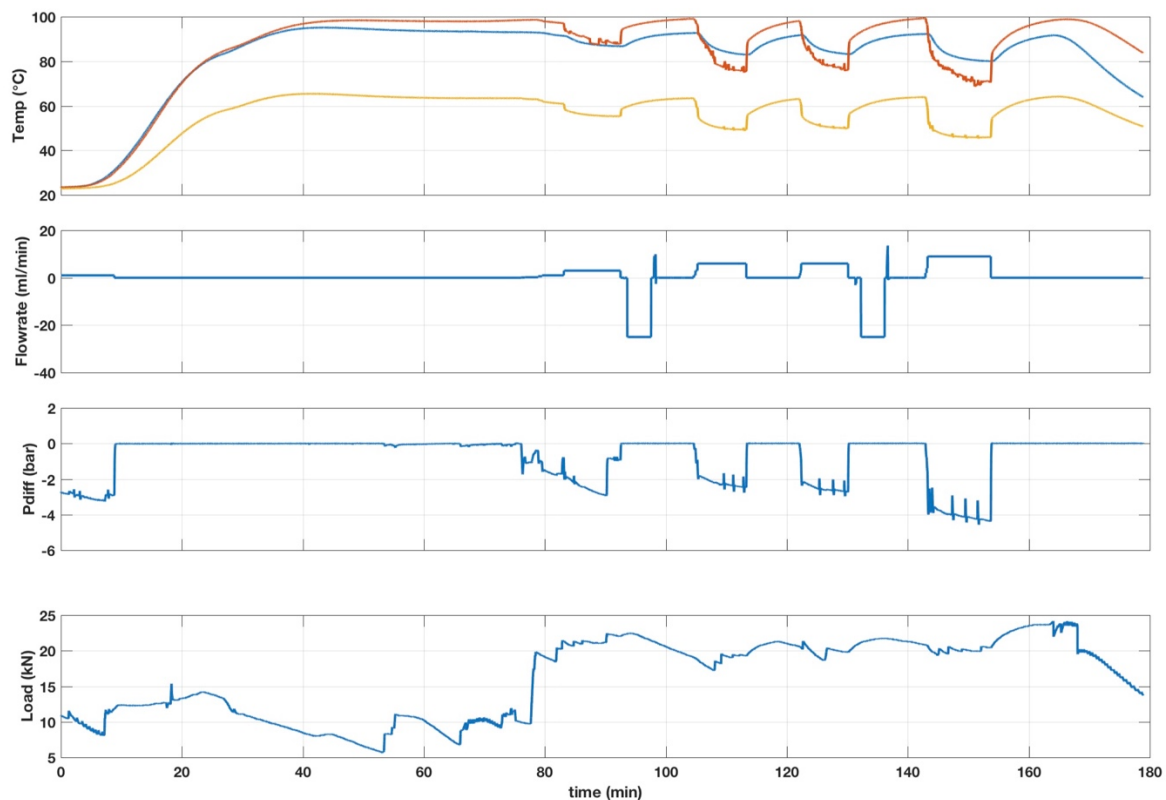
Fig 8.1: **Experiment 1** *recorded data; temperature plot on the top shows the Inlet (yellow), Outlet (red) and Sample (blue) temperature. X-axis represents the running time of the experiment (min).*
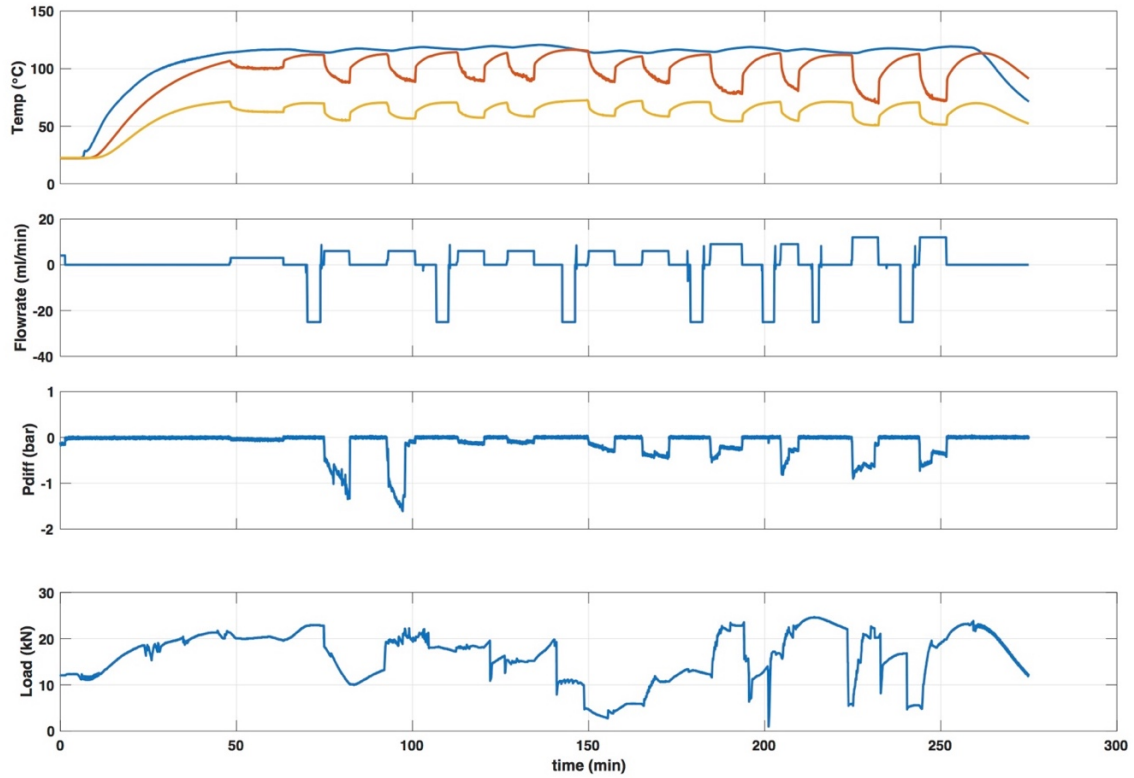
Fig 8.2: *Experiment 2* recorded data; temperature plot on the top shows the Inlet (yellow), Outlet (red) and Sample (blue) temperature. X-axis represents the running time of the experiment (min).
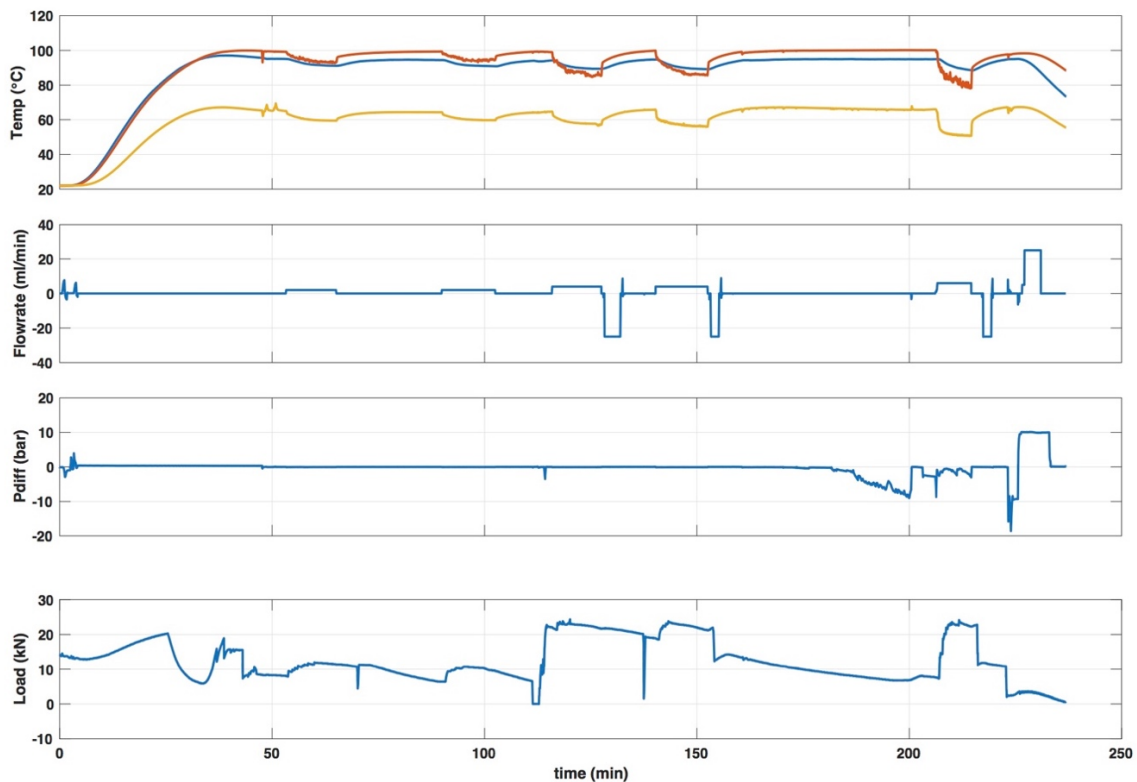
Fig 8.3: *Experiment 3* recorded data; temperature plot on the top shows the Inlet (yellow), Outlet (red) and Sample (blue) temperature. X-axis represents the running time of the experiment (min).
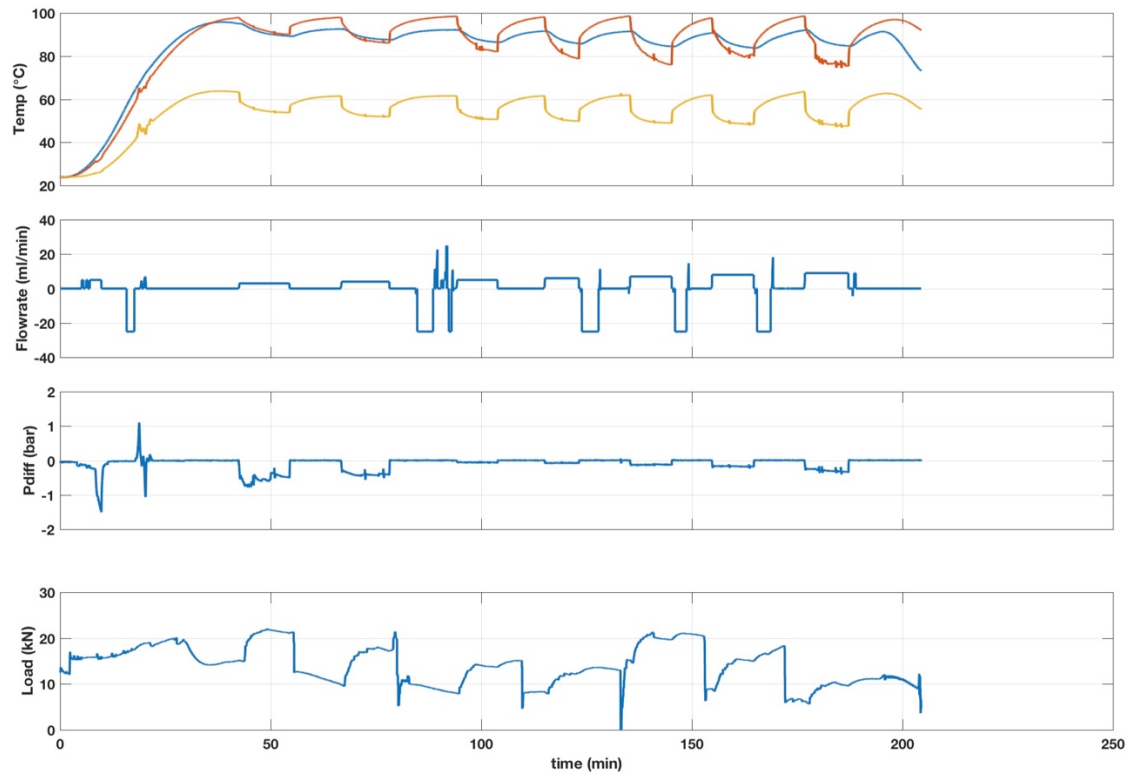
*Fig 8.4: **Experiment 4** recorded data; temperature plot on the top shows the Inlet (yellow), Outlet (red) and Sample (blue) temperature. X-axis represents the running time of the experiment (min).*
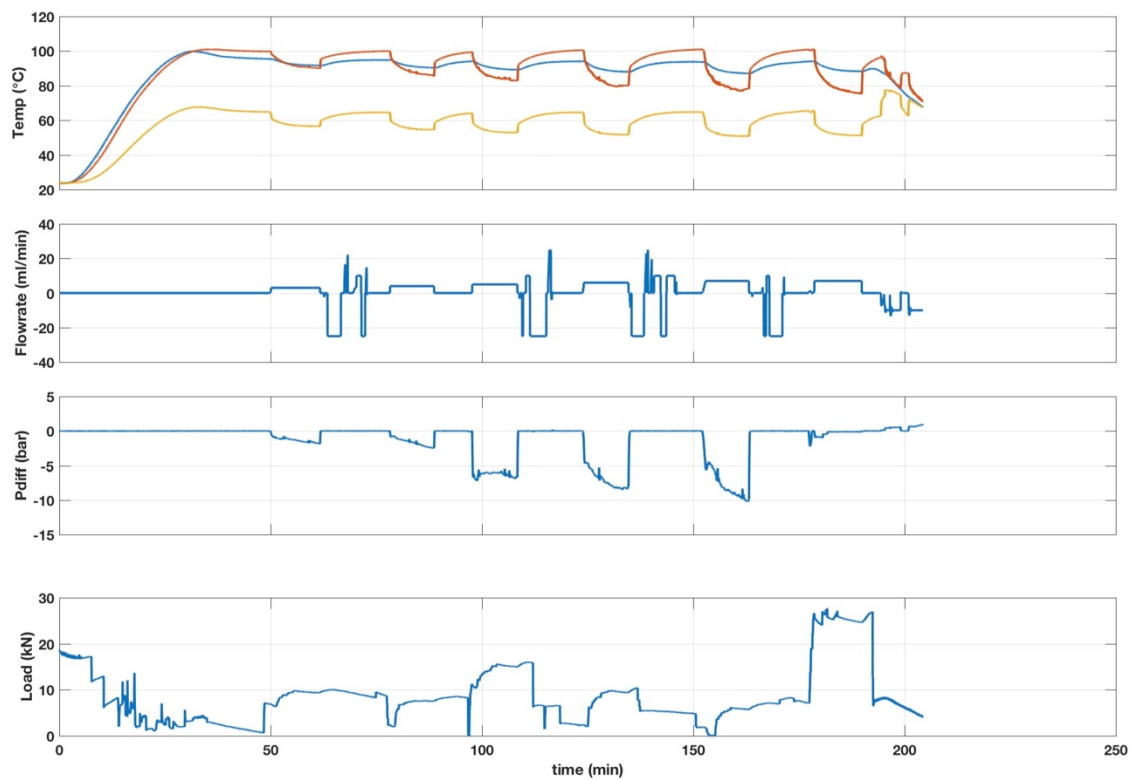
*Fig 8.5: **Experiment 5** recorded data; temperature plot on the top shows the Inlet (yellow), Outlet (red) and Sample (blue) temperature. X-axis represents the running time of the experiment (min).*
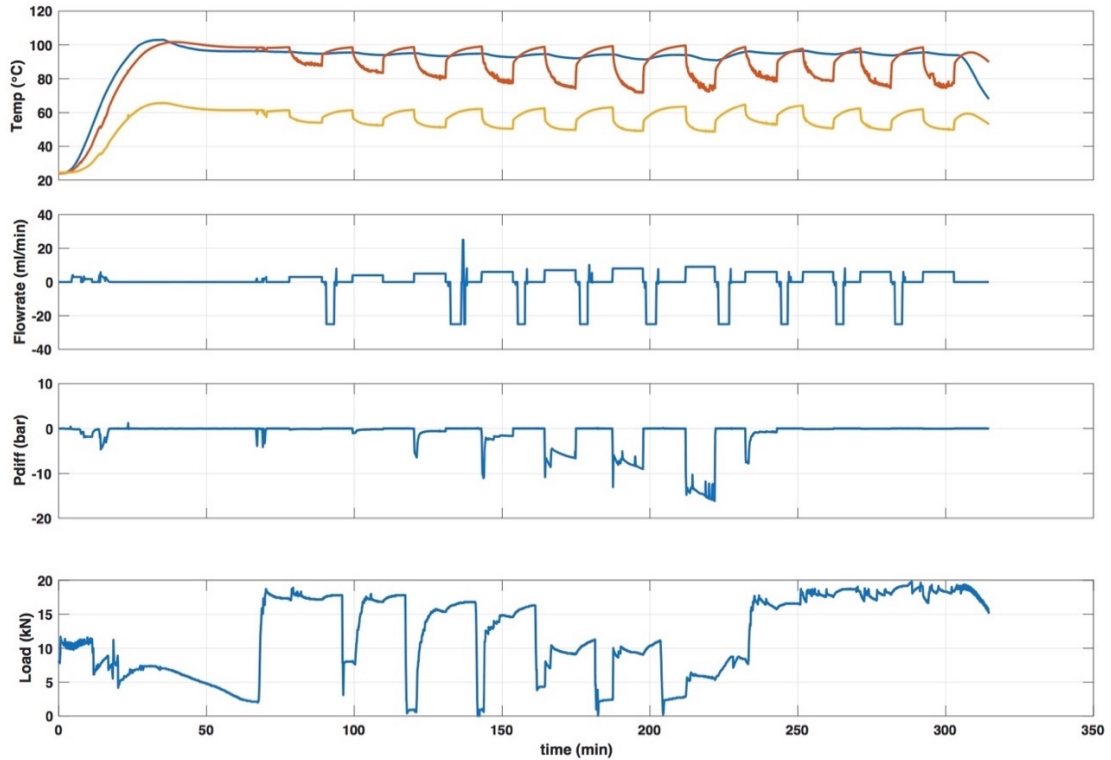
Fig 8.6: **Experiment 6** recorded data; temperature plot on the top shows the Inlet (yellow), Outlet (red) and Sample (blue) temperature. X-axis represents the running time of the experiment (min).
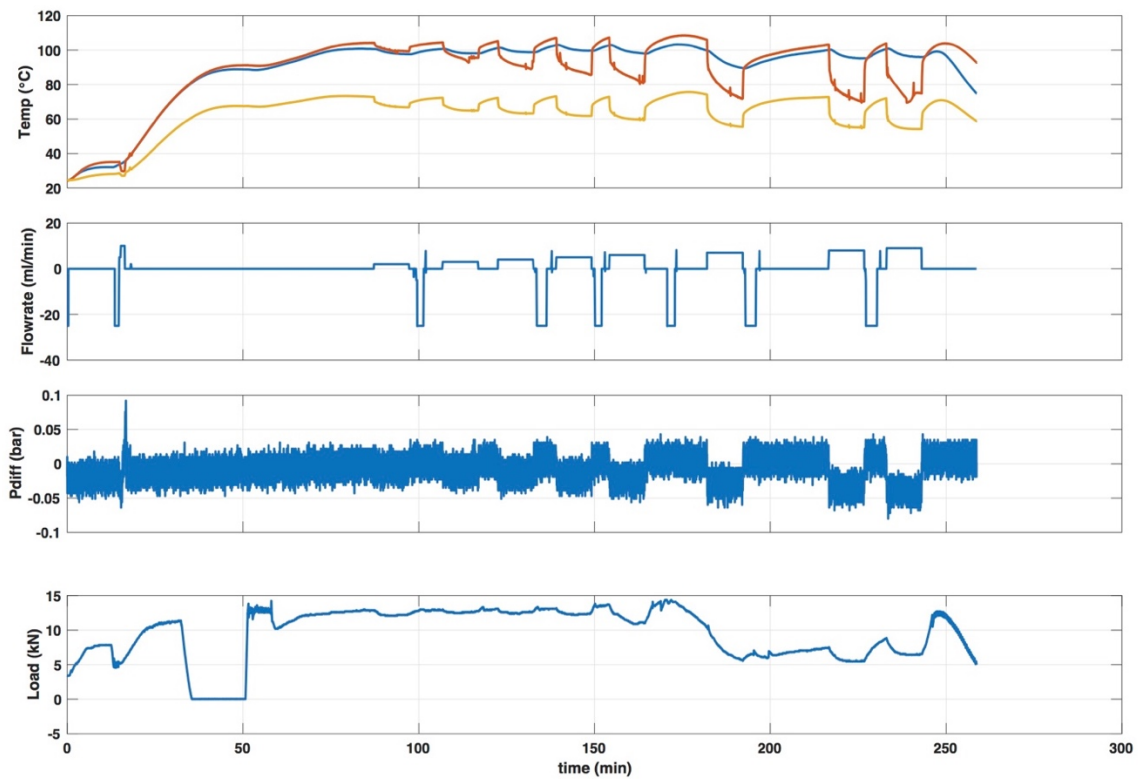
Fig 8.7: **Experiment 7** recorded data; temperature plot on the top shows the Inlet (yellow), Outlet (red) and Sample (blue) temperature. X-axis represents the running time of the experiment (min).
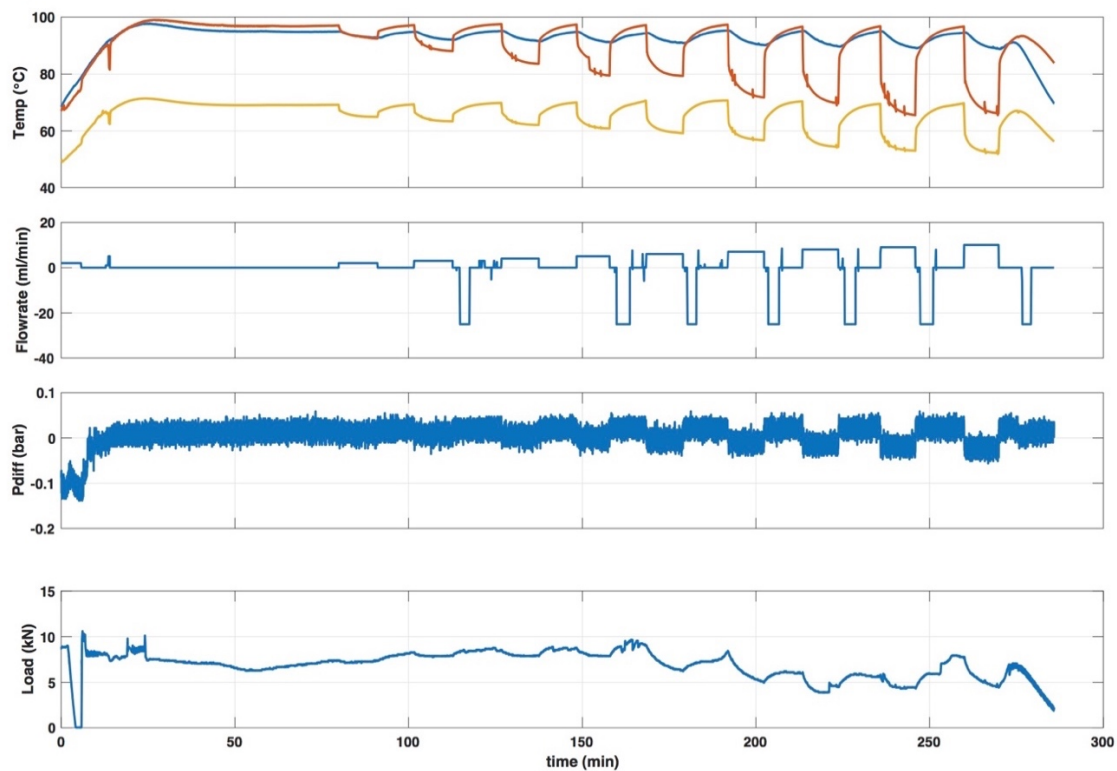
*Fig 8.8: **Experiment 8** recorded data; temperature plot on the top shows the Inlet (yellow), Outlet (red) and Sample (blue) temperature. X-axis represents the running time of the experiment (min).*
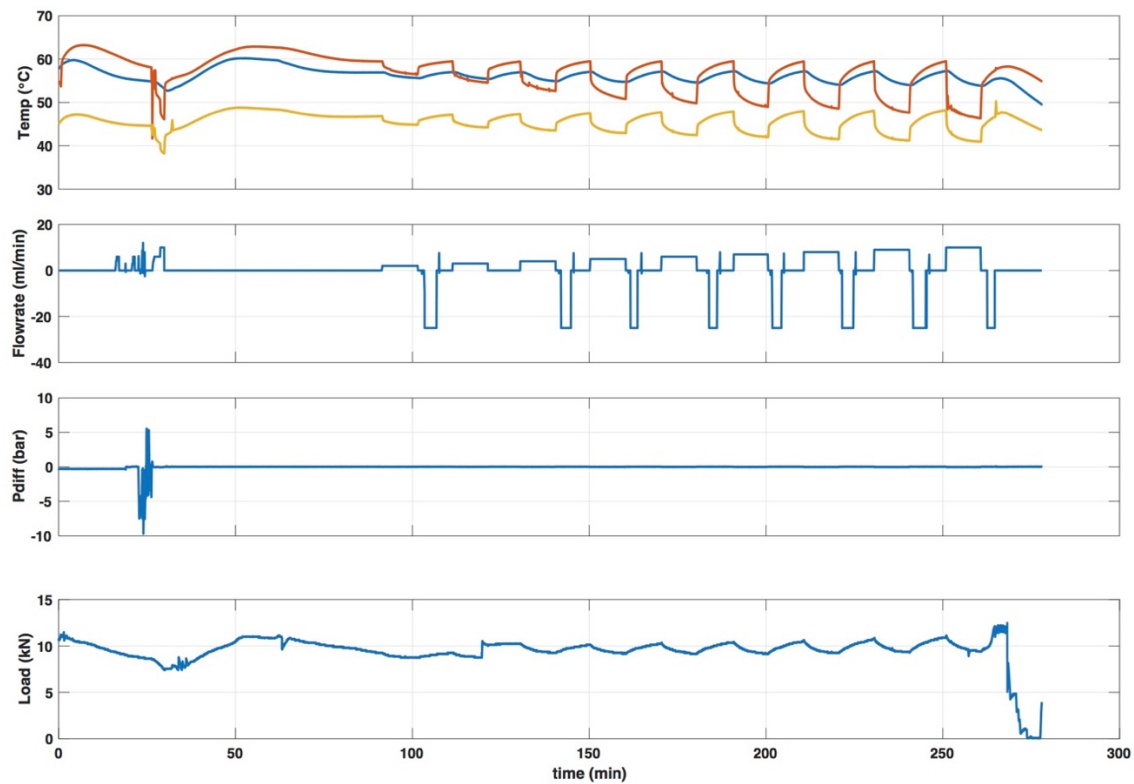
*Fig 8.9: **Experiment 9** recorded data; temperature plot on the top shows the Inlet (yellow), Outlet (red) and Sample (blue) temperature. X-axis represents the running time of the experiment (min).*

Experiment 1

Flow rate (ml/min)	T$_{in}$ (°C)		T$_{out}$ (°C)		T$_{sample}$ (°C)	
	No-flow	Steady-state	No-flow	Steady-state	No-flow	Steady-state
3	63.05	55.30	98.56	87.87	93.01	86.75
6	63.26	49.61	98.58	75.61	92.15	83.15
9	63.90	45.88	99.28	71.16	92.22	80.09

Experiment 2

Flow rate (ml/min)	T$_{in}$ (°C)		T$_{out}$ (°C)		T$_{sample}$ (°C)	
	No-flow	Steady-state	No-flow	Steady-state	No-flow	Steady-state
3	71.23	62.34	106.50	101.15	114.00	116.69
6	70.93	57.47	113.13	88.81	115.71	117.55
9	70.91	54.48	112.91	79.78	115.46	117.40
12	70.51	51.06	112.28	71.68	115.01	117.98

Experiment 3

Flow rate (ml/min)	T$_{in}$ (°C)		T$_{out}$ (°C)		T$_{sample}$ (°C)	
	No-flow	Steady-state	No-flow	Steady-state	No-flow	Steady-state
2	64.63	59.55	99.25	93.95	94.77	91.05
4	65.22	56.52	99.37	85.72	94.42	89.32
6	66.03	50.67	100.09	79.48	94.91	88.61

Experiment 4

Flow rate (ml/min)	T$_{in}$ (°C)		T$_{out}$ (°C)		T$_{sample}$ (°C)	
	No-flow	Steady-state	No-flow	Steady-state	No-flow	Steady-state
3	63.38	53.84	97.81	90.06	95.11	89.36
4	61.42	51.99	97.92	86.08	92.53	87.62
5	61.54	50.66	98.46	82.11	92.17	86.47
6	61.55	49.89	98.13	78.90	91.51	85.89
7	61.91	49.04	98.54	76.08	91.44	84.53
8	61.95	48.48	97.73	80.77	90.72	83.84
9	63.48	47.53	98.57	75.56	91.95	84.78

Experiment 5

Flow rate (ml/min)	T$_{in}$ (°C)		T$_{out}$ (°C)		T$_{sample}$ (°C)	
	No-flow	Steady-state	No-flow	Steady-state	No-flow	Steady-state
3	64.84	56.60	99.79	90.14	95.50	91.69
4	64.55	54.62	100.09	85.88	94.87	90.39
5	64.11	52.89	99.47	82.90	94.11	89.21
6	64.59	51.72	100.54	80.18	94.08	88.06
7	65.13	51.08	101.03	76.90	93.84	87.76

Experiment 6

Flow rate (ml/min)	T$_{in}$ (°C)		T$_{out}$ (°C)		T$_{sample}$ (°C)	
	No-flow	Steady-state	No-flow	Steady-state	No-flow	Steady-state
3	61.40	54.08	98.57	88.16	95.84	94.73
4	61.40	52.50	98.50	83.51	95.45	93.99
5	61.66	51.39	98.66	80.57	95.07	93.37
6	62.20	50.55	99.00	77.73	94.80	92.76
7	62.52	49.87	98.76	74.79	94.52	92.11
8	63.07	49.26	99.24	72.26	94.25	91.47
9	63.56	48.88	99.61	74.90	93.96	91.03

Table 8.1: Temperatures at no-flow and steady-state flow conditions at inlet, outlet and sample of all fracture Experiments 1 – 6

Experiment 8 (Benchmarking)

Flow rate (ml/min)	T_{in} (°C)		T_{out} (°C)		T_{sample} (°C)	
	No-flow	Steady-state	No-flow	Steady-state	No-flow	Steady-state
2	69.16	64.97	97.06	92.48	94.89	92.84
3	69.30	63.41	97.20	88.08	94.80	92.05
4	69.80	62.15	97.51	83.61	95.07	91.57
5	69.93	60.84	97.34	79.47	94.71	91.18
6	70.58	59.26	97.21	79.39	94.32	90.98
7	70.67	56.78	97.31	71.82	95.24	90.25
8	70.36	54.42	96.62	69.76	95.03	89.73
9	69.48	53.04	96.75	65.57	94.94	89.27
10	69.67	52.13	96.69	66.11	94.47	88.88

Experiment 9 (Benchmarking)

Flow rate (ml/min)	T_{in} (°C)		T_{out} (°C)		T_{sample} (°C)	
	No-flow	Steady-state	No-flow	Steady-state	No-flow	Steady-state
2	46.81	44.84	59.45	56.48	56.92	55.63
3	47.15	44.24	59.43	54.58	56.98	55.44
4	47.32	43.52	59.39	52.64	56.98	54.91
5	47.50	42.92	59.48	50.81	57.06	54.74
6	47.71	42.42	59.45	49.86	57.10	54.62
7	47.88	42.03	59.48	48.97	57.16	54.43
8	47.99	41.55	59.42	48.61	57.12	54.10
9	48.06	41.25	59.44	47.65	57.17	54.03
10	48.19	40.94	59.45	46.31	57.21	53.86

Table 8.2: Temperatures at no-flow and steady-state flow conditions at inlet, outlet and sample of all benchmarking
Experiments 8 – 9

Flow rate (ml/min)	T_{out} - T_{in} (°C)		
	0.1 mm	0.2 mm	1 mm
2	29.12	29.55	29.15
3	27.39	27.58	27.16
4	25.13	25.19	24.77
5	22.94	22.94	22.52
6	20.98	20.94	20.52
7	19.26	19.20	18.79
8	17.77	17.70	17.29
9	16.48	16.40	16.00
10	15.35	15.27	14.87
15	11.35	11.29	10.96
20	8.98	8.93	8.68
40	4.87	4.84	4.79
80	2.55	2.54	2.62

*Table 8.3: ΔT values (°C) at varying flow rates and fracture apertures of 0.1, 0.2 and 1 mm according to **Figure 3.20**.*

Aperture (mm)	Tout - Tin (°C)	
	Constant Flow Rate (6 ml/min)	Constant Velocity (0.0333 m/s)
0.05	21.08	27.55
0.1	20.98	20.98
0.15	20.95	16.44
0.2	20.94	13.39
0.25	20.90	11.25
0.3	20.87	9.69
0.35	20.85	8.52
0.4	20.77	7.56
0.45	20.78	6.82
0.5	20.76	6.21
1	20.52	3.36
2	20.23	2.01
4	19.78	1.28

Table 8.4: ΔT values (°C) with varying fracture aperture at constant flow rate and constant fluid velocity according to **Figure 3.22**.

Flow rate (ml/min)	Tout - Tinj (°C)			
	Straight Fracture	Case 1	Case 2	Case 3
2	33.55	37.23	38.28	38.38
3	29.99	35.57	37.29	37.42
4	26.82	33.82	36.22	36.39
5	24.13	32.07	35.11	35.32
6	21.87	30.37	33.97	34.22
7	19.95	28.76	32.83	33.12
8	18.32	27.26	31.71	32.03
9	16.93	25.86	30.61	30.97
10	15.72	24.58	29.55	29.94
15	11.55	19.51	24.89	25.38
20	9.10	16.08	21.28	21.84
40	4.92	9.33	13.19	13.75
80	2.57	5.04	7.41	7.81

Table 8.5: $T_{out} - T_{inj}$ values (°C) at varying flow rates in different geometrical cases according to **Figure 3.25**.

Flow rate (ml/min)	T_{in} (°C) 4 mm	T_{in} (°C) 1 mm	T_{out} (°C) 4 mm	T_{out} (°C) 1 mm	T_{sample} (°C) 4 mm	T_{sample} (°C) 1 mm	$T_{injection}$ (°C)
2	56.81	58.34	96.27	93.96	95.81	95.34	52.10
3	56.16	57.61	92.60	89.40	93.88	93.78	52.10
4	55.76	57.14	88.69	85.63	92.33	92.73	52.10
5	55.49	56.80	85.08	82.65	91.15	91.98	52.10
6	55.28	56.54	81.99	80.25	90.26	91.39	52.10
7	55.13	56.34	79.46	78.28	89.58	90.94	52.10
8	55.01	56.18	77.44	76.77	89.04	90.77	52.10
9	54.91	55.99	75.80	75.17	88.60	89.73	52.10
10	54.83	55.87	74.44	74.09	88.23	89.99	52.10
15	54.52	55.34	69.93	69.95	86.97	89.04	52.10
20	54.35	54.97	67.21	67.42	86.21	88.41	52.10
40	53.85	54.11	62.07	62.70	84.79	86.93	52.10
80	53.45	53.26	58.79	59.38	83.70	85.49	52.10

*Table 8.6: Inlet, outlet, sample and injection temperatures (°C) at varying flow rates with fluid pathways of 4 mm and 1 mm diameter according to **Figure 3.32**.*

Flow rate (ml/min)	$T_{out} - T_{inj}$ (°C) 4 mm	$T_{out} - T_{inj}$ (°C) 1 mm
2	44.17	41.86
3	40.50	37.30
4	36.59	33.53
5	32.98	30.55
6	29.89	28.15
7	27.36	26.18
8	25.34	24.67
9	23.70	23.07
10	22.34	21.99
15	17.83	17.85
20	15.11	15.32
40	9.97	10.60
80	6.69	7.28

*Table 8.7: $T_{out} - T_{inj}$ values (°C) at varying flow rates with fluid pathways of 4 mm and 1 mm diameter according to **Figure 3.33**.*